Science
AAAS

Spontaneous formation of robust two-dimensional perovskite phases

Shaun Tan,[1,†] Meng-Chen Shih,[1,†] Yongli Lu,[1,†] Seung-Gu Choi,[2] Yifan Dong,[3] Joo-Hong Lee,[2] Ilhan Yavuz,[4] Bryon W. Larson,[3] So Yeon Park,[3] Tim Kodalle,[5,6] Ruiqi Zhang,[7] Matthias J. Grotevent,[1] Yu-Kuan Lin,[1] Hua Zhu,[1] Vladimir Bulović,[7] Carolin M. Sutter-Fella,[5] Nam-Gyu Park,[8,9] Matthew C. Beard,[3] Jin-Wook Lee,[2,9] Kai Zhu,[3,*] Moungi G. Bawendi[1,*]

[1]Department of Chemistry, Massachusetts Institute of Technology (MIT), Cambridge, MA, USA

[2]Department of Nanoengineering and Department of Nano Science and Technology, SKKU Advanced Institute of Nanotechnology (SAINT), Sungkyunkwan University, Suwon, Republic of Korea

[3]Chemistry and Nanoscience Center, National Renewable Energy Laboratory (NREL), Golden, CO, USA

[4]Department of Physics, Marmara University, Ziverbey, Istanbul, Turkey

[5]Molecular Foundry, Lawrence Berkeley National Laboratory, Berkeley, CA, USA

[6]Advanced Light Source, Lawrence Berkeley National Laboratory, Berkeley, CA, USA

[7]Department of Electrical Engineering and Computer Science, Massachusetts Institute of Technology (MIT), Cambridge, MA, USA.

[8]School of Chemical Engineering, Sungkyunkwan University, Suwon, Republic of Korea

[9]SKKU Institute of Energy Science & Technology (SIEST), Sungkyunkwan University, Suwon, Republic of Korea

[†]These authors contributed equally to this work.

*Correspondence should be addressed to K.Z. (email: kai.zhu@nrel.gov) or to M.G.B. (email: mgb@mit.edu).

Abstract

The two-dimensional on three-dimensional (2D/3D) perovskite bilayer heterostructure can improve the stability and performance of perovskite solar cells. We show that the 2D/3D perovskite stack in a device evolves dynamically during its end-of-life decomposition. Initially phase-pure 2D interlayers can evolve differently, resulting in different device stabilities. We show that a robust 2D interlayer can be formed using mixed solvents to regulate its crystallinity and phase purity. The resulting 2D/3D devices achieved 25.9% efficiency and had good durability, retaining 91% of their initial performance after 1,074 hours at 85 °C using maximum power point tracking.

The development of two-dimensional/three-dimensional (2D/3D) perovskite bilayer heterostructures has helped boost the performance and durability of perovskite solar cells (PSCs) (*1*–*8*). The 2D interlayer can passivate defects, control charge transport, create a built-in potential, prevent external ingression from the environment, and block ion migration (*1*–*8*). However, for these advantages to be retained, the 2D interlayer needs to be stable; the 2D interlayer must not evolve structurally or compositionally to become non-functional. We will show that 2D interlayers can evolve dynamically during device aging, and that phase-pure 2D interlayers (*9*) can undergo different evolution pathways. We also demonstrate how excess PbI_2 can facilitate 2D formation to promote phase-purity and crystallinity.

We investigated the changes that can occur to 2D perovskite interlayers during long-term illumination. We aged our baseline control 2D/3D device under full-spectrum 1-sun illumination with ultraviolet (UV) included in a nitrogen atmosphere. The 3D perovskite was a $FAPbI_3$-based composition with added MACl and $MAPbBr_3$ for improved crystallization (*10*, *11*) and excess PbI_2. The excess PbI_2 has several roles that will be discussed throughout this work. All devices are based on the n-i-p structure with SnO_2 and spiro-MeOTAD (2,2',7,7'-Tetrakis[N,N-di(4-methoxyphenyl)amino]-9,9'-spirobifluorene) as the charge transporting layers. Under maximum power point (MPP) tracking, the control 2D/3D device had poor photostability (**fig. S1**), where 74% of its initial performance was maintained after 500 hours.

We used coupled-geometry x-ray diffraction (XRD) with sufficient penetration depth to probe the buried 2D interlayer in a device stack. Specifically for the control 2D/3D device (**fig. S2**), the initial n=2 quasi-2D perovskite phase [$L_2APb_2X_7$, hereafter referred to as 2D(n=2), where L, A, and X refer to the spacer organic ligand octylammonium (Oc), the A-site organic cation, and halide anion, respectively] gradually disappeared, with partial transformation into PbI_2 and the n=1 2D phase [L_2PbX_4, referred to as 2D(n=1)]. We postulated that the poor device stability under MPP tracking was

related to this disappearance of most of the 2D interlayer. The bare 3D device had low power conversion efficiency (PCE) because of abundant unpassivated defects. With loss of most of the 2D interlayer, the 2D/3D device lost its defect passivation and essentially reverted back to behave like a bare 3D device. The PCE decreased through degradation because the 2D/3D device slowly turned into a bare 3D device. This degradation process was also evident in the changes of their carrier lifetimes before and after illumination (**fig. S3**). Additionally, the bare 3D device underwent severe initial decay. This so-called burn-in decay was caused by rapid defect migration (*12–14*). As the 2D interlayer disappeared with time, defect migration occurred over a longer duration. The burn-in was not rapid but became an extended period degradation of the 2D/3D device. Overall, the control 2D/3D device was not stable, and most of the 2D perovskite layer disappeared under illumination (discussion in **supplementary text S1**). These findings motivated us to create a durable 2D interlayer.

2D interlayer formation studies

We used time-resolved, in situ grazing-incidence wide-angle x-ray scattering (in situ GIWAXS) to study the formation dynamics of 2D/3D perovskites. Hereafter, the phases present initially upon deposition, excluding the 3D perovskite, are referred to as the initial phase. The previously discussed control 2D/3D perovskites are labelled as the Oc films. The initial phase consisted of the 2D(n=1) perovskite and unreacted PbI_2 (**Fig. 1A**, **1B** and **fig. S4A**). The PbI_2 peak subsequently weakened when annealing of the film began, but this PbI_2 was not fully consumed and was residual in the final film. The 2D(n=1) perovskite only partially converted into the 2D(n=2) phase, so the final film contained an impure mixture of 2D(n=1), 2D(n=2), and PbI_2 phases. Further experiments indicate that the excess PbI_2 in the 3D perovskite composition facilitated 2D formation by providing a readily available PbI_2 source (**fig. S5**), but with the disadvantage that unreacted PbI_2 would remain. For the 3D phase with no excess composition, although no unreacted PbI_2 remained, the 2D perovskite phase had low crystallinity and the PCE was poor (**fig. S6**) (**supplementary text S2**). This trade-off presented an opportunity to assess the interplay between 2D perovskite crystallinity and residual PbI_2.

Unless otherwise stated, all 2D/3D perovskites were based on the 3D with excess PbI_2 composition. Utilizing mixed solvent systems with methylammonium (MA) led to a stepwise progression to promote formation of the 2D(n=2) phase. First, OcMA (Oc ligand with MA additive in isopropanol (IPA)) formed a 2D(n=1) initial phase (**Fig. 1C** and **1D**), which converted into the 2D(n=2) phase upon annealing. PbI_2 and 2D(n=1) were fully reacted, unlike in the control Oc film. Next, the initial phase formed with OcMA:F (OcMA with mixed dimethylformamide and IPA) consisted of a multi-phase mixture of 2D(n=1) and 2D(n=2), and the 2D(n=1) fully converted into 2D(n=2) in the final film (**Fig. 1E** and **1F**). Finally, with OcMA:S (OcMA with mixed

dimethylsulfoxide and IPA), the 2D(n=2) perovskite now became the equilibrium phase, forming spontaneously (**Fig. 1G**, **1H**, and **fig. S7**); neither PbI_2, 2D(n=1), nor any other secondary by-products were present. Despite the excess PbI_2 in the 3D perovskite composition, there was no unreacted PbI_2 left after 2D formation, and a phase-pure 2D perovskite formed with high crystallinity (**Fig. 1I**).

OcMA, OcMA:F, and OcMA:S all attained a final phase-pure 2D(n=2) perovskite. This allowed us to exclude phase purity as a contributing factor when comparing their materials properties. The final crystallinity of the 2D(n=2) phase increased in the order OcMA:S > OcMA:F > OcMA > Oc. This trend was consistent when evaluating the GIWAXS integrated peak area (**Fig. 1I** and **fig. S8**), FWHM peak broadening, and Halder-Wagner analysis from lab-based grazing-incidence XRD of the 2D/3D perovskites (**fig. S9**). We observed a correlation between 2D crystallinity and carrier lifetime (**Fig. 1J** and **1K**). The bare 3D film had a carrier lifetime of 1,067 ns, which increased by 244% to 2,608 ns for the Oc film due to defect passivation by the 2D interlayer. The unreacted PbI_2 left over likely contributed to the increased lifetime (*15*), convoluting with the 2D interlayer contribution. Regardless, the OcMA:S film, even with no unreacted PbI_2, showed the longest carrier lifetime of 4,205 ns (394% increase over the bare 3D film), demonstrating effective suppression of non-radiative recombination.

We extended our study to understand the 2D formation mechanisms (**Fig. 2A** and **table S1**). Different mixed solvents had varying consequences (**fig. S10**). With OcMA:MG (methyl glycol and IPA) and OcMA:A (acetonitrile and IPA), 2D crystallinity and formation were similar compared to OcMA (IPA only). Meanwhile, OcMA:F (**Fig. 1E**), OcMA:N (1-methyl-2-pyrrolidone and IPA), and OcMA:PC (propylene carbonate and IPA) all formed a mixed 2D(n=1) and 2D(n=2) initial phase, with final 2D(n=2) crystallinity improved compared to OcMA. This also suggested OcMA:PC as a promising candidate, and the measured carrier lifetime of 3,842 ns trended with 2D crystallinity (**fig. S11**). The mixed solvent and MA together synergistically regulated 2D formation. Without MA, Oc:S (Oc ligand with dimethylsulfoxide and IPA) showed comparable crystallinity and formation relative to the control Oc (**fig. S12**). Without the mixed solvent, and regardless of the MA halide choice, the final 2D(n=2) crystallinity was only slightly improved over the control Oc (**fig. S13**). In this work, only OcMA:S (**Fig. 1G**) spontaneously formed a 2D(n=2) initial phase and had the highest final 2D crystallinity. Lastly, increasing the MA concentration in OcMA:S showed the possibility of forming the higher-order 2D(n=3) phase (**fig. S14**).

Preliminary theoretical calculations helped shed light on the experimental observations (**supplementary text S3**, **table S2** to **S5**). 2D formation involved partial dissolution of the 3D perovskite surface, followed by secondary recrystallization into the 2D phase (*16*–*18*). A stronger solvent interaction assisted with this dissolution (**Fig 2B** to **2E** and **fig. S15** to **S18**), which was

necessary to source the precursor components (PbI_2 and FA) from the 3D surface used for 2D formation. Sourcing of FA also led to the formation of a FA-based 2D(n=2) perovskite. The MA additive functioned to thermodynamically promote 2D(n=2) formation during its initial stage (**fig. S19**), followed by MA volatilization and FA substitution, resulting in a high crystallinity FA-based 2D(n=2) phase (**fig. S20**, **supplementary text S4**, and **table S6**). This is akin to the role of MA to promote 3D perovskite intermediate phase crystallization (*10*, *19*, *20*). Furthermore, a stronger solvent interaction also slowed down drying and removal, which reduced the nucleation rate during recrystallization to promote higher crystallinity (*21*, *22*).

Grain potential homogenization and electronic structure

Ultraviolet photoelectron spectroscopy (UPS) measurements showed that the Oc 2D/3D perovskite created a type I band alignment relative to the bare 3D perovskite (**fig. S21**). This unfavorable energy offset impeded hole extraction toward spiro-MeOTAD (*23*, *24*). In contrast, the work function and valence band maximum shifts netted a type II alignment for the OcMA:S 2D/3D perovskite and created an energy cascade to bridge hole extraction. OcMA:S and OcMA had similar energetic shifts, consistent with both films having phase-pure 2D(n=2) interlayers, as shown in GIWAXS results. In terms of topographical morphology, no obvious difference was observed between the 2D/3D perovskites in **Fig. 2F** and **fig. S22** from atomic force microscopy (AFM). The surface morphology of the 2D interlayer was not obviously visible in **Fig. 2F** because the AFM measurement setup was optimized for electrical sensitivity, which sacrificed topography resolution (**supplementary text S5**). Potential maps measured with Kelvin probe force microscopy (KPFM) (**Fig. 2G**) showed that the bare 3D film had large intra-grain and grain-to-grain potential variations caused by abundant surface defects that created localized charging effects (*25*). The potential profile transformed into a different pattern for the Oc film as a result of 2D interlayer formation, but individual grains were not resolvable because of intragrain potential inhomogeneity. In this case, the potential fluctuations were caused by the co-existence of multiple phases – unreacted PbI_2, 2D(n=1), and 2D(n=2). For the OcMA:S film, the intra-grain potential uniformity was smoothened out (rightmost in **Fig. 2G**) by the phase-pure 2D(n=2) interlayer and its long-range structural ordering (i.e. high crystallinity). The AFM morphological grain boundary now corresponded spatially with the KPFM potential boundary, and individual grains were distinguishable because of the homogenized intra-grain potential.

Transient reflection spectroscopy (TRS) allowed us to decouple surface versus bulk carrier dynamics in the 3D perovskite by optically generating carriers with short and long wavelengths and modelling the carrier diffusion from the surface (**Fig. 2H**) (*26*). For the OcMA:S film, the carriers diffused away from the 2D/3D interface more efficiently. For example, with 3.54 eV excitation light,

50% of photocarriers moved away from the surface within 50 ps for the OcMA:S film, whereas it took 100 ps for the Oc film, consistent with the homogenized surface potential profile and reduced non-radiative recombination. Conversely, using time-resolved microwave conductivity (TRMC), we found that the carrier lifetime for the OcMA:S film was marginally improved over the Oc film (17.7 to 19.0 μs, 7.3% increase) (**Fig. 2I** and **fig. S23**). Because TRMC is a bulk technique lacking surface sensitivity, these results implied that the 2D perovskite had minimal impact on the bulk 3D perovskite. Direct visualization was obtained by cross-sectional SEM imaging, where the 2D perovskite was seen as a conformal layer formed on top of the 3D perovskite (**fig. S24**). This result was also consistent with time-of-flight secondary ion mass spectrometry (ToF-SIMS) profiling of the elemental distributions (**fig. S25**). Moreover, the optical bandgap of the 2D/3D perovskites was also comparable (**fig. S26**). These results suggest that the 2D perovskite was mostly confined to the 3D perovskite surface with no appreciable bulk diffusion.

Device characterization

We compared the performance of devices based on the 2D/3D perovskites that had the longest carrier lifetimes and found that the PCE increased as OcMA:S > OcMA:PC > OcMA:F > Oc > bare 3D devices (**Fig. 3A**, **3B**, **fig. S27**, and **table S7**). This trend was primarily due to an increasing open-circuit voltage and fill factor, consistent with the increasing carrier lifetime. 2D phase purity contributed to the improvement when comparing between the Oc device versus the other 2D/3D devices, whereas 2D crystallinity accounted for the differences between the OcMA:S, OcMA:PC, and OcMA:F devices, which were all phase-pure and differed only in crystallinity. Generally, the CBD-SnO_2 devices had higher PCE than the NP-SnO_2 devices (**fig. S28**). The OcMA:S devices had the best performance overall, with the champion device based on CBD-SnO_2 reaching a PCE of 25.9% with minimal hysteresis (**Fig. 3C** and **table S8**).

The device stability was assessed through MPP tracking under full-spectrum 1-sun AM 1.5G illumination (UV included). We emphasize that all devices for all stability tests were of the n-i-p structure based on spiro-MeOTAD. No active cooling or heating was applied, and we measured the actual device temperature to be 40-45°C. The target OcMA:S device (**Fig. 3D**), with a peak PCE of 24.3%, sustained its performance with minimal degradation, and retained 96.4% of its initial PCE after >1,700 hours. The control Oc device degraded the most rapidly, dropping to 74.1% of its initial performance after 500 hours. The OcMA:PC and OcMA:F devices had stability intermediate to those of the OcMA:S and Oc devices (**fig. S29**). Both the OcMA:PC and OcMA:F devices showed the same decay behavior (linear decrease after initial rise for ~75 hours), but was distinct from the OcMA:S device.

Comparing the devices with or without excess PbI_2 demonstrated the role of the 2D interlayer. The "Oc no excess" device had no excess PbI_2 in the 3D composition, but its stability and PCE were still far short of the target OcMA:S device (**Fig. 3D**). The "OcMA:S no excess" device was more durable than the "Oc no excess" device (**fig. S30**). Yet, the target OcMA:S device (excess PbI_2 composition but no residual PbI_2 after 2D formation) showed the greatest durability improvement. These comparisons demonstrate the interplay between the 2D interlayer and excess PbI_2 to stabilize the device and simultaneously maintaining a high PCE. None of the 2D/3D devices underwent the rapid initial burn-in degradation seen for all of the bare 3D devices (**fig. S31**), so burn-in was not caused by residual PbI_2 (**supplementary text S6**). The 2D interlayer passivation of defects accounted for the absence of burn-in, which was caused by rapid defect migration (*12–14*). Additionally, the solvent by itself without 2D interlayer formation did not improve stability (**fig. S32**).

Conventional spiro-OMeTAD is doped with tBP (4-tert-butylpyridine) and LiTFSI (lithium bis(trifluoromethane)sulfonimide). Such dopants are hygroscopic, highly diffusible, and lower the glass transition temperature of spiro-OMeTAD (*27–29*), causing a variety of device degradation problems especially at higher temperatures. The spiro-OMeTAD used in this work did not contain tBP nor LiTFSI, which motivated us to assess our devices at elevated temperatures. We first tested the thermal stability in the dark, progressively increasing the temperature from 65-75°C (**Fig. 3E**). After >2,100 hours, on average (8 devices), the OcMA:S devices preserved 86% of their initial PCE. The most stable OcMA:S device retained 91% of its initial performance. We then performed MPP tracking of the OcMA:S device actively heated at 65°C (**Fig. 3F**). The lower initial PCE was caused by the negative temperature coefficient of PSCs, consistent with literature reports of -0.15% per °C (*30*, *31*). The device retained 95% of its initial PCE after >800 hours. We further increased the heating temperature to 85°C under 1-sun AM 1.5G illumination (UV included). This n-i-p device based on our spiro-MeOTAD retained 91% of its initial performance after 1,074 hours illumination (**Fig. 3G**). All devices in this work were of the n-i-p structure based on spiro-MeOTAD, which generally have poorer stability than their inverted p-i-n counterparts (*29*, *32*). Especially at higher temperatures, fewer n-i-p devices have been reported. We demonstrate durable n-i-p devices, competitive with state-of-the-art inverted p-i-n devices (**table S9**).

A robust 2D interlayer

The control Oc device lost most of its 2D interlayer under illumination, whereas the bare 3D perovskite under illumination did not undergo any sort of decomposition (**fig. S33**). Thus, problems with the 2D interlayer limited the overall durability of the 2D/3D Oc device. For the target OcMA:S device, the 2D(n=2) phase was in a stable state both structurally (crystalline long-range ordering) and

thermodynamically (spontaneously-formed single-phase). The 2D interlayer was still intact after >2,500 hours illumination without any sort of phase transformation (**Fig. 4A** and **fig. S34**). Long-term retention of this robust 2D interlayer was key to stabilizing the device. During aging, the 2D interlayer passivated defects and suppressed ion migration, functioning like a blocking barrier. When the 2D perovskite degraded, ions penetrated into the transport layer unimpeded, as observed through post-mortem analysis of the aged devices (**Fig. 4B**).

Initially phase-pure 2D interlayers could degrade differently. For both the OcMA:PC and OcMA:F devices, although the pristine 2D perovskite was phase-pure 2D(n=2), it transformed into the 2D(n=1) phase (**fig. S35**). Nevertheless, further decomposition into PbI_2 did not occur, unlike the control Oc device. We further attempted to generalize our results. For the "Oc no excess" device (**fig. S36**), a phase-pure 2D(n=2) perovskite transformed into 2D(n=1) under illumination, so the 2D interlayer transformation was not caused by excess PbI_2. In contrast, the "OcMA:S no excess" device (**fig. S37**) was durable under the same conditions, so our method worked without excess PbI_2. Our strategy also worked on alternative 2D interlayers based on different widely used spacer organic ligands (**fig. S38** and **S39**). Overall, this work showcases the importance of attaining a robust 2D interlayer (**Fig. 4C**).

References and Notes

1. F. Zhang, S. Y. Park, C. Yao, H. Lu, S. P. Dunfield, C. Xiao, S. Uličná, X. Zhao, L. Du Hill, X. Chen, X. Wang, L. E. Mundt, K. H. Stone, L. T. Schelhas, G. Teeter, S. Parkin, E. L. Ratcliff, Y.-L. Loo, J. J. Berry, M. C. Beard, Y. Yan, B. W. Larson, K. Zhu, Metastable Dion-Jacobson 2D structure enables efficient and stable perovskite solar cells. *Science* **375**, 71–76 (2022).

2. J. Tong, Q. Jiang, A. J. Ferguson, A. F. Palmstrom, X. Wang, J. Hao, S. P. Dunfield, A. E. Louks, S. P. Harvey, C. Li, H. Lu, R. M. France, S. A. Johnson, F. Zhang, M. Yang, J. F. Geisz, M. D. McGehee, M. C. Beard, Y. Yan, D. Kuciauskas, J. J. Berry, K. Zhu, Carrier control in Sn–Pb perovskites via 2D cation engineering for all-perovskite tandem solar cells with improved efficiency and stability. *Nat. Energy* **7**, 642–651 (2022).

3. R. Azmi, E. Ugur, A. Seitkhan, F. Aljamaan, A. S. Subbiah, J. Liu, G. T. Harrison, M. I. Nugraha, M. K. Eswaran, M. Babics, Y. Chen, F. Xu, T. G. Allen, A. ur Rehman, C. Wang, T. D. Anthopoulos, U. Schwingenschlögl, M. De Bastiani, E. Aydin, S. De Wolf, Damp heat–stable perovskite solar cells with tailored-dimensionality 2D/3D heterojunctions. *Science* **376**, 73–77 (2022).

4. S. Sidhik, Y. Wang, M. De Siena, R. Asadpour, A. J. Torma, T. Terlier, K. Ho, W. Li, A. B. Puthirath, X. Shuai, A. Agrawal, B. Traore, M. Jones, R. Giridharagopal, P. M. Ajayan, J. Strzalka, D. S. Ginger, C. Katan, M. A. Alam, J. Even, M. G. Kanatzidis, A. D. Mohite, Deterministic fabrication of 3D/2D perovskite bilayer stacks for durable and efficient solar cells. *Science* **377**, 1425–1430 (2022).

5. C. Liu, Y. Yang, H. Chen, I. Spanopoulos, A. S. R. Bati, I. W. Gilley, J. Chen, A. Maxwell, B. Vishal, R. P. Reynolds, T. E. Wiggins, Z. Wang, C. Huang, J. Fletcher, Y. Liu, L. X. Chen, S.

De Wolf, B. Chen, D. Zheng, T. J. Marks, A. Facchetti, E. H. Sargent, M. G. Kanatzidis, Two-dimensional perovskitoids enhance stability in perovskite solar cells. *Nature* **633**, 359–364 (2024).

6. R. Lin, J. Xu, M. Wei, Y. Wang, Z. Qin, Z. Liu, J. Wu, K. Xiao, B. Chen, S. M. Park, G. Chen, H. R. Atapattu, K. R. Graham, J. Xu, J. Zhu, L. Li, C. Zhang, E. H. Sargent, H. Tan, All-perovskite tandem solar cells with improved grain surface passivation. *Nature* **603**, 73–78 (2022).

7. Z. Liang, Y. Zhang, H. Xu, W. Chen, B. Liu, J. Zhang, H. Zhang, Z. Wang, D.-H. Kang, J. Zeng, X. Gao, Q. Wang, H. Hu, H. Zhou, X. Cai, X. Tian, P. Reiss, B. Xu, T. Kirchartz, Z. Xiao, S. Dai, N.-G. Park, J. Ye, X. Pan, Homogenizing out-of-plane cation composition in perovskite solar cells. *Nature* **624**, 557–563 (2023).

8. R. Azmi, D. S. Utomo, B. Vishal, S. Zhumagali, P. Dally, A. M. Risqi, A. Prasetio, E. Ugur, F. Cao, I. F. Imran, A. A. Said, A. R. Pininti, A. S. Subbiah, E. Aydin, C. Xiao, S. Il Seok, S. De Wolf, Double-side 2D/3D heterojunctions for inverted perovskite solar cells. *Nature* **628**, 93–98 (2024).

9. H. Gu, J. Xia, C. Liang, Y. Chen, W. Huang, G. Xing, Phase-pure two-dimensional layered perovskite thin films. *Nat. Rev. Mater.* **8**, 533–551 (2023).

10. M. Kim, G.-H. Kim, T. K. Lee, I. W. Choi, H. W. Choi, Y. Jo, Y. J. Yoon, J. W. Kim, J. Lee, D. Huh, H. Lee, S. K. Kwak, J. Y. Kim, D. S. Kim, Methylammonium Chloride Induces Intermediate Phase Stabilization for Efficient Perovskite Solar Cells. *Joule* **3**, 2179–2192 (2019).

11. J.-W. Lee, S. Tan, S. Il Seok, Y. Yang, N.-G. Park, Rethinking the A cation in halide perovskites. *Science* **375**, eabj1186 (2022).

12. K. Domanski, B. Roose, T. Matsui, M. Saliba, S.-H. Turren-Cruz, J.-P. Correa-Baena, C. R. Carmona, G. Richardson, J. M. Foster, F. De Angelis, J. M. Ball, A. Petrozza, N. Mine, M. K. Nazeeruddin, W. Tress, M. Grätzel, U. Steiner, A. Hagfeldt, A. Abate, Migration of cations induces reversible performance losses over day/night cycling in perovskite solar cells. *Energy Environ. Sci.* **10**, 604–613 (2017).

13. J. M. Azpiroz, E. Mosconi, J. Bisquert, F. De Angelis, Defect migration in methylammonium lead iodide and its role in perovskite solar cell operation. *Energy Environ. Sci.* **8**, 2118–2127 (2015).

14. S. Tan, I. Yavuz, N. De Marco, T. Huang, S. Lee, C. S. Choi, M. Wang, S. Nuryyeva, R. Wang, Y. Zhao, H.-C. Wang, T.-H. Han, B. Dunn, Y. Huang, J.-W. Lee, Y. Yang, Steric Impediment of Ion Migration Contributes to Improved Operational Stability of Perovskite Solar Cells. *Adv. Mater.* **32**, 1906995 (2020).

15. Q. Chen, H. Zhou, T.-B. Song, S. Luo, Z. Hong, H.-S. Duan, L. Dou, Y. Liu, Y. Yang, Controllable Self-Induced Passivation of Hybrid Lead Iodide Perovskites toward High Performance Solar Cells. *Nano Lett.* **14**, 4158–4163 (2014).

16. A. H. Proppe, A. Johnston, S. Teale, A. Mahata, R. Quintero-Bermudez, E. H. Jung, L. Grater, T. Cui, T. Filleter, C.-Y. Kim, S. O. Kelley, F. De Angelis, E. H. Sargent, Multication perovskite 2D/3D interfaces form via progressive dimensional reduction. *Nat. Commun.* **12**, 3472 (2021).

17. S. Tan, T. Huang, I. Yavuz, R. Wang, M. H. Weber, Y. Zhao, M. Abdelsamie, M. E. Liao, H. Wang, K. Huynh, K. Wei, J. Xue, F. Babbe, M. S. Goorsky, J. Lee, C. M. Sutter-Fella, Y. Yang, Surface Reconstruction of Halide Perovskites During Post-treatment. *J. Am. Chem. Soc.* **143**,

6781–6786 (2021).

18. J. Xue, R. Wang, K.-L. Wang, Z.-K. Wang, I. Yavuz, Y. Wang, Y. Yang, X. Gao, T. Huang, S. Nuryyeva, J. Lee, Y. Duan, L. Liao, R. Kaner, Y. Yang, Crystalline Liquid-like Behavior: Surface-Induced Secondary Grain Growth of Photovoltaic Perovskite Thin Film. *J. Am. Chem. Soc.* **141**, 13948–13953 (2019).

19. J. Park, J. Kim, H.-S. Yun, M. J. Paik, E. Noh, H. J. Mun, M. G. Kim, T. J. Shin, S. Il Seok, Controlled growth of perovskite layers with volatile alkylammonium chlorides. *Nature* **616**, 724–730 (2023).

20. H. Lu, Y. Liu, P. Ahlawat, A. Mishra, W. R. Tress, F. T. Eickemeyer, Y. Yang, F. Fu, Z. Wang, C. E. Avalos, B. I. Carlsen, A. Agarwalla, X. Zhang, X. Li, Y. Zhan, S. M. Zakeeruddin, L. Emsley, U. Rothlisberger, L. Zheng, A. Hagfeldt, M. Grätzel, Vapor-assisted deposition of highly efficient, stable black-phase FAPbI 3 perovskite solar cells. *Science* **370**, 1–8 (2020).

21. Y. Xu, M. Wang, Y. Lei, Z. Ci, Z. Jin, Crystallization Kinetics in 2D Perovskite Solar Cells. *Adv. Energy Mater.* **10**, 1–18 (2020).

22. J.-W. Lee, H.-S. Kim, N.-G. Park, Lewis Acid-Base Adduct Approach for High Efficiency Perovskite Solar Cells. *Acc. Chem. Res.* **49**, 311–319 (2016).

23. J. Euvrard, Y. Yan, D. B. Mitzi, Electrical doping in halide perovskites. *Nat. Rev. Mater.* **6**, 531–549 (2021).

24. J. Peng, F. Kremer, D. Walter, Y. Wu, Y. Ji, J. Xiang, W. Liu, T. Duong, H. Shen, T. Lu, F. Brink, D. Zhong, L. Li, O. Lee Cheong Lem, Y. Liu, K. J. Weber, T. P. White, K. R. Catchpole, Centimetre-scale perovskite solar cells with fill factors of more than 86 per cent. *Nature* **601**, 573–578 (2022).

25. Q. Jiang, J. Tong, Y. Xian, R. A. Kerner, S. P. Dunfield, C. Xiao, R. A. Scheidt, D. Kuciauskas, X. Wang, M. P. Hautzinger, R. Tirawat, M. C. Beard, D. P. Fenning, J. J. Berry, B. W. Larson, Y. Yan, K. Zhu, Surface reaction for efficient and stable inverted perovskite solar cells. *Nature* **611**, 278–283 (2022).

26. Y. Yang, M. Yang, D. T. Moore, Y. Yan, E. M. Miller, K. Zhu, M. C. Beard, Top and bottom surfaces limit carrier lifetime in lead iodide perovskite films. *Nat. Energy* **2**, 16207 (2017).

27. T. Malinauskas, D. Tomkute-Luksiene, R. Sens, M. Daskeviciene, R. Send, H. Wonneberger, V. Jankauskas, I. Bruder, V. Getautis, Enhancing Thermal Stability and Lifetime of Solid-State Dye-Sensitized Solar Cells via Molecular Engineering of the Hole-Transporting Material Spiro-OMeTAD. *ACS Appl. Mater. Interfaces* **7**, 11107–11116 (2015).

28. F. Lamberti, T. Gatti, E. Cescon, R. Sorrentino, A. Rizzo, E. Menna, G. Meneghesso, M. Meneghetti, A. Petrozza, L. Franco, Evidence of Spiro-OMeTAD De-doping by tert-Butylpyridine Additive in Hole-Transporting Layers for Perovskite Solar Cells. *Chem* **5**, 1806–1817 (2019).

29. F. M. Rombach, S. A. Haque, T. J. Macdonald, Lessons learned from spiro-OMeTAD and PTAA in perovskite solar cells. *Energy Environ. Sci.* **14**, 5161–5190 (2021).

30. T. Moot, J. B. Patel, G. McAndrews, E. J. Wolf, D. Morales, I. E. Gould, B. A. Rosales, C. C. Boyd, L. M. Wheeler, P. A. Parilla, S. W. Johnston, L. T. Schelhas, M. D. McGehee, J. M. Luther, Temperature Coefficients of Perovskite Photovoltaics for Energy Yield Calculations. *ACS Energy Lett.* **6**, 2038–2047 (2021).

31. S. M. Park, M. Wei, N. Lempesis, W. Yu, T. Hossain, L. Agosta, V. Carnevali, H. R. Atapattu, P. Serles, F. T. Eickemeyer, H. Shin, M. Vafaie, D. Choi, K. Darabi, E. D. Jung, Y. Yang, D.

Bin Kim, S. M. Zakeeruddin, B. Chen, A. Amassian, T. Filleter, M. G. Kanatzidis, K. R. Graham, L. Xiao, U. Rothlisberger, M. Grätzel, E. H. Sargent, Low-loss contacts on textured substrates for inverted perovskite solar cells. *Nature* **624**, 289–294 (2023).

32. M. V. Khenkin, E. A. Katz, A. Abate, G. Bardizza, J. J. Berry, C. Brabec, F. Brunetti, V. Bulović, Q. Burlingame, A. Di Carlo, R. Cheacharoen, Y.-B. Cheng, A. Colsmann, S. Cros, K. Domanski, M. Dusza, C. J. Fell, S. R. Forrest, Y. Galagan, D. Di Girolamo, M. Grätzel, A. Hagfeldt, E. von Hauff, H. Hoppe, J. Kettle, H. Köbler, M. S. Leite, S. Liu, Y.-L. Loo, J. M. Luther, C.-Q. Ma, M. Madsen, M. Manceau, M. Matheron, M. McGehee, R. Meitzner, M. K. Nazeeruddin, A. F. Nogueira, Ç. Odabaşı, A. Osherov, N.-G. Park, M. O. Reese, F. De Rossi, M. Saliba, U. S. Schubert, H. J. Snaith, S. D. Stranks, W. Tress, P. A. Troshin, V. Turkovic, S. Veenstra, I. Visoly-Fisher, A. Walsh, T. Watson, H. Xie, R. Yıldırım, S. M. Zakeeruddin, K. Zhu, M. Lira-Cantu, Consensus statement for stability assessment and reporting for perovskite photovoltaics based on ISOS procedures. *Nat. Energy* **5**, 35–49 (2020).

33. T. Zhang, F. Wang, H.-B. Kim, I.-W. Choi, C. Wang, E. Cho, R. Konefal, Y. Puttisong, K. Terado, L. Kobera, M. Chen, M. Yang, S. Bai, B. Yang, J. Suo, S.-C. Yang, X. Liu, F. Fu, H. Yoshida, W. M. Chen, J. Brus, V. Coropceanu, A. Hagfeldt, J.-L. Brédas, M. Fahlman, D. S. Kim, Z. Hu, F. Gao, Ion-modulated radical doping of spiro-OMeTAD for more efficient and stable perovskite solar cells. *Science* **377**, 495–501 (2022).

34. T.-H. Han, S. Tan, J. Xue, L. Meng, J.-W. Lee, Y. Yang, Interface and Defect Engineering for Metal Halide Perovskite Optoelectronic Devices. *Adv. Mater.* **31**, 1803515 (2019).

35. J. Carrillo, A. Guerrero, S. Rahimnejad, O. Almora, I. Zarazua, E. Mas-Marza, J. Bisquert, G. Garcia-Belmonte, Ionic Reactivity at Contacts and Aging of Methylammonium Lead Triiodide Perovskite Solar Cells. *Adv. Energy Mater.* **6**, 1502246 (2016).

36. C. Besleaga, L. E. Abramiuc, V. Stancu, A. G. Tomulescu, M. Sima, L. Trinca, N. Plugaru, L. Pintilie, G. A. Nemnes, M. Iliescu, H. Gud, A. Manolescu, I. Pintilie, Iodine Migration and Degradation of Perovskite Solar Cells Enhanced by Metallic Electrodes. *J. Phys. Chem. Lett.* **7**, 5168–5175 (2016).

37. K. Domanski, J.-P. Correa-Baena, N. Mine, M. K. Nazeeruddin, A. Abate, M. Saliba, W. Tress, A. Hagfeldt, M. Grätzel, Not All That Glitters Is Gold: Metal-Migration- Induced Degradation in Perovskite Solar Cells. *ACS Nano* **10**, 6306–6314 (2016).

38. G. Tumen-Ulzii, C. Qin, D. Klotz, M. R. Leyden, P. Wang, M. Auffray, T. Fujihara, T. Matsushima, J. Lee, S. Lee, Y. Yang, C. Adachi, Detrimental Effect of Unreacted PbI 2 on the Long-Term Stability of Perovskite Solar Cells. *Adv. Mater.* **32**, 1905035 (2020).

39. S. Wang, Y. Jiang, E. J. Juarez-perez, L. K. Ono, Y. Qi, Accelerated degradation of methylammonium lead iodide perovskites induced by exposure to iodine vapour ShenghaoWang†,. *Nat. Energy* **16195**, 1–8 (2016).

40. S. Tan, I. Yavuz, M. H. Weber, T. Huang, C.-H. Chen, R. Wang, H.-C. Wang, J. H. Ko, S. Nuryyeva, J. Xue, Y. Zhao, K.-H. Wei, J.-W. Lee, Y. Yang, Shallow Iodine Defects Accelerate the Degradation of α-Phase Formamidinium Perovskite. *Joule* **4**, 2426–2442 (2020).

41. Y. Zhou, I. Poli, D. Meggiolaro, F. De Angelis, A. Petrozza, Defect activity in metal halide perovskites with wide and narrow bandgap. *Nat. Rev. Mater.* **0123456789** (2021).

42. B. Chen, P. N. Rudd, S. Yang, Y. Yuan, J. Huang, Imperfections and their passivation in halide perovskite solar cells. *Chem. Soc. Rev.* **48**, 3842–3867 (2019).

43. G. Kresse, J. Hafner, Ab initio molecular dynamics for liquid metals. *Phys. Rev. B* **47**, 558–561 (1993).

44. G. Kresse, J. Furthmuller, Efficiency of ab-initio total energy calculations for metals and semiconductors using a plane-wave basis set. *Comput. Mater. Sci.* **6**, 15–50 (1996).

45. J. Klimeš, D. R. Bowler, A. Michaelides, Van der Waals density functionals applied to solids. *Phys. Rev. B* **83**, 195131 (2011).

46. H. Peng, Z.-H. Yang, J. P. Perdew, J. Sun, Versatile van der Waals Density Functional Based on a Meta-Generalized Gradient Approximation. *Phys. Rev. X* **6**, 041005 (2016).

47. S. Sidhik, I. Metcalf, W. Li, T. Kodalle, C. J. Dolan, M. Khalili, J. Hou, F. Mandani, A. Torma, H. Zhang, R. Garai, J. Persaud, A. Marciel, I. A. Muro Puente, G. N. M. Reddy, A. Balvanz, M. A. Alam, C. Katan, E. Tsai, D. Ginger, D. P. Fenning, M. G. Kanatzidis, C. M. Sutter-Fella, J. Even, A. D. Mohite, Two-dimensional perovskite templates for durable, efficient formamidinium perovskite solar cells. *Science* **384**, 1227–1235 (2024).

48. B. Ding, Y. Ding, J. Peng, J. Romano-deGea, L. E. K. Frederiksen, H. Kanda, O. A. Syzgantseva, M. A. Syzgantseva, J.-N. Audinot, J. Bour, S. Zhang, T. Wirtz, Z. Fei, P. Dörflinger, N. Shibayama, Y. Niu, S. Hu, S. Zhang, F. F. Tirani, Y. Liu, G.-J. Yang, K. Brooks, L. Hu, S. Kinge, V. Dyakonov, X. Zhang, S. Dai, P. J. Dyson, M. K. Nazeeruddin, Dopant-additive synergism enhances perovskite solar modules. *Nature* **628**, 299–305 (2024).

49. Y. Zou, W. Yu, H. Guo, Q. Li, X. Li, L. Li, Y. Liu, H. Wang, Z. Tang, S. Yang, Y. Chen, B. Qu, Y. Gao, Z. Chen, S. Wang, D. Zhang, Y. Chen, Q. Chen, S. M. Zakeeruddin, Y. Peng, H. Zhou, Q. Gong, M. Wei, M. Grätzel, L. Xiao, A crystal capping layer for formation of black-phase FAPbI 3 perovskite in humid air. *Science* **385**, 161–167 (2024).

50. H. Wang, S. Su, Y. Chen, M. Ren, S. Wang, Y. Wang, C. Zhu, Y. Miao, C. Ouyang, Y. Zhao, Impurity-healing interface engineering for efficient perovskite submodules. *Nature*, doi: 10.1038/s41586-024-08073-w (2024).

51. Y. Bai, Z. Huang, X. Zhang, J. Lu, X. Niu, Z. He, C. Zhu, M. Xiao, Q. Song, X. Wei, C. Wang, Z. Cui, J. Dou, Y. Chen, F. Pei, H. Zai, W. Wang, T. Song, P. An, J. Zhang, J. Dong, Y. Li, J. Shi, H. Jin, P. Chen, Y. Sun, Y. Li, H. Chen, Z. Wei, H. Zhou, Q. Chen, Initializing film homogeneity to retard phase segregation for stable perovskite solar cells. *Science* **378**, 747–754 (2022).

52. J. Jeong, M. Kim, J. Seo, H. Lu, P. Ahlawat, A. Mishra, Y. Yang, M. A. Hope, F. T. Eickemeyer, M. Kim, Y. J. Yoon, I. W. Choi, B. P. Darwich, S. J. Choi, Y. Jo, J. H. Lee, B. Walker, S. M. Zakeeruddin, L. Emsley, U. Rothlisberger, A. Hagfeldt, D. S. Kim, M. Grätzel, J. Y. Kim, Pseudo-halide anion engineering for α-FAPbI3 perovskite solar cells. *Nature* **592**, 381–385 (2021).

53. P. Zhu, D. Wang, Y. Zhang, Z. Liang, J. Li, J. Zeng, J. Zhang, Y. Xu, S. Wu, Z. Liu, X. Zhou, B. Hu, F. He, L. Zhang, X. Pan, X. Wang, N.-G. Park, B. Xu, Aqueous synthesis of perovskite precursors for highly efficient perovskite solar cells. *Science* **383**, 524–531 (2024).

54. S. Yu, Z. Xiong, H. Zhou, Q. Zhang, Z. Wang, F. Ma, Z. Qu, Y. Zhao, X. Chu, X. Zhang, J. You, Homogenized NiO x nanoparticles for improved hole transport in inverted perovskite solar cells. *Science* **382**, 1399–1404 (2023).

55. Z. Li, X. Sun, X. Zheng, B. Li, D. Gao, S. Zhang, X. Wu, S. Li, J. Gong, J. M. Luther, Z. Li, Z. Zhu, Stabilized hole-selective layer for high-performance inverted p-i-n perovskite solar cells. *Science* **382**, 284–289 (2023).

56. J. Liu, X. Chen, K. Chen, W. Tian, Y. Sheng, B. She, Y. Jiang, D. Zhang, Y. Liu, J. Qi, K. Chen, Y. Ma, Z. Qiu, C. Wang, Y. Yin, S. Zhao, J. Leng, S. Jin, W. Zhao, Y. Qin, Y. Su, X. Li, X. Li, Y. Zhou, Y. Zhou, F. Ling, A. Mei, H. Han, Electron injection and defect passivation for

high-efficiency mesoporous perovskite solar cells. *Science* **383**, 1198–1204 (2024).

57. S. Zhang, F. Ye, X. Wang, R. Chen, H. Zhang, L. Zhan, X. Jiang, Y. Li, X. Ji, S. Liu, M. Yu, F. Yu, Y. Zhang, R. Wu, Z. Liu, Z. Ning, D. Neher, L. Han, Y. Lin, H. Tian, W. Chen, M. Stolterfoht, L. Zhang, W.-H. Zhu, Y. Wu, Minimizing buried interfacial defects for efficient inverted perovskite solar cells. *Science* **380**, 404–409 (2023).

58. S. M. Park, M. Wei, J. Xu, H. R. Atapattu, F. T. Eickemeyer, K. Darabi, L. Grater, Y. Yang, C. Liu, S. Teale, B. Chen, H. Chen, T. Wang, L. Zeng, A. Maxwell, Z. Wang, K. R. Rao, Z. Cai, S. M. Zakeeruddin, J. T. Pham, C. M. Risko, A. Amassian, M. G. Kanatzidis, K. R. Graham, M. Grätzel, E. H. Sargent, Engineering ligand reactivity enables high-temperature operation of stable perovskite solar cells. *Science* **381**, 209–215 (2023).

59. H. Chen, C. Liu, J. Xu, A. Maxwell, W. Zhou, Y. Yang, Q. Zhou, A. S. R. Bati, H. Wan, Z. Wang, L. Zeng, J. Wang, P. Serles, Y. Liu, S. Teale, Y. Liu, M. I. Saidaminov, M. Li, N. Rolston, S. Hoogland, T. Filleter, M. G. Kanatzidis, B. Chen, Z. Ning, E. H. Sargent, Improved charge extraction in inverted perovskite solar cells with dual-site-binding ligands. *Science* **384**, 189–193 (2024).

60. Y.-H. Lin, Vikram, F. Yang, X.-L. Cao, A. Dasgupta, R. D. J. Oliver, A. M. Ulatowski, M. M. McCarthy, X. Shen, Q. Yuan, M. G. Christoforo, F. S. Y. Yeung, M. B. Johnston, N. K. Noel, L. M. Herz, M. S. Islam, H. J. Snaith, Bandgap-universal passivation enables stable perovskite solar cells with low photovoltage loss. *Science* **384**, 767–775 (2024).

61. G. Li, Z. Su, L. Canil, D. Hughes, M. H. Aldamasy, J. Dagar, S. Trofimov, L. Wang, W. Zuo, J. J. Jerónimo-Rendon, M. M. Byranvand, C. Wang, R. Zhu, Z. Zhang, F. Yang, G. Nasti, B. Naydenov, W. C. Tsoi, Z. Li, X. Gao, Z. Wang, Y. Jia, E. Unger, M. Saliba, M. Li, A. Abate, Highly efficient p-i-n perovskite solar cells that endure temperature variations. *Science* **379**, 399–403 (2023).

62. D. Gao, B. Li, Q. Liu, C. Zhang, Z. Yu, S. Li, J. Gong, L. Qian, F. Vanin, K. Schutt, M. A. Davis, A. F. Palmstrom, S. P. Harvey, N. J. Long, J. M. Luther, X. C. Zeng, Z. Zhu, Long-term stability in perovskite solar cells through atomic layer deposition of tin oxide. *Science* **386**, 187–192 (2024).

63. J. Li, H. Liang, C. Xiao, X. Jia, R. Guo, J. Chen, X. Guo, R. Luo, X. Wang, M. Li, M. Rossier, A. Hauser, F. Linardi, E. Alvianto, S. Liu, J. Feng, Y. Hou, Enhancing the efficiency and longevity of inverted perovskite solar cells with antimony-doped tin oxides. *Nat. Energy* **9**, 308–315 (2024).

64. S. Li, Y. Xiao, R. Su, W. Xu, D. Luo, P. Huang, L. Dai, P. Chen, P. Caprioglio, K. A. Elmestekawy, M. Dubajic, C. Chosy, J. Hu, I. Habib, A. Dasgupta, D. Guo, Y. Boeije, S. J. Zelewski, Z. Lu, T. Huang, Q. Li, J. Wang, H. Yan, H. Chen, C. Li, B. A. I. Lewis, D. Wang, J. Wu, L. Zhao, B. Han, J. Wang, L. M. Herz, J. R. Durrant, K. S. Novoselov, Z. Lu, Q. Gong, S. D. Stranks, H. J. Snaith, R. Zhu, Coherent growth of high-Miller-index facets enhances perovskite solar cells. *Nature*, 0–1 (2024).

65. Y. Chen, N. Yang, G. Zheng, F. Pei, W. Zhou, Y. Zhang, L. Li, Z. Huang, G. Liu, R. Yin, H. Zhou, C. Zhu, T. Song, C. Hu, D. Zheng, Y. Bai, Y. Duan, Y. Ye, Y. Wu, Q. Chen, Nuclei engineering for even halide distribution in stable perovskite/silicon tandem solar cells. *Science* **385**, 554–560 (2024).

Acknowledgements:

Funding: S.T. was initially supported by First Solar, Inc. during the early stages of the project, then was supported by the US Department of Energy's Office of Energy Efficiency and Renewable Energy (EERE) under the Solar Energy Technologies Office under award number DE-EE0009512. M.-C.S. and Y.L. were supported by the US Department of Energy's Office of Energy Efficiency and Renewable Energy (EERE) under the Solar Energy Technologies Office under award number DE-EE0009512. M.J.G. was supported by First Solar, Inc.. T.K. acknowledges support by the U.S. Department of Energy (DOE), Office of Science, Office of Basic Energy Sciences, Materials Sciences and Engineering Division under Contract No. DE-AC02-05-CH11231 (D2S2 program KCD2S2). Part of the work was carried out as a user project at the Molecular Foundry, a user facility supported by the Office of Science, Office of Basic Energy Sciences, of the U.S. Department of Energy under Contract No. DE-AC02-05CH11231. Work at the Advanced Light Source (ALS) was done at beamline 12.3.2. The ALS is a DOE Office of Science User Facility under contract no. DE-AC02-05CH11231. J.-W.L. acknowledges support by a National Research Foundation of Korea (NRF) grant funded by the Korean government (Ministry of Science and ICT) under contract number RS-2024-00416154. N.-G.P. acknowledges financial support from the National Research Foundation of Korea (NRF) grant funded by the Korean government (Ministry of Science and ICT) under contract NRF-2021R1A3B1076723 (Research Leader Program). Computing resources used in this work were provided by the National Center for High Performance Computing of Turkey (UHeM). TR, TA, and TRMC spectroscopy studies were supported from the Center for Hybrid Organic-Inorganic Semiconductors for Energy (CHOISE), an Energy Frontier Research Center funded by the Office of Basic Energy Sciences, Office of Science within the U.S. Department of Energy. This work was performed in part in the MIT.nano Characterization Facilities. The authors thank Connor Moorman for the FESEM measurements. The authors thank Jordan Cox and Charlie Settens for assisting with the XRD measurements. The U.S. Government retains and the publisher, by accepting the article for publication, acknowledges that the U.S. Government retains a nonexclusive, paid-up, irrevocable, worldwide license to publish or reproduce the published form of this work, or allow others to do so, for U.S. Government purposes.

Author contributions: S. Tan conceived the idea. S. Tan and M.-C. Shih designed and conducted most of the experiments, supervised by M. G. Bawendi. S. Tan, M.-C. Shih, and Y. Lu performed the GIWAXS and XRD measurements. T. Kodalle assisted with the GIWAXS measurements and analyses, supervised by C. M. Sutter-Fella. Y.-K. Lin assisted with the XRD measurements. Y. Dong performed the TA and TR measurements, supervised by M. C. Beard and K. Zhu. M. C. Beard analyzed and developed the model for the TA and TR results. B. W. Larson and S. Y. Park performed the TRMC measurements and analyses, supervised by K. Zhu. S.-G. Choi and J.-H. Lee performed the KPFM and AFM measurements and analyses, supervised by N.-G. Park and J.-W. Lee. S.-G. Choi did the ToF-SIMS measurements and analyses, supervised by J.-W. Lee. I. Yavuz did the theoretical calculations and analyses. R. Zhang, M. J. Grotevent, and H. Zhu assisted with experiments and provided valuable discussions. S. Tan, M.-C. Shih, K. Zhu, and M. G. Bawendi wrote the first manuscript draft. All authors contributed feedback and commented on the manuscript.

Competing interests: S.T., M.-C.S., and M.G.B. are inventors of a provisional patent (US 63/662,739) related to the subject matter of this manuscript. The other authors declare no competing interests.

Data and materials availability: All data needed to evaluate the conclusions in the paper are present in the paper or the supplementary materials.

Supplementary Materials:

This PDF file includes:

Materials and Methods

Supplementary Text S1 to S6

Figs. S1 to S39

Tables S1 to S8

References (33...65)

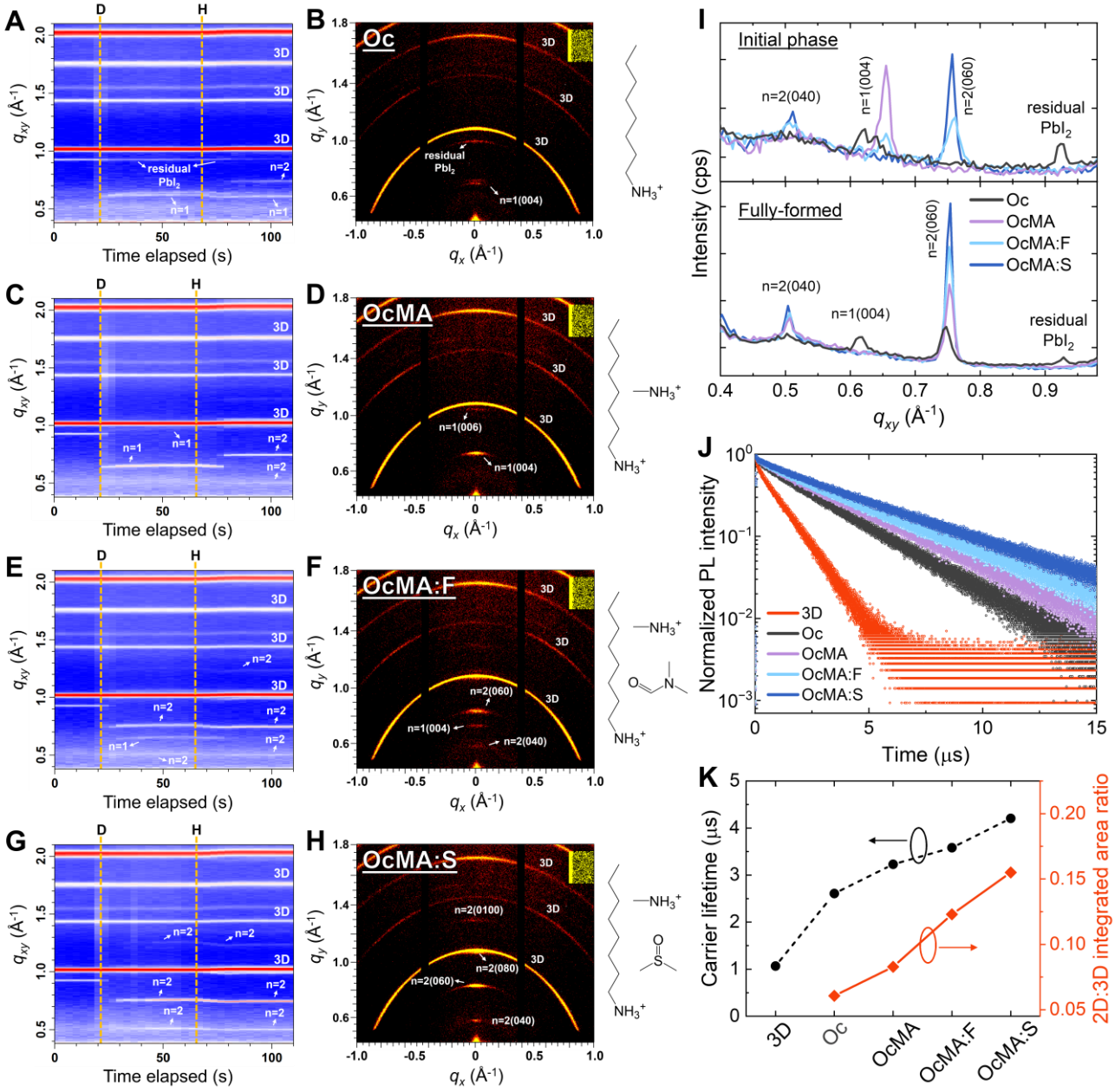

Fig. 1. 2D perovskite formation and crystallinity. (**A** to **H**) In situ GIWAXS measurements, and initial phase GIWAXS patterns of the Oc (A and B), OcMA (C and D), OcMA:F (E and F), and OcMA:S (G and H) 2D/3D perovskites. Labels "D" and "H" denote the deposition time and annealing start time, respectively. (**I**) Azimuthal integrated GIWAXS patterns of the 2D/3D perovskites. Top and bottom panels respectively show the initial (top) and final (bottom) 2D phases. (**J**) Time-resolved PL spectra of the 2D/3D perovskites on glass. (**K**) Plot of carrier lifetime (in black) and 2D:3D integrated area ratio (in red) of the 2D/3D perovskites. The 2D:3D integrated ratio was calculated as the ratio of the 2D(n=2)(060) to 3D(001) integrated peak areas for the final 2D/3D perovskites.

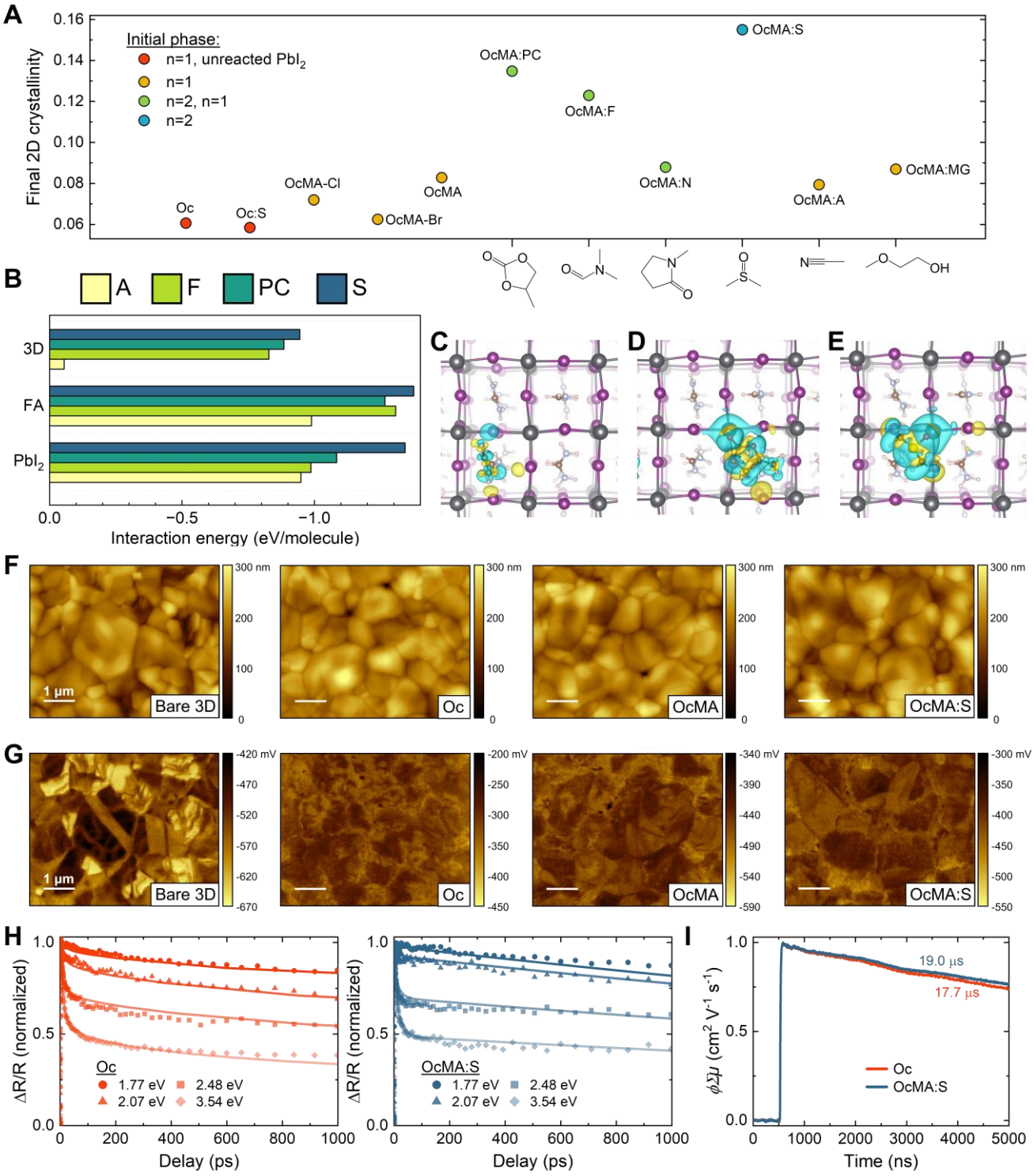

Fig. 2. Expansion to different 2D fabrication systems, potential uniformity, and carrier dynamics. (**A**) Plot of the 2D crystallinity (vertical axis) and the initial phase species (color coded). The 2D crystallinity was quantified by the 2D(n=2):3D integrated area ratio. (**B**) Interaction energy per solvent molecule with the 3D perovskite surface or 3D perovskite components. (**C** to **E**) Slab models of the 3D perovskite surface bonded with acetonitrile (C), propylene carbonate (D), and dimethylsulfoxide (E). (**F** and **G**) AFM topography (F) and KPFM potential mapping (G) of the 2D/3D perovskites. All scale bars are 1 μm. (**F**) TRS carrier dynamics of the control Oc (left) and target OcMA:S (right) 2D/3D perovskites on glass. The probe energy was 1.53 eV. Solid lines are fits using a diffusion model. Any decay in the TRS dynamics represents surface carrier dynamics and not

recombination, i.e., transient absorption dynamics show no decay in 1,000 ps. (**G**) TRMC transients of the control Oc and target OcMA:S 2D/3D perovskites on quartz.

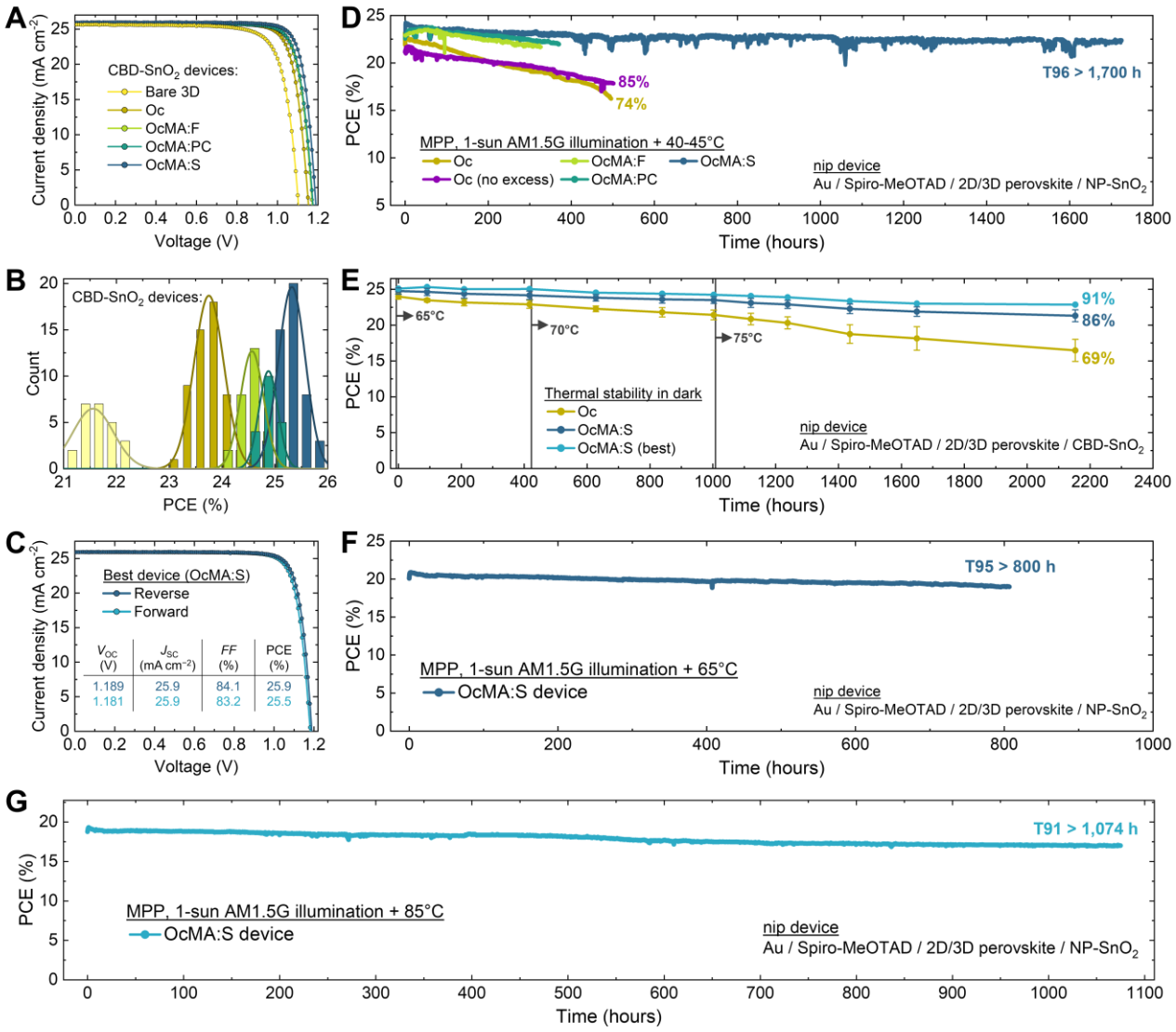

Fig. 3. Device performance and stability. (**A**) Current density-voltage curves of the best devices based on CBD-SnO_2 for the different 2D/3D perovskites. (**B**) Histogram of the device PCE distribution based on CBD-SnO_2. (**C**) Current density-voltage curves of the champion OcMA:S device based on CBD-SnO_2. (**D**) MPP tracking under 1-sun AM1.5G illumination (UV included) of the devices at 40-45°C in a nitrogen atmosphere. (**E**) Thermal stability test of the devices in the dark. Error bars represent the standard deviation of 8 devices. (**F**) 65°C MPP tracking of the OcMA:S device under 1-sun AM1.5G illumination (UV included) in a nitrogen atmosphere. (**G**) 85°C MPP tracking of the OcMA:S device under 1-sun AM1.5G illumination (UV included) in a nitrogen atmosphere.

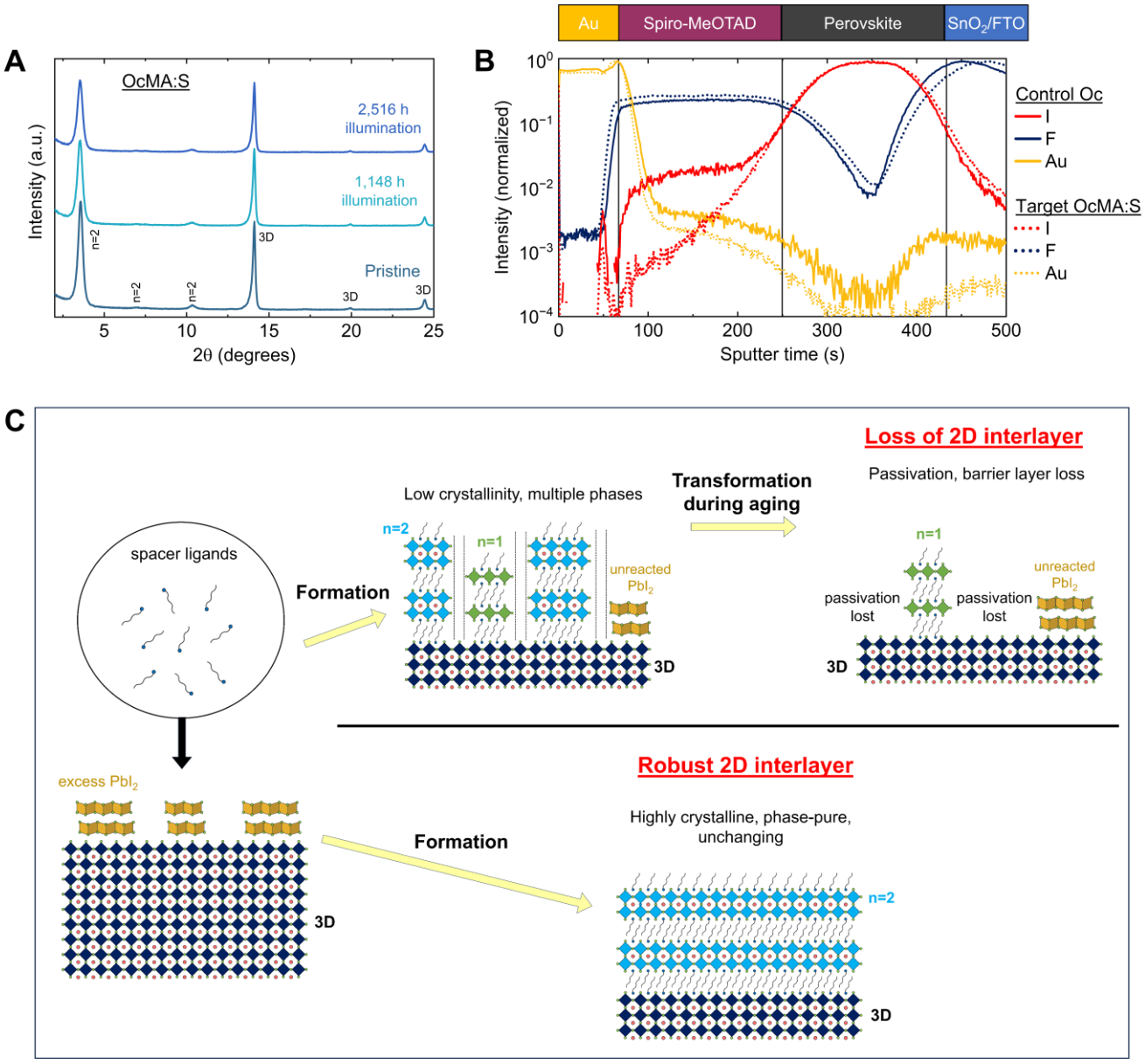

Fig. 4. Evolution of 2D perovskite interlayers. (**A**) XRD patterns of the target OcMA:S 2D/3D perovskite aged under 1-sun AM 1.5G illumination under open-circuit condition in a nitrogen glovebox. The XRD was performed on devices of structure spiro-MeOTAD/2D perovskite/3D perovskite/SnO_2/FTO. The 2D perovskite was thus buried under the spiro-MeOTAD layer for these measurements. (**B**) Post-mortem ToF-SIMS elemental depth profiling of the devices of structure Au/spiro-MeOTAD/2D perovskite/3D perovskite/SnO_2/FTO. The devices were aged simultaneously together for 528 hours under 1-sun AM 1.5G illumination under open-circuit condition in a nitrogen glovebox. Note that the fluorine signal marks either the spiro-MeOTAD layer or FTO substrate layer. The former corresponds to the $TFSI^-$ (bis(trifluoromethanesulfonyl)imide) counter-anion in spiro(TFSI)$_2$. (**C**) Schematic illustrating the formation and transformation of 2D perovskite interlayers, representing the Oc (top) and OcMA:S (bottom) 2D/3D perovskites.

Science
AAAS

595

Supplementary Materials for

Spontaneous formation of robust two-dimensional perovskite phases

Shaun Tan *et al.*

*Corresponding authors: Kai Zhu, kai.zhu@nrel.gov and Moungi G. Bawendi, mgb@mit.edu

600

This PDF file includes:

610

615

Materials and Methods

Materials

All materials were purchased from Sigma-Aldrich, unless otherwise stated. Formamidinium iodide, methylammonium chloride, methylammonium bromide, methylammonium iodide, n-octylammonium bromide, and phenethylammonium iodide were purchased from Greatcell Solar Materials. SnO_2 colloidal solution was purchased from Alfa Aesar Chemicals. 2,2',7,7'-tetrakis(N,N -di-p methoxyphenylamino)-9,9'-spirobifluorene (Spiro-OMeTAD) was purchased from Luminescence Technology Corp. N-Propyl-3-methylpyridinium bis(trifluoromethylsulfonyl)imide was purchased from Strem Chemicals. All chemicals were used directly as received without further purification.

Synthesis of $MAPbBr_3$ single crystals

$MAPbBr_3$ single crystals were synthesized using the inverse temperature crystallization method. 1.34 g of MABr was added to 10 mL of DMF and stirred at room temperature. After fully dissolved, 4.40 g of $PbBr_2$ was added to the MABr/DMF solution. This solution was filtered and then heated at 90 °C in an oil bath with continuous stirring for 3 hours. Finally, the orange $MAPbBr_3$ single crystals were washed with diethyl ether and dried overnight.

Synthesis of spiro^{2+}(TFSI$^-$)$_2$ single crystals

Spiro^{2+}(TFSI$^-$)$_2$ was synthesized by oxidation of Spiro-OMeTAD using Silver(I) bis(trifluoromethanesulfonyl)imide (Ag-TFSI) (*33*). Spiro-OMeTAD (0.5 g) and 10 mL anhydrous dichloromethane were added to a flask with continuous stirring. After fully dissolved, Ag-TFSI (0.3166 g) was added. The flask was evacuated and backfilled with nitrogen. The resultant mixture was stirred at room temperature for 5 hours. The reaction was then diluted by adding dichloromethane. A gray precipitate of silver was filtered off, and the crude product was obtained by rotary evaporator. The solid was dissolved in a minimal amount of dichloromethane and precipitated in dry diethyl ether. The resulting powder of spiro^{2+}(TFSI$^-$)$_2$ was collected via vacuum filtration.

Deposition of SnO_2 electron transport layers

FTO substrates were sequentially cleaned by ultrasonication for 10 min each in Hellmanex, deionized water, acetone, and isopropanol.

For chemical bath deposition (CBD) of SnO_2, a solution was prepared by mixing 137.5 mg of $SnCl_2{\cdot}2H_2O$, 625 mg of urea, 625 µL of hydrochloric acid, and 12.5 µL of thioglycolic acid in 50 mL deionized water. The front electrode of the FTO substrates was taped using Kapton tape before SnO_2 deposition. The substrates and solution were then loaded into a Hellendahl glass reaction vessel (volume ~170 mL) and heated at 65 °C for 14 hours in a water bath. After reaction completion, the SnO_2/FTO

substrates were sequentially cleaned by ultrasonication for 5 min each in deionized water and isopropanol. Finally, the SnO_2/FTO substrates were then annealed at 170 °C for 1 hour in an ambient environment.

For nanoparticle SnO_2 (NP-SnO_2), the SnO_2 colloidal solution was diluted in deionized water in 1:6.5 ratio. The FTO substrates were first treated by oxygen plasma for 10 mins. The diluted SnO_2 colloidal solution was then spun at 3000 rpm for 30 secs. The SnO_2/FTO substrates were then annealed at 150 °C for 30 mins in an ambient environment.

Perovskite solar cell fabrication

For passivation of the buried interface, the SnO_2/FTO substrates were first treated by oxygen plasma for 10 mins. Subsequently, 10 mM potassium chloride in deionized water was spun at 3000 rpm for 30 secs, followed by annealing at 100 °C for 10 mins. The FTO/SnO_2 substrates were treated again by oxygen plasma for 10 mins before perovskite deposition.

The perovskite precursor solution was prepared by mixing 1.4 M FAI, 0.5 M MACl, 0.013 M $MAPbBr_3$, and 1.53 M PbI_2 in a mixed DMF/DMSO solvent with volume ratio 8:1. The solution was stirred for at least 3 hours at room temperature with a magnetic stirrer before use. Fresh solutions were prepared and used within the same day for perovskite fabrication. The solution was filtered with a 0.22 μm PTFE filter before use.

The perovskite films were deposited via spin coating at 500 rpm for 7 secs, then 1000 rpm for 8 secs, then 5000 rpm for 30 secs. 10 secs into the 5000 rpm stage, 700 μL of diethyl ether antisolvent was dropped on the wet film. The films were then annealed successively first at 100 °C for 40 mins, then 150 °C for 5 mins. All processing steps for the perovskite films are conducted in a nitrogen glovebox at a temperature of 25 °C.

For 2D perovskite deposition, the control treatment consists of 10mM of octylammonium bromide dissolved in isopropanol and deposited at 4000rpm for 30 secs. This was then annealed at 100 °C for 5 mins. For the mixed methylammonium halide and solvent systems, we used a molar ratio of octylammonium bromide:methylammonium halide:solvent additive of 1:0.3:2.5, all dissolved in isopropanol for all 2D fabrication systems. For example, for the target OcMA:S treatment, we used 10mM octylammonium bromide, 3mM methylammonium iodide, and 25mM dimethyl sulfoxide dissolved in isopropanol. This was then deposited at 4000rpm for 30 secs, and annealed at 100 °C for 5 mins.

The spiro-OMeTAD hole transporting layer solution was prepared by mixing 90.0 mg spiro-OMeTAD, 9.0 mg of spiro^{2+}(TFSI$^-$)$_2$, and 3.17 μL of N-Propyl-3-methylpyridinium

bis(trifluoromethylsulfonyl)imide in 1 mL of chlorobenzene. The solution was filtered with a 0.22 μm PTFE filter before use. This was then deposited via spin coating at 4000 rpm for 20 secs. Lastly, 100 nm gold electrode was deposited via thermal vacuum evaporation at a rate of 0.5 A s^{-1} for the first 10 nm, then 1.0 A s^{-1} for the rest 90 nm.

Device stability testing

Photostability tests were performed by tracking the maximum power point (MPP) under full-spectrum 1-sun AM 1.5G illumination using a G2V Optics Pico LED solar simulator. No wavelength filters (e.g. ultraviolet) were used. Without active heating or cooling, the measured device temperature was 40-45°C. On the other hand, for MPP tracking at 65°C or 85°C, the device was actively heated using a hotplate. All tests were performed in N_2. All devices for all photostability tests used nanoparticle SnO_2 as the electron transport layer. For only the 85°C MPP photostability test, we reduced only the MACl amount in the 3D perovskite composition to 0.3 M, and everything else about the fabrication was kept the same as described in the previous section.

Thermal stability tests in the dark were performed by heating the devices on a hotplate in N_2 at a set temperature progressively increasing from 65°C, to 70°C, to 75 °C. Periodically, the devices were transferred to a simulated 1-sun AM 1.5G illumination solar simulator to measure their efficiency. All devices for the dark thermal stability tests used chemical bath deposition SnO_2 as the electron transport layer.

In situ wide-angle X-ray scattering measurements

The in-situ GIWAXS measurements were carried out at the 12.3.2 microdiffraction beamline at the Advanced Light Source (ALS). A custom-designed analytical chamber allowed for processing of the perovskite film during simultaneous GIWAXS measurements. The glass/ITO substrates were placed onto the integrated spin coating and puck-heater, and adhered on by a heat transfer paste. The analytical chamber was sealed off from the external environment by being held under nitrogen flow before the precursor solution was applied to the substrate. The incident angle of the incoming X-ray beam for GIWAXS measurements was 1° with a beam energy of 10 keV. The sample detector distance (SDD) was ~155 mm, and the detector was positioned at an angle of 35° from the sample plane. The GIWAXS data were continuously recorded with an integration time of one second using a 2D Pilatus 1 M detector (Dectris Ltd.). After closing the beamline hutch and starting the measurement, the spin coating and annealing procedure was remotely initialized including a remote-controlled dispense. At the end of the spin coating protocol, the puck was heated up to the respective annealing temperature while continuously

spinning at 200 rpm in order to ensure uniform measurement conditions during the annealing step. The resulting GIWAXS patterns were calibrated using an Al_2O_3 reference sample.

AFM and KPFM

To investigate the surface potential homogeneity, Kelvin Probe Force Microscopy (KPFM) measurements were conducted using an Atomic Force Microscopy (AFM) measurement system (NX-10, Park Systems) installed inside a glovebox filled with N2. The surface potential value of each sample was determined by obtaining the difference in work function between the sample surface and the tip apex. To accurately measure the contact potential difference (CPD) of the sample, the biased tip was calibrated at a scan rate of 0.30 Hz before and after each measurement using highly ordered pyrolytic graphite, which is inert and exhibits a reliable work function of 4.65 eV. An NSC36 chromium-gold tip was used to maximize the image resolution of the CPD in consideration of its high electrical sensitivity.

Transient Reflection Spectroscopy

Transient reflectance measurements were collected in a pump–probe set up. The fundamental laser pulse (1030 nm, 190 fs, 1 kHz) is generated from a femtosecond ytterbium-doped potassium gadolinium tungstate (Yb:KGW) laser (PHAROS, Light Conversion). The fundamental pulse is split into two parts by a beam splitter. One part is sent to an optical parametric amplifier (ORPHEUS) for tunable pump generation where the pump is modulated at a frequency of 500 Hz. The other part of the fundamental pulse is focused into a sapphire crystal to generate a white-light continuum that is used as the probe. The pump and probe are spatially overlapped on the surface of the sample.

Time-resolved Microwave Conductivity

Perovskite films were prepared in an identical manner to those used in devices, except onto precleaned 25×11×1-mm quartz plates (Technical Glass Products, Inc.). Microwave conductivity measurements were conducted using previously described protocols (ref). In brief, a 5-ns pulse width, 10-Hz laser at 640 nm was coupled into an X band resonant cavity to photo-generate carriers in each perovskite film, the power from which was measured before and after each measurement using a photothermal detector placed at the sample position and masked by the optical window and waveguide sections when the sample was present. Each sample was positioned inside the microwave cavity such that excitation was always incident to the quartz side, and continuous nitrogen purge was applied to the cavity during all measurements. Neutral density filters were used to attenuate the beam power over one order of magnitude to below 1010 cm-2 absorbed photon flux. For analysis, each sample's fraction of absorbed light was measured inside an integrating sphere diffuse reflectance accessory (Cary 7000i), whereas the

beam attenuation profiles of the filter combinations were extracted from the measured specular transmission data for each neutral density filter at the excitation wavelength.

Material and device characterizations

Time-resolved PL spectra were measured using a time-correlated single-photon counting card (Picoquant; PicoHarp 300). The excitation was a 532 nm picosecond pulsed diode laser (Picoquant; LDH-P-FA-530-B) with a repetition rate of 30 kHz adjusted using a pulse generator (Stanford Research; DG535). UV-Vis spectra were measured using a Cary UV-Vis-NIR spectrophotometer. Static XRD and grazing-incidence XRD spectra were measured using a Rigaku SmartLab and a Bruker D8 Discovery Diffractometer with a General Area Detector Diffraction System. ToF-SIMS measurements were carried out using a TOF-SIMS-5 (ION-TOF) equipped with oxygen-ion beam sputter gun and bismuth primary ion gun. The area of 150 × 150 μm2 was sputtered by the oxygen ion beam with energy of 1 keV and 25 keV bismuth ion beam was subsequently used to collect positive ion species in 40 × 40 μm^2 within the sputtered area. Ultraviolet photoelectron spectroscopy (UPS) spectra were obtained from NEXSA (ThermoFisher Scientific) equipped with a He I discharge UV lamp with photon energy of 21.22 eV. FE-SEM measurements were carried out using a Zeiss Gemini 450 field emission scanning electron microscope.

Current density-voltage (*J-V*) curves were recorded using a Newport Oriel Class AAA, 91195A solar simulator and a Keithley 2420 source meter unit. All *J-V* measurements were recorded under AM 1.5G illumination, carefully calibrated to 100 mW/cm^2 using a calibrated silicon reference cell. *J-V* measurements were performed with a step voltage of 10 mV and a delay time of 50 ms. A dark metal aperture was used to precisely define the device active area during measurements.

Supplementary Text S1

Disappearing 2D interlayer and its effects on device efficiency and stability

From the results in **fig. S1** to **S3**, for only the control 2D/3D Oc device specifically, we observed that the 2D(n=2) perovskite gradually disappeared with partial transformation into the 2D(n=1) phase and PbI_2. The Oc device lost the majority of its 2D interlayer under illumination. This has negative consequences on efficiency and stability for several reasons. (1) The 2D perovskite is important because of its defect passivation effects. With disappearance of the 2D perovskite, defect passivation is lost, and the device basically reverted back into the bare 3D device. In simple words, the PCE decreased because the 2D/3D Oc device is going back to reach the low PCE of the bare 3D device. (2) Defect passivation is also important to suppress defect migration(*34*). The 2D perovskite functions as a blocking barrier in-between the 3D perovskite and transporting layer. This barrier effect is lost if the 2D perovskite disappears. Left unimpeded, halide migration into spiro-MeOTAD is known to cause irreversible redox de-doping reactions to degrade its hole-transport capability(*35*, *36*). Loss of the 2D interlayer will also worsen extrinsic species from entering into and corroding the 3D perovskite. Penetration of extrinsic material (e.g. electrode material, moisture, oxygen, etc) negatively impacts the device stability(*37*). (3) PbI_2 generated is unstable to light and undergoes photolysis into metallic Pb and I_2 gas(*38*). Metallic Pb constitutes a deep-level trap state, while I_2 gas corrodes the perovskite and aggravates decomposition into the yellow δ-$FAPbI_3$ phase(*39*, *40*). (4) Unbounded spacer organic ligands are insulating, and form defect states (e.g. interstitial defects) to trap charges and cause non-radiative recombination(*41*, *42*). Moreover, unbounded spacer organic ligands are also more susceptible to defect migration(*41*, *42*). The above degradation mechanisms will increasingly activate as the 2D perovskite disappears. It is not possible to isolate and assign which slope in **fig. S1** corresponds to which specific degradation mechanism. This is because the overall degradation slope is convoluted by every degradation mechanism simultaneously happening at the same time. As such, it is more important to focus on the overall device stability and efficiency. The control 2D/3D Oc device was not stable, and its 2D perovskite was observed to disappear under illumination.

Supplementary Text S2

Role of excess PbI_2 and 2D perovskite formation

We studied the 2D/3D and bare 3D perovskites, with or without excess PbI_2 composition:

1) 3D excess PbI_2
2) 3D no excess
3) 3D excess PbI_2 – spincoated with isopropanol (no 2D)
4) 3D no excess – spincoated with isopropanol (no 2D)
5) Oc 2D/3D excess PbI_2
6) Oc 2D/3D no excess

For clarification, here we also define:

- Excess PbI_2 = Extra PbI_2 added to the 3D perovskite composition. In other words, the FAI:PbI_2 ratio is not 1:1 in the perovskite precursor solution.
- Unreacted PbI_2 = Unconsumed PbI_2 leftover after 3D or 2D/3D perovskite formation.
- Residual PbI_2 = Same as unreacted PbI_2.

Analyzing the XRD results together help us clarify the role and function of the excess PbI_2:

1) To form 2D perovskites, a source of PbI_2 is necessary. For the "3D excess PbI_2" film (red line **fig. S5A**), the PbI_2 is readily available, leftover as residual PbI_2 after 3D perovskite fabrication. This PbI_2 is consumed to form the 2D perovskite, where the PbI_2 peak at 2θ~12.6° decreased concurrently to the appearance of the 2D peaks (black line **fig. S5A**).

2) The stochiometric 3D perovskite is labelled "3D no excess" (red line **fig. S5B**). No excess PbI_2 is added to the 3D perovskite precursor solution. To form 2D perovskites, the PbI_2 source can be obtained in two ways. In the first way (minor source), there is a tiny amount of residual PbI_2 leftover after 3D perovskite fabrication. The PbI_2 peak is almost negligible and only barely visible when magnified (inset red line **fig. S5B**). This is due to the volatilization of a tiny amount of organic cations during the 3D perovskite thermal annealing:

$$APbX_3\ (\text{3D perovskite}) \xrightarrow{\text{3D annealing}} PbX_2\ (\text{solid}) + AX\ (\text{gas}) \quad (\text{volatization})$$

In the second way (major source), isopropanol (IPA), which is used to deposit the organic spacer ligands, has an additional dual-function to form PbI_2 by dissolving the 3D perovskite organic 'A' cations (black line **fig. S5B**):

$$APbX_3\ (3D\ perovskite) \xrightarrow{IPA\ dissolve} PbX_2\ (solid) + AX\ (in\ IPA) \quad (IPA\ dissolution)$$

Formamidinium is highly soluble in IPA, but PbI_2 is weakly soluble. Solid PbI_2 is left behind for the organic spacer ligands to react with to form 2D perovskites. Note that IPA dissolution also happens for the "3D excess PbI_2" film, as seen in **fig. S5C**.

3) For the "3D no excess" perovskite, annealing (minor source) and IPA dissolution (major source) combined to generate the PbI_2 source to form 2D perovskites (black line **fig. S5D**). Although no unreacted PbI_2 is leftover, the Oc 2D perovskite has low crystallinity (i.e. broad FWHM and low peak intensity).

4) Comparing "Oc 2D/3D excess PbI_2" and "Oc 2D/3D no excess", there is a trade-off between unreacted PbI_2 and 2D formation. In other words, **excess PbI_2 facilitated 2D formation by providing a readily available PbI_2 source**, but leftover unreacted PbI_2 is a problem. Now it becomes important to compare their stability and efficiency. Firstly in terms of efficiency (**fig. S6**), the "Oc 2D/3D excess PbI_2" devices have higher FF, V_{OC}, and PCE than the "Oc 2D/3D no excess" devices. Higher 2D crystallinity is the primary reason for the improved FF and V_{OC}, while the residual PbI_2 contributed to some of the V_{OC} increase. Particularly, the improved FF of the "Oc 2D/3D excess PbI_2" devices can be mainly attributed to the higher 2D crystallinity. The FF of the "3D excess PbI_2" devices is similar or slightly lower than the "3D no excess" devices, meaning that residual PbI_2 alone does not improve FF. Overall, the "Oc 2D/3D excess PbI_2" devices have the highest PCE in **fig. S6**, but it is important to consider their device stability. Comparing these devices presents an opportunity to assess how the trade-off between unreacted PbI_2 and 2D formation affects device stability, which will be discussed later in the manuscript.

Supplementary Text S3

Preliminary theoretical studies

We applied first-principles calculations within the framework of density functional theory (DFT), employing a plane-wave basis set and the projected augmented wave method, as implemented in the VASP package(*43*, *44*). For describing the exchange-correlation functionals in DFT, we opted the SCAN+rvv10 type meta-GGA functional with a van der Waals (vdW) functional(*45*, *46*). All starting geometries are generated based on the experimental lattice parameters of $FAPbI_3$. In our self-consistent field calculations and geometry optimizations, we utilized a 400 eV cutoff energy for the plane-wave basis sets and a 4 × 4 × 1 gamma-centered k-point mesh was chosen for Brillouin-zones sampling. During the geometry optimizations, we permitted the relaxation of ionic positions and cell dimensions using a conjugate gradient algorithm, enforcing that all residual forces were reduced to less than 0.02 eV/Å.

For the calculations involving surfaces and 2D structures, periodic slabs, with a minimum separation of 15-20 Å of vacuum in the direction perpendicular to the surfaces, were used to model the surfaces and 2D perovskites. We utilized a (100) direction in all surface calculations. Formation energy of 2D perovskites were calculated from:

$$\Delta H = E_{2D+Oc} - [nE_{PbI_2} + n/2\, E_{AI} + nE_{OcI}]$$

for FA or MA perovskites ($A = FA, MA$), where is n is the number of units to generate the 2D perovskite having an Oc unit for each octahedral gap, E_{2D+Oc} is the energy of the whole complex, E_{PbI_2} is the energy of the PbI_2 in the hexagonal phase and E_{MAI}, E_{FAI} are the energies of MAI and FAI crystals in the rock-salt phase, respectively, and E_{OcI} is the energy of OcI in the gas phase. Molecular binding energies to the (100) surface are calculated from:

$$\Delta E_{bind} = E_{pvsk+mol} - [E_{pvsk} + E_{mol}]$$

where $E_{pvsk+mol}$ is the energy of the perovskite slab and the molecule complex, E_{pvsk} is the energy of the perovskite slab only and E_{mol} is the energy of the molecule only.

Solvent molecule and PbI_2 interactions in the gas phase are calculated from

$$\Delta E_{bind} = E_{PbI_2+mol} - [E_{PbI_2} + E_{mol}]$$

where E_{PbI_2+mol} is the energy of the single PbI_2 and molecule complex, E_{PbI_2} and E_{mol} are the gas-phase energies of PbI_2 and solvent molecule.

Charge-density difference (CDD) distribution, $\Delta\rho$, is calculated from

$$\Delta\rho = \rho_{pvsk+mol} - [\rho_{pvsk} + \rho_{mol}]$$

where $\rho = \rho(\vec{r})$ is the charge-density distribution; $\rho_{pvsk+mol}$ is the charge-density of the perovskite slab and the molecule complex, ρ_{pvsk} is the charge-density of the perovskite slab only and ρ_{mol} is the charge-density of the molecule only.

Supplementary Text S4

The role of MA in 2D formation

The primary role of the MA additive was to thermodynamically promote 2D(n=2) formation during its initial stage. During crystallization, MA vaporization occurred, following by FA substitution, which finally formed a FA-based 2D(n=2) phase. Looking at the "OcMA:S 2D/3D" perovskite (in blue, **fig. S20C**), the 2D peak positions closely matched that of 2D "$OA_2FAPb_2X_7$" (in red, **fig. S20B**). Note that the measurement uncertainty was ±0.02°. In contrast, the 2D(n=2) peak positions of "OcMA:S 2D/3D" differed significantly from that of 2D "$OA_2MAPb_2X_7$" (in black, **fig. S20A**). For the 2D interlayer, vaporization occurred readily since it is a small amount of MA (3 mM) in the 2D precursor solution. The precursor solution was also deposited to the top film surface, allowing it to escape easily. If any MA is leftover, it is at most trace amounts. For additional evidence, next we fabricated the "Oc on $FAPbI_3$" 2D/3D perovskite (in green, **fig. S20D**). Here, we deposited the control Oc 2D perovskite (only Oc ligand in IPA solvent) on the pure $FAPbI_3$ 3D perovskite. This $FAPbI_3$ contained neither MACl nor $MAPbBr_3$. There was no MA at all in both the 2D and 3D perovskite precursor solutions. The 2D(n=2) perovskite still formed, which demonstrated that FA substitution must have occurred. And this must only be a pure FA-based 2D(n=2) perovskite. Comparing their 2D peaks, the peak positions matched for "Oc on $FAPbI_3$" and "OcMA:S 2D/3D".

Supplementary Text S5

Image resolution in AFM and KPFM

The AFM images in **Fig. 2F** cannot properly resolve the 2D perovskite morphology. This is because we used the NSC36 cantilever tip in **non-contact mode** imaging to maximize and obtain the best electrical resolution. There is a **trade-off between electrical resolution versus morphology/topography resolution**. The NSC36 tip has high electrical sensitivity, but low resonance frequency (90 kHz) and low spring constant (1 N m^{-1}), which also means it is not suitable for contact mode imaging. Contact mode imaging (i.e. dynamic force tapping mode) would have given the best morphology resolution. Overall, the goal of the experiments in **Fig. 2F** and **2G** is to study the electrical potential uniformity, so we maximized electrical resolution.

Supplementary Text S6

Decoupling 2D perovskite versus residual PbI_2

To study the contributions of the 2D perovskite and residual PbI_2, we performed MPP stability tests on 2D/3D and bare 3D devices, with or without excess PbI_2:

1) Oc 2D/3D excess PbI_2
2) Oc 2D/3D no excess
3) 3D excess PbI_2
4) 3D no excess

Firstly, looking at the 2D/3D devices (**fig. S31**), the "Oc 2D/3D no excess" device had lower PCE, but was more stable (T85 = 500 hours) than the "Oc 2D/3D excess PbI_2" device (T74 = 500 hours). This is well-known, where the presence of residual PbI_2 for the "Oc 2D/3D excess PbI_2" device improved PCE but sacrificially worsened degradation. More importantly, now we are able to decouple the contributions of the 2D perovskite versus the absence of residual PbI_2 on device stability.

Our target "OcMA:S" device (main text **Fig. 3D**) also had no residual PbI_2. Eventhough its 3D perovskite used the excess PbI_2 composition, no unreacted PbI_2 was leftover after 2D formation. The target "OcMA:S" device (T96 > 1,700 hours) was by far more stable (and higher PCE) than the "Oc 2D/3D no excess" device. Their huge contrast is obvious when the devices are plotted together in main text **Fig. 3D**. This implies that **the absence of residual PbI_2 only contributed minorly**. IF the absence of residual PbI_2 was the major reason, then we would expect the "Oc 2D/3D no excess" and "OcMA:S" devices to have similar stability, which is certainly not the case. In other words, **the 2D perovskite was still the dominant reason that stabilized the OcMA:S device**, while the absence of residual PbI_2 only contributed partially. We illustrate this using the simple schematic:

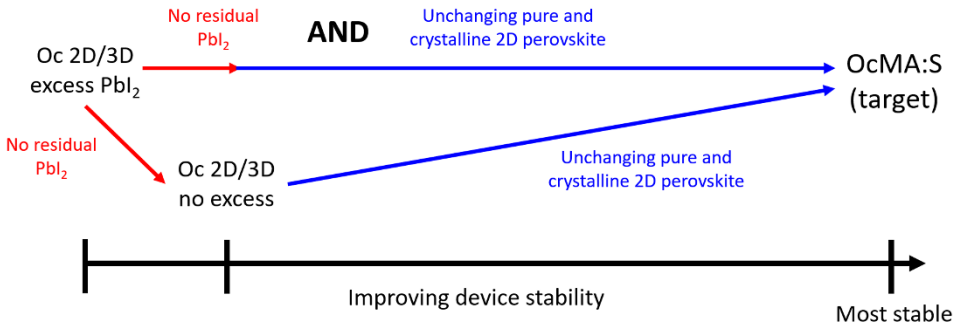

All 2D/3D devices were more stable (and higher PCE) than all bare 3D devices (**fig. S31**). The "3D excess PbI_2" device was the most unstable among all devices, with a severe initial burn-in, where the PCE rapidly dropped to 73% of its initial PCE in the first 30 hours. The "3D no excess" device – even with no excess PbI_2 at all – only improved barely. The initial burn-in was still severe (82% retained in first 30 hours) – showing that the burn-in is not caused by the residual PbI_2 – and the device was still unstable overall (T67 = 500 h). This again shows that although the absence of residual PbI_2 did improve stability, the 2D perovskite had a much more significant contribution.

Rapid defect migration is responsible for the burn-in effect(*12–14*). Especially, none of the 2D/3D devices experienced the rapid initial burn-in (**fig. S31**). This shows the effectiveness of the 2D interlayer to passivate defects and suppress defect migration, functioning like a blocking barrier. But if the 2D interlayer is disappearing, defect passivation is slowly lost and defect migration occurred over a longer duration – essentially, the "burn-in" is no longer rapid, but became stretched out and turned into the long-term degradation experienced by the 2D/3D device. For the target OcMA:S device, its unchanging 2D interlayer was robust and structurally intact during aging. This was the key to stabilize the OcMA:S device. This is why it is critically important to make sure that the 2D interlayer is not lost during aging.

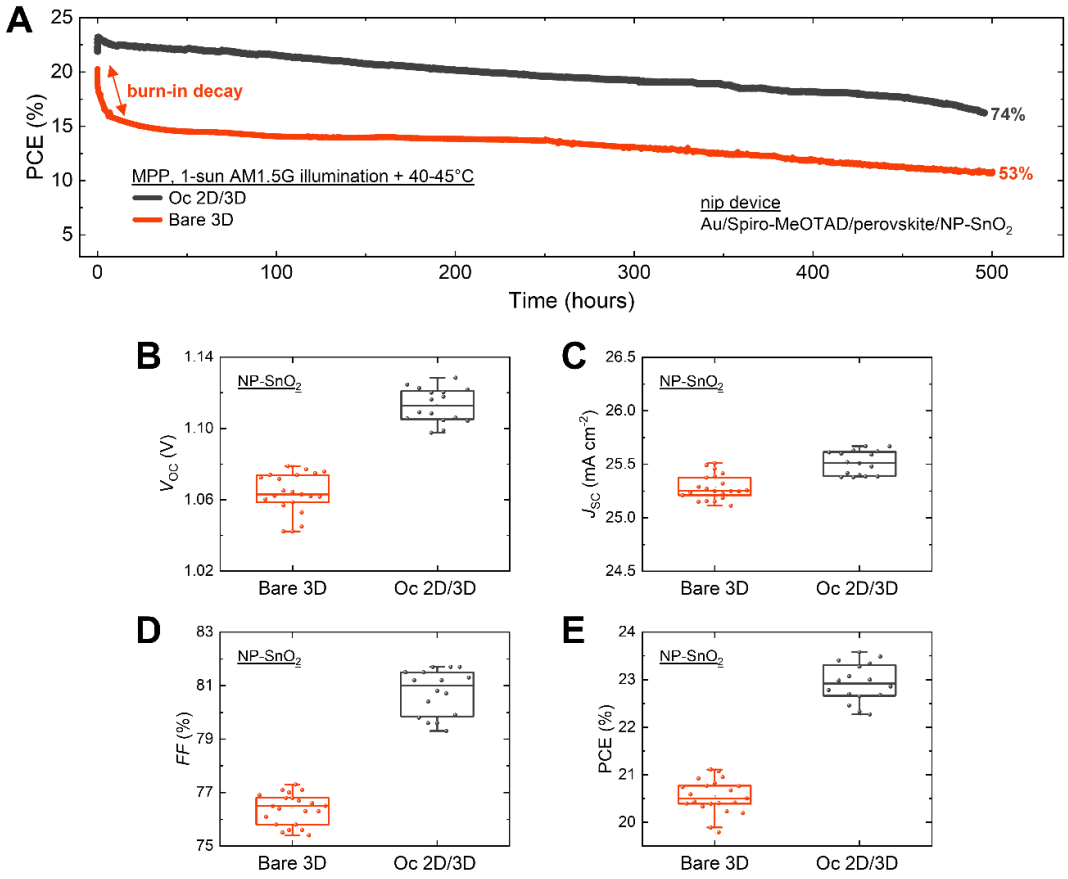

Fig. S1. (**A**) MPP tracking under 1-sun AM1.5G illumination (UV included) of the devices at 40-45°C in a nitrogen atmosphere. Box plots showing the distribution of the photovoltaic parameters of (**B**) V_{OC}, (**C**) J_{SC}, (**D**) *FF*, and (**E**) PCE of the devices. The devices use NP-SnO_2 as the electron-transporting layer.

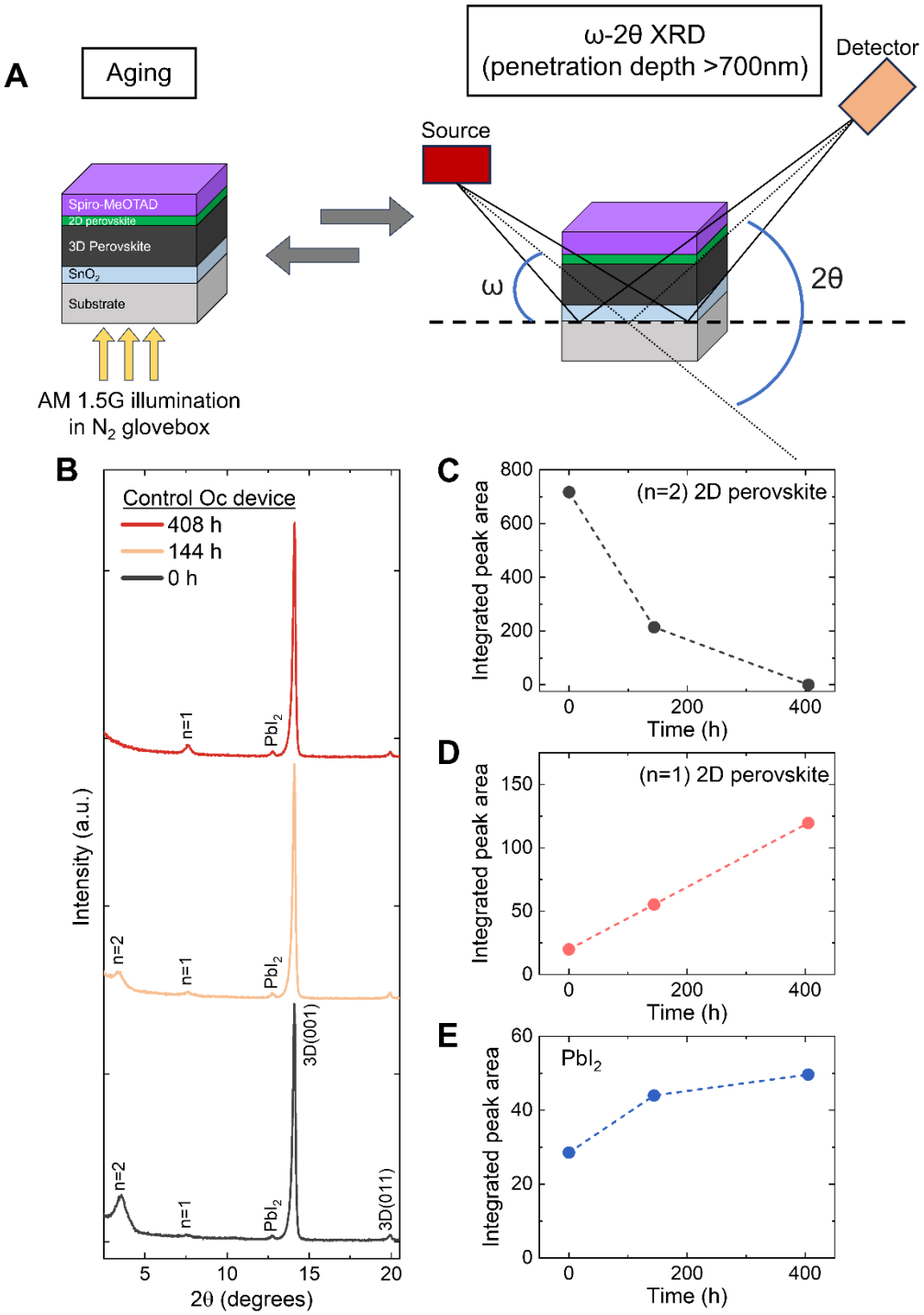

Fig. S2. (**A**) Schematic showing the aging experiment setup and static coupled-geometry (ω-2θ) XRD. (**B**) XRD patterns of the control Oc 2D/3D perovskite aged under 1-sun AM 1.5G illumination in open-circuit condition in a nitrogen glovebox. The XRD was performed on devices of structure spiro-MeOTAD/2D perovskite/3D perovskite/SnO_2/FTO. The 2D perovskite was thus buried under the spiro-MeOTAD layer for these measurements. The ω-2θ XRD has sufficient penetration depth to probe through the spiro-MeOTAD to investigate the buried 2D interlayer and 3D bulk perovskite. Evolution of the (**C**) 2D(n=2) perovskite, (**D**) 2D(n=1) perovskite, and (**E**) PbI_2 integrated peak areas. The time elapsed refers only to the illumination time.

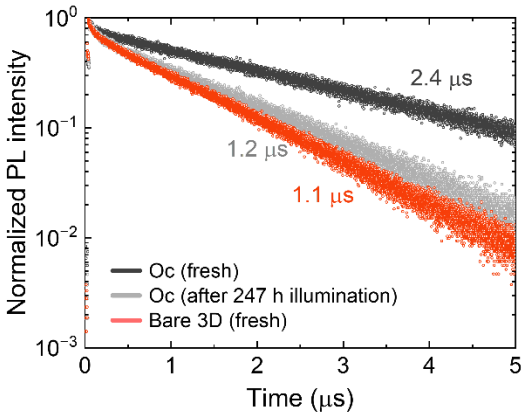

Fig. S3. Time-resolved PL spectra of the same Oc 2D/3D perovskite before (in black) and after (in gray) aging. The film was aged under 1-sun AM 1.5G illumination in a nitrogen glovebox. The fresh bare 3D perovskite (no aging) is also shown for comparison. All films were deposited on glass substrates.

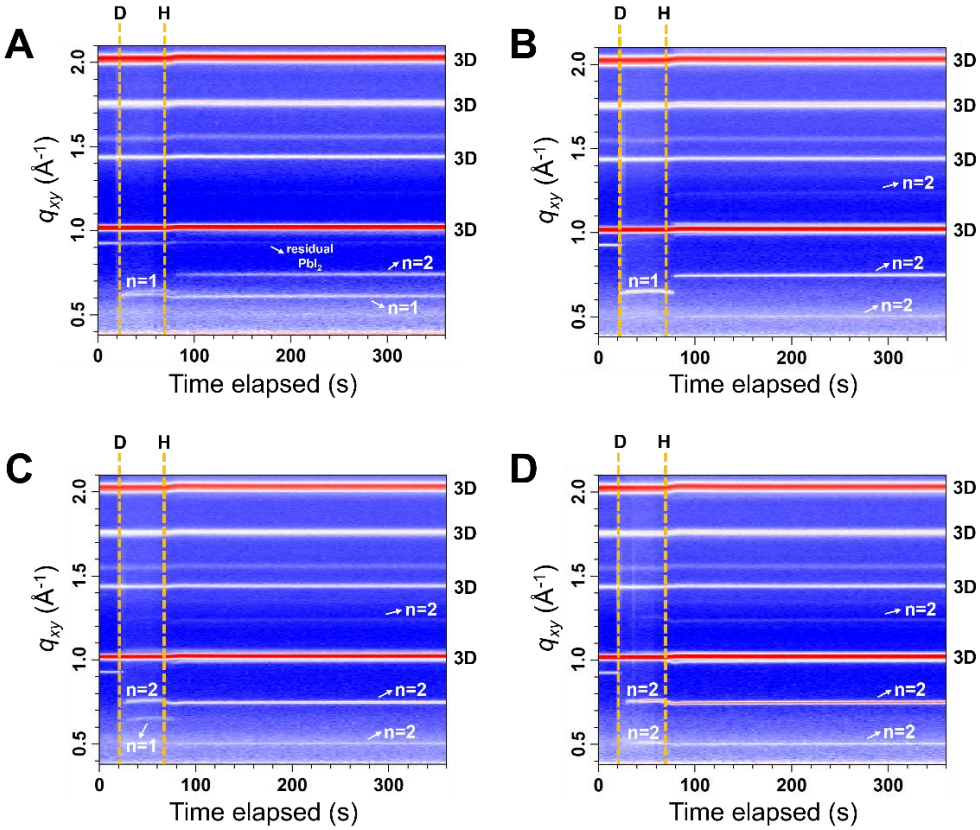

Fig. S4. Longer timescale (360 seconds) in situ GIWAXS measurements of the (**A**) Oc, (**B**) OcMA, (**C**) OcMA:F, and (**D**) OcMA:S 2D/3D perovskites. Labels "D" and "H" denote the deposition time and annealing start time, respectively.

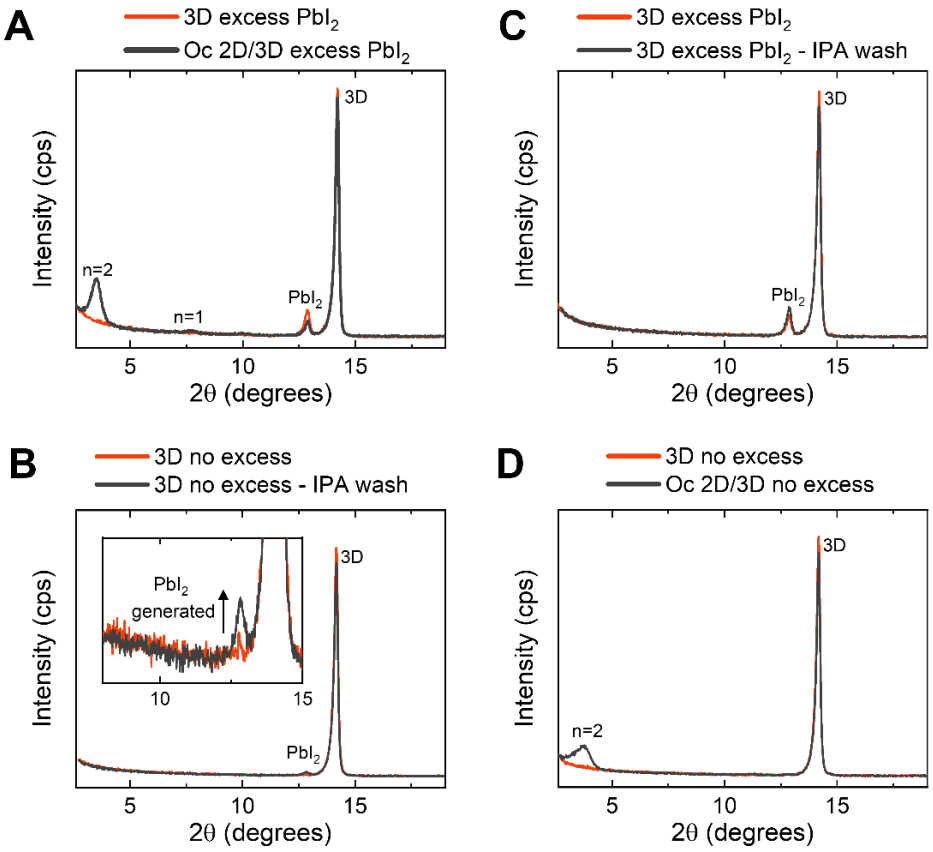

Fig. S5. (**A**) XRD spectra of the 3D and Oc 2D/3D perovskites, with excess PbI_2 composition. (**B**) XRD spectra of the 3D perovskite, no excess composition, before and after being spincoated with pure IPA. (**C**) XRD spectra of the 3D perovskite, with excess PbI_2 composition, before and after being spincoated with pure IPA. (**D**) XRD spectra of the 3D and Oc 2D/3D perovskites, no excess composition.

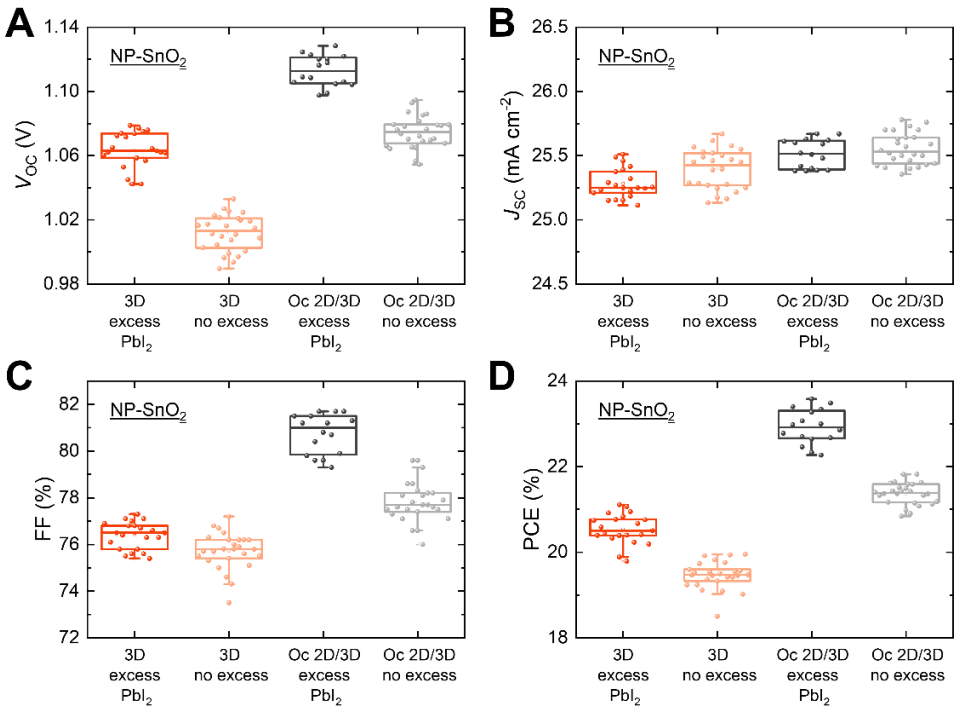

1065 **Fig. S6.** Box plots showing the distribution of the photovoltaic parameters of (**A**) V_{OC}, (**B**) J_{SC}, (**C**) *FF*, and (**D**) PCE of the 2D/3D and bare 3D devices with or without excess PbI_2. The devices use NP-SnO_2 as the electron-transporting layer.

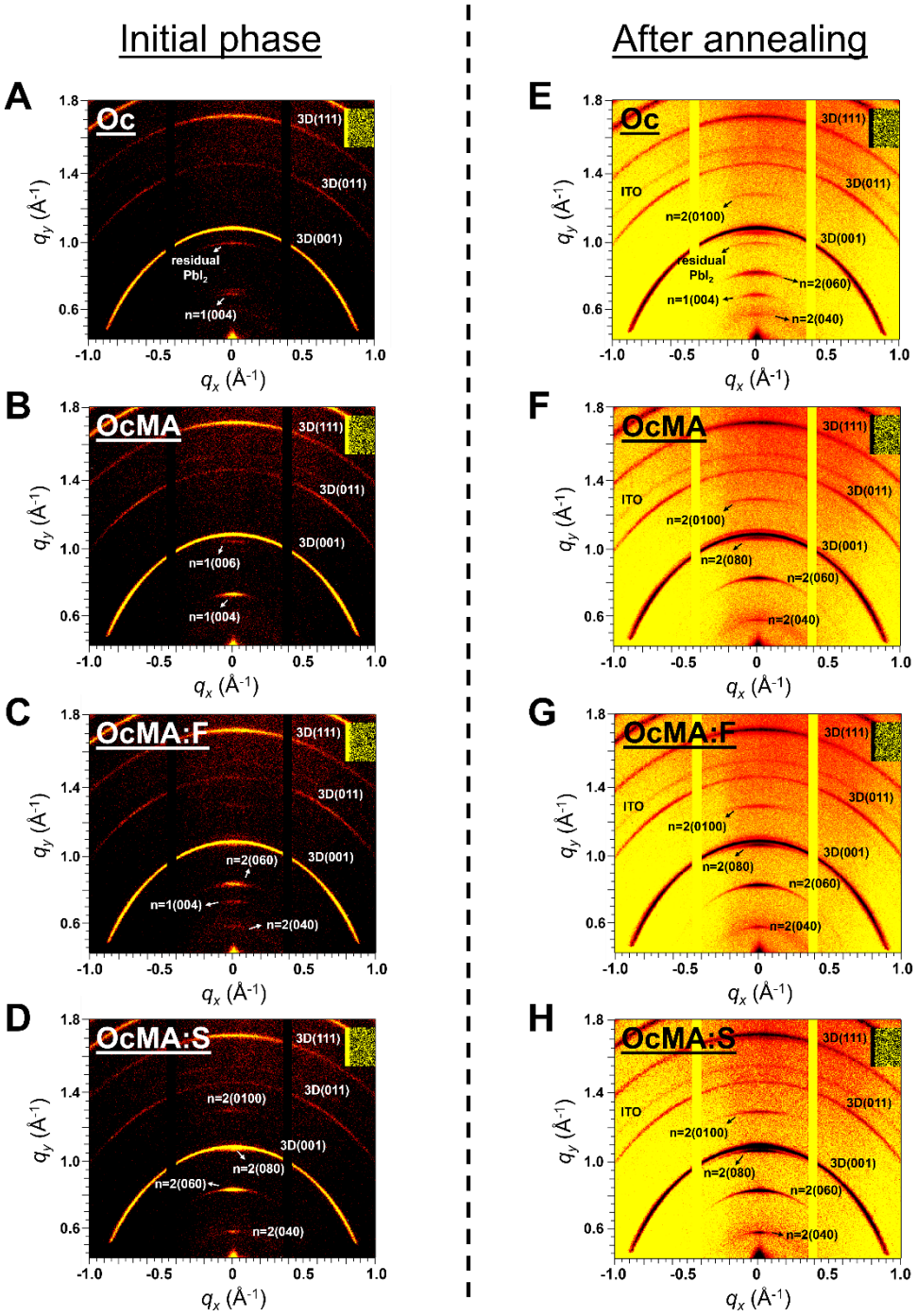

Fig. S7. GIWAXS spectra of the 2D initial phase of the (**A**) Oc, (**B**) OcMA, (**C**) OcMA:F, and (**D**) OcMA:S 2D/3D perovskites. GIWAXS spectra of the final 2D phase of the (**E**) Oc, (**F**) OcMA, (**G**) OcMA:F, and (**H**) OcMA:S 2D/3D perovskites.

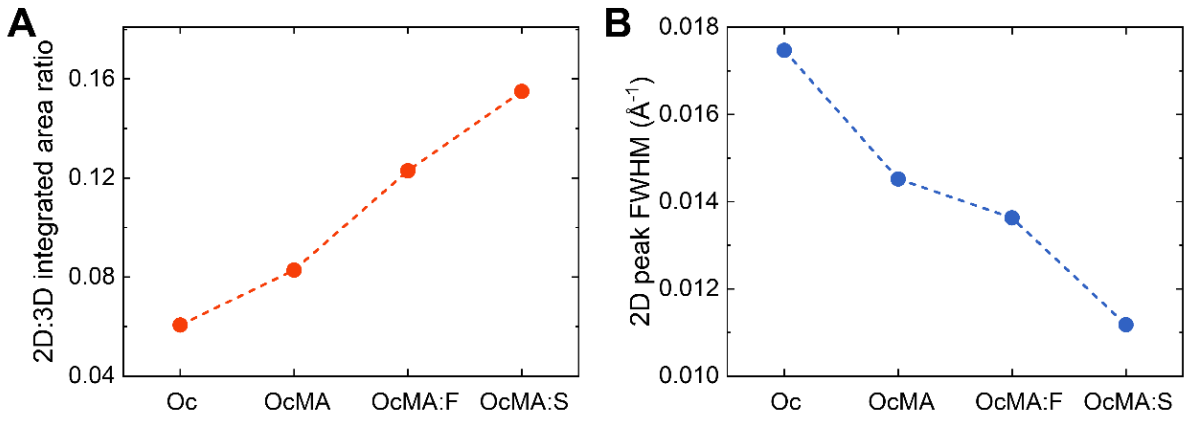

Fig. S8. (**A**) Ratio of the 2D(n=2) to 3D(001) integrated peak areas, and (**B**) FWHM of the 2D(n=2) peak, for the final 2D/3D perovskites obtained from the GIWAXS spectra. Based on the Debye-Scherrer law, crystallite size is inversely proportional to the FWHM. Therefore, the OcMA:S 2D/3D perovskite has the highest crystallinity with the largest crystallite size.

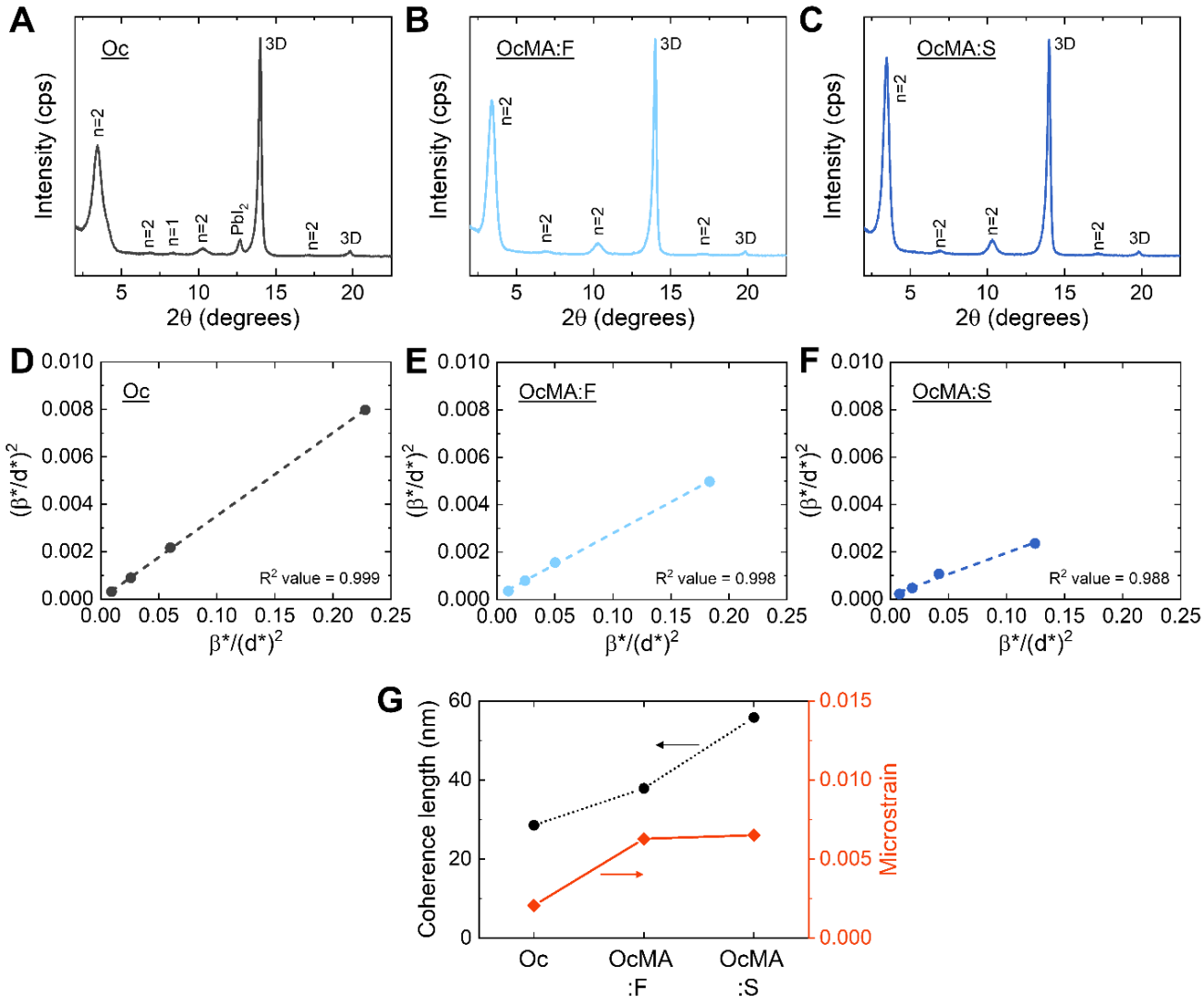

Fig. S9. Lab-based static high-resolution grazing-incidence XRD spectra of the (**A**) Oc, (**B**) OcMA:F, and (**C**) OcMA:S 2D/3D perovskites. Halder-Wagner plot of the (**D**) Oc, (**E**) OcMA:F, and (**F**) OcMA:S 2D(n=2) phase. (**G**) Halder-Wagner analysis (*47*) of the coherence length and microstrain of the 2D(n=2) phase.

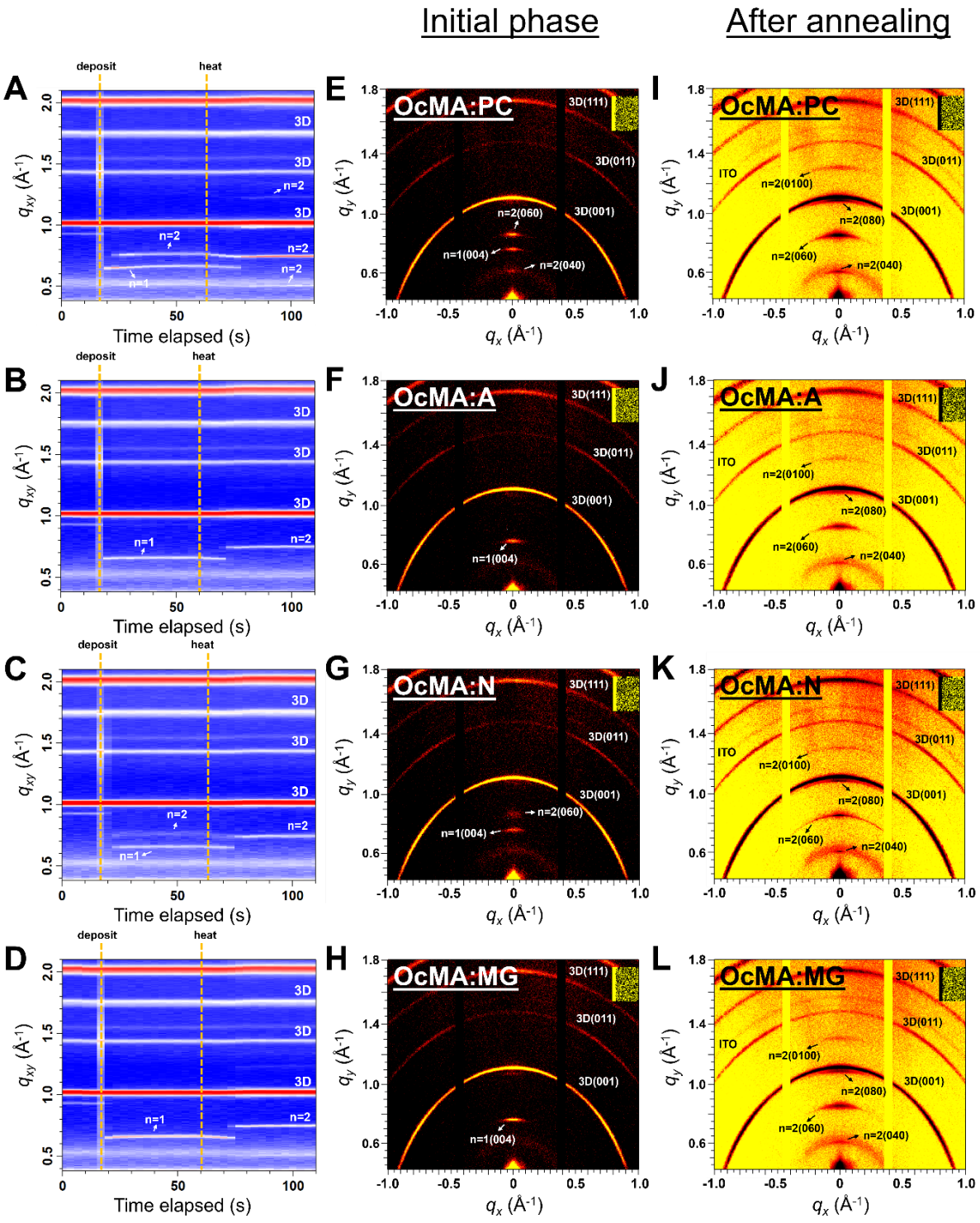

Fig. S10. In situ GIWAXS measurements of the (**A**) OcMA:PC, (**B**) OcMA:A, (**C**) OcMA:N, and (**D**) OcMA:MG 2D/3D perovskites. GIWAXS spectra of the 2D initial phase of the (**E**) OcMA:PC, (**F**) OcMA:A, (**G**) OcMA:N, and (**H**) OcMA:MG 2D/3D perovskites. GIWAXS spectra of the final 2D phase of the (**I**) OcMA:PC, (**J**) OcMA:A, (**K**) OcMA:N, and (**L**) OcMA:MG 2D/3D perovskites.

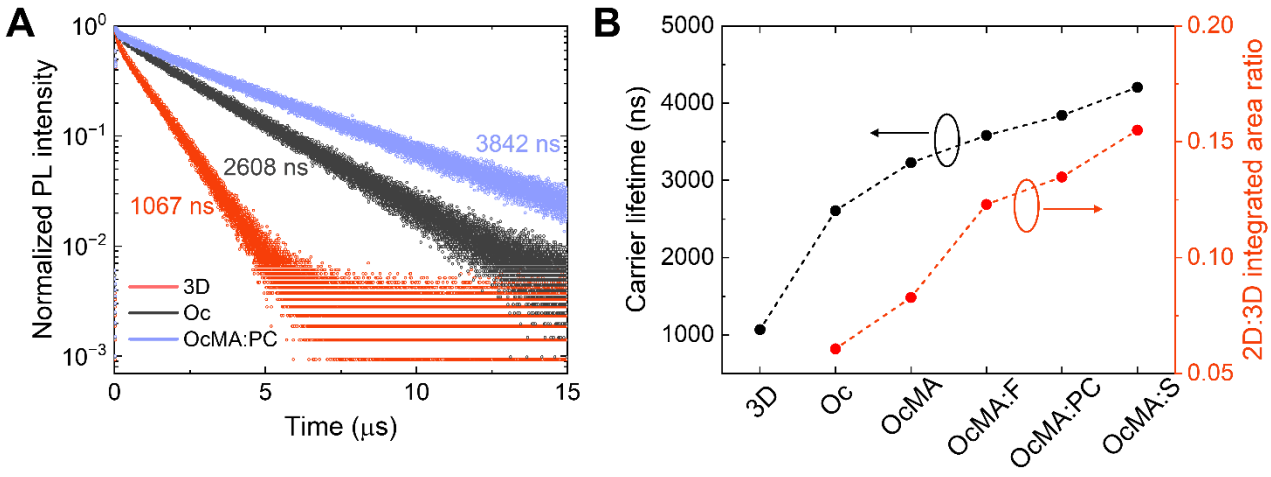

Fig. S11. (**A**) Time-resolved PL spectra of the OcMA:PC 2D/3D perovskite, in comparison to the bare 3D and Oc 2D/3D perovskite. All films were deposited on glass substrates. (**B**) Carrier lifetime (left axis) and 2D:3D integrated area ratio (right axis) of the 2D/3D perovskites. The 2D:3D integrated ratio is calculated as the ratio of the 2D(n=2)(060) to 3D(001) integrated peak areas for the final 2D/3D perovskites.

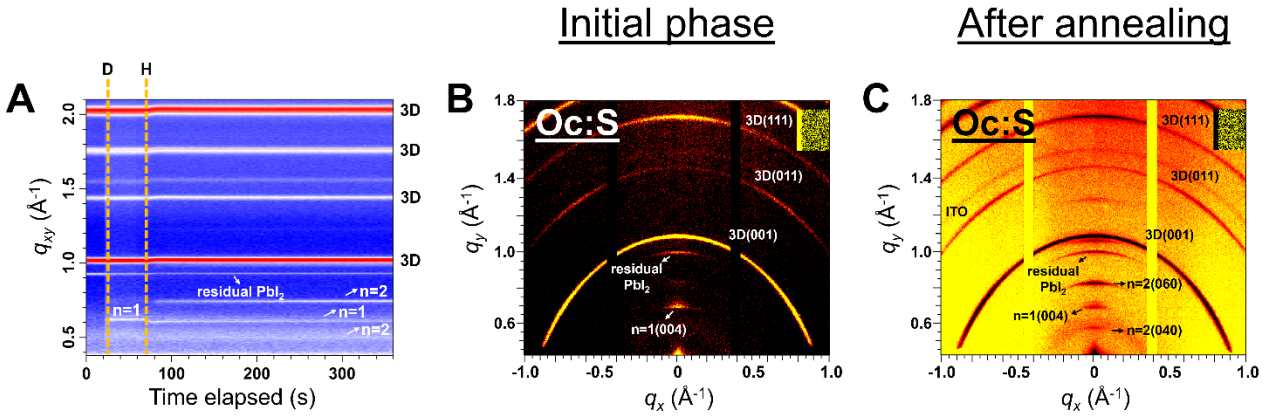

Fig. S12. (**A**) In situ GIWAXS measurements of the Oc:S 2D/3D perovskite. (**B**) GIWAXS spectra of the 2D initial phase of the Oc:S 2D/3D perovskite. (**C**) GIWAXS spectra of the final 2D phase of the Oc:S 2D/3D perovskite.

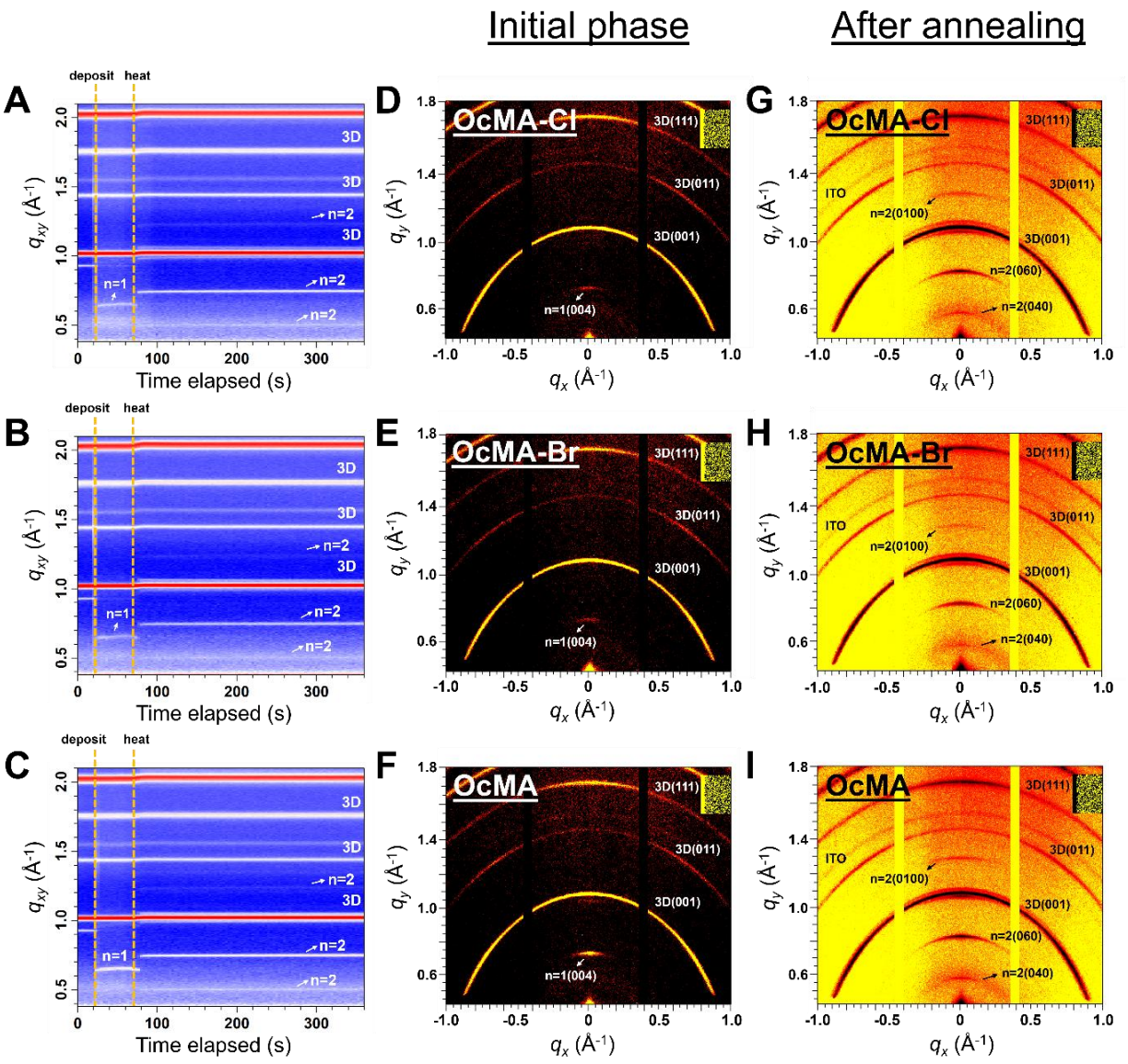

Fig. S13. In situ GIWAXS measurements of the (**A**) OcMA-Cl, (**B**) OcMA-Br, and (**C**) OcMA 2D/3D perovskites. GIWAXS spectra of the 2D initial phase of the (**D**) OcMA-Cl, (**E**) OcMA-Br, and (**F**) OcMA 2D/3D perovskites. GIWAXS spectra of the final 2D phase of the (**G**) OcMA-Cl, (**G**) OcMA-Br, and (**I**) OcMA 2D/3D perovskites.

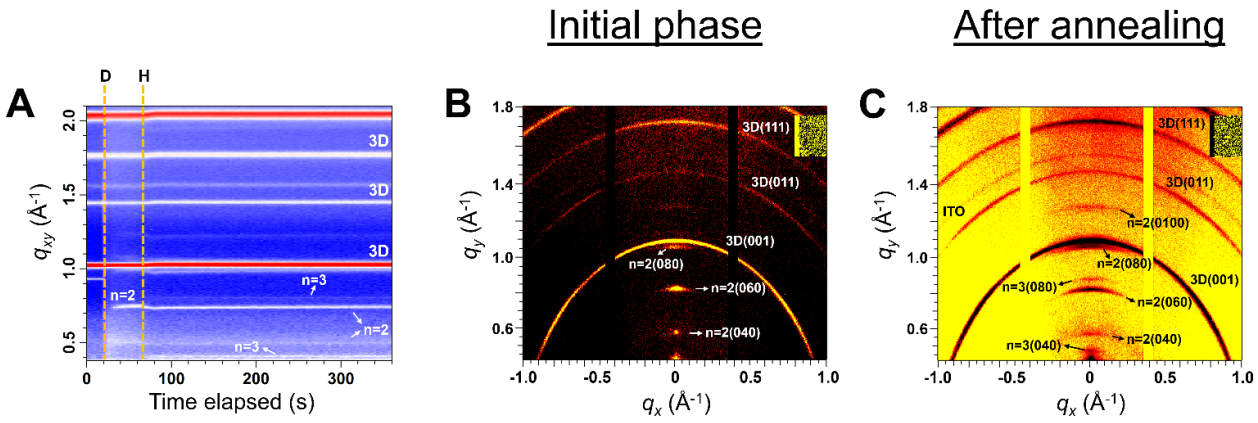

1115 **Fig. S14.** (**A**) In situ GIWAXS measurement of the OcMA:S 2D/3D perovskite, but using a higher concentration of methylammonium iodide. In this case, the Oc:MA:S ratio was 1:1:2.5. GIWAXS spectra of the (**B**) 2D initial phase, and (**C**) final 2D phase.

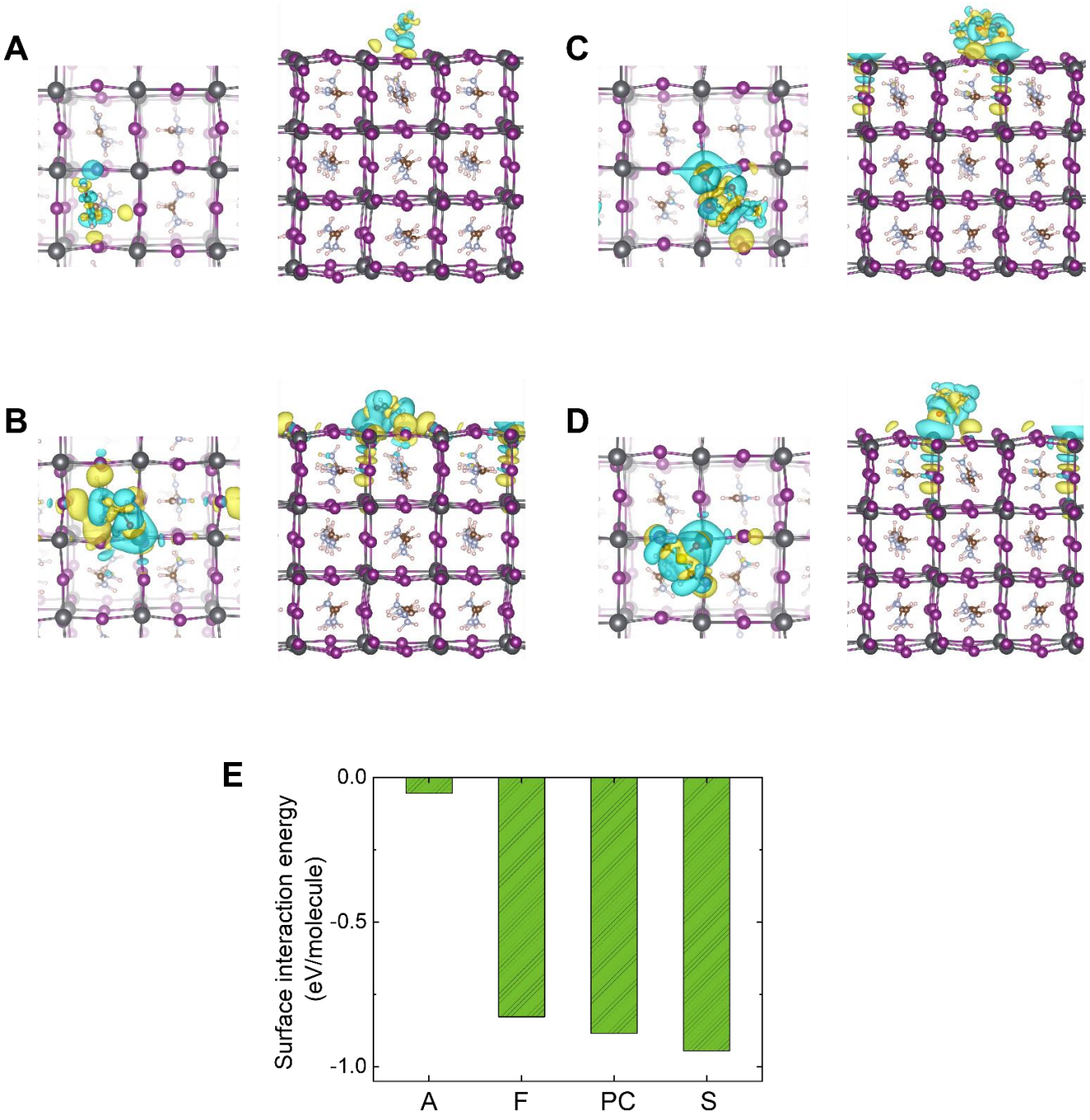

Fig. S15. Top view (left) and side view (right) slab models of the 3D perovskite surface bonded with (**A**) acetonitrile (A), (**B**) dimethylformamide (F), (**C**) propylene carbonate (PC), and (**D**) dimethylsulfoxide (S). (**E**) Interaction energy per solvent molecule with the 3D perovskite surface.

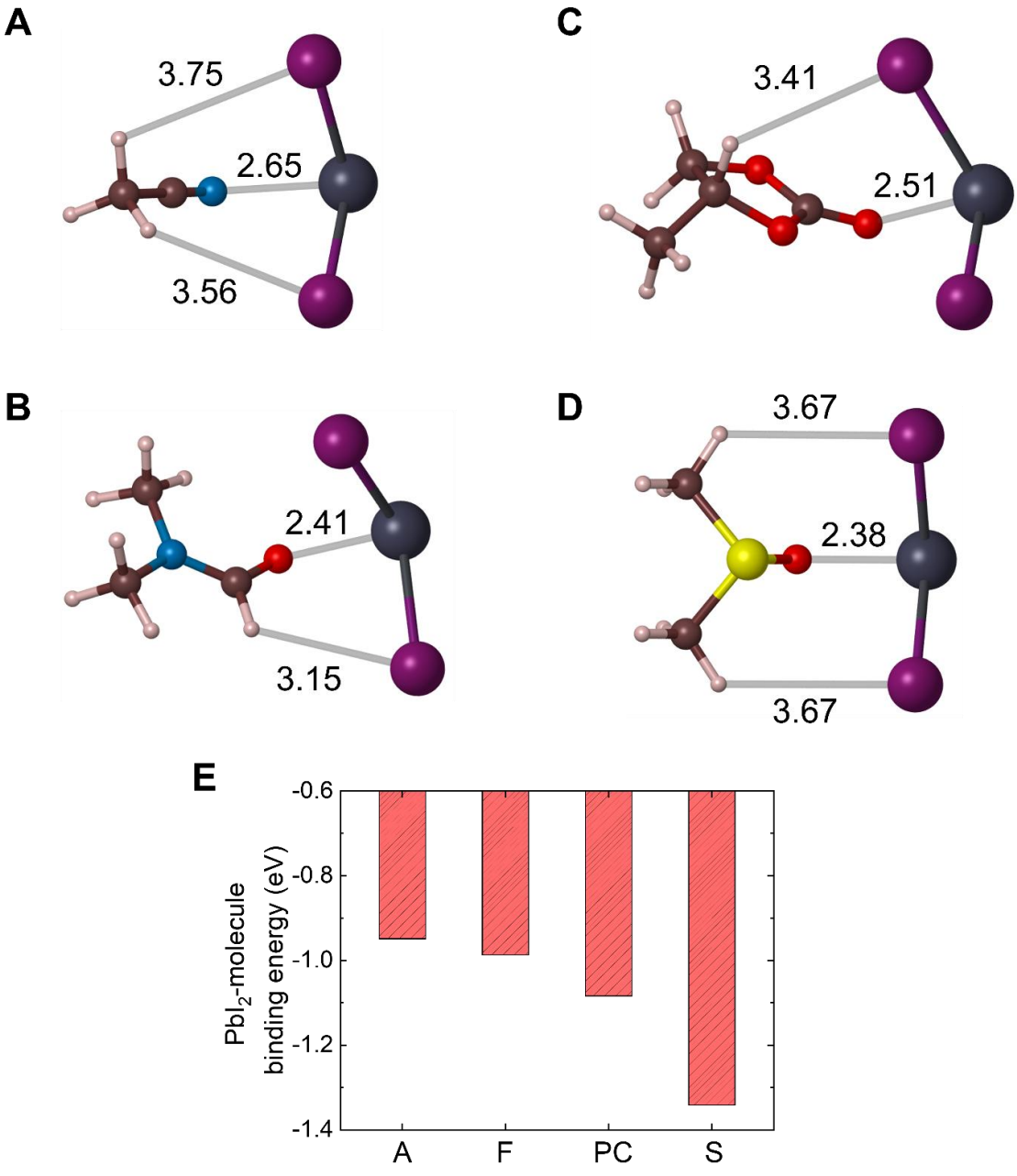

Fig. S16. Molecular configuration and binding with PbI_2 of (**A**) acetonitrile (A), (**B**) dimethylformamide (F), (**C**) propylene carbonate (PC), and (**D**) dimethylsulfoxide (S). (**E**) Binding energy per solvent molecule with PbI_2.

1130

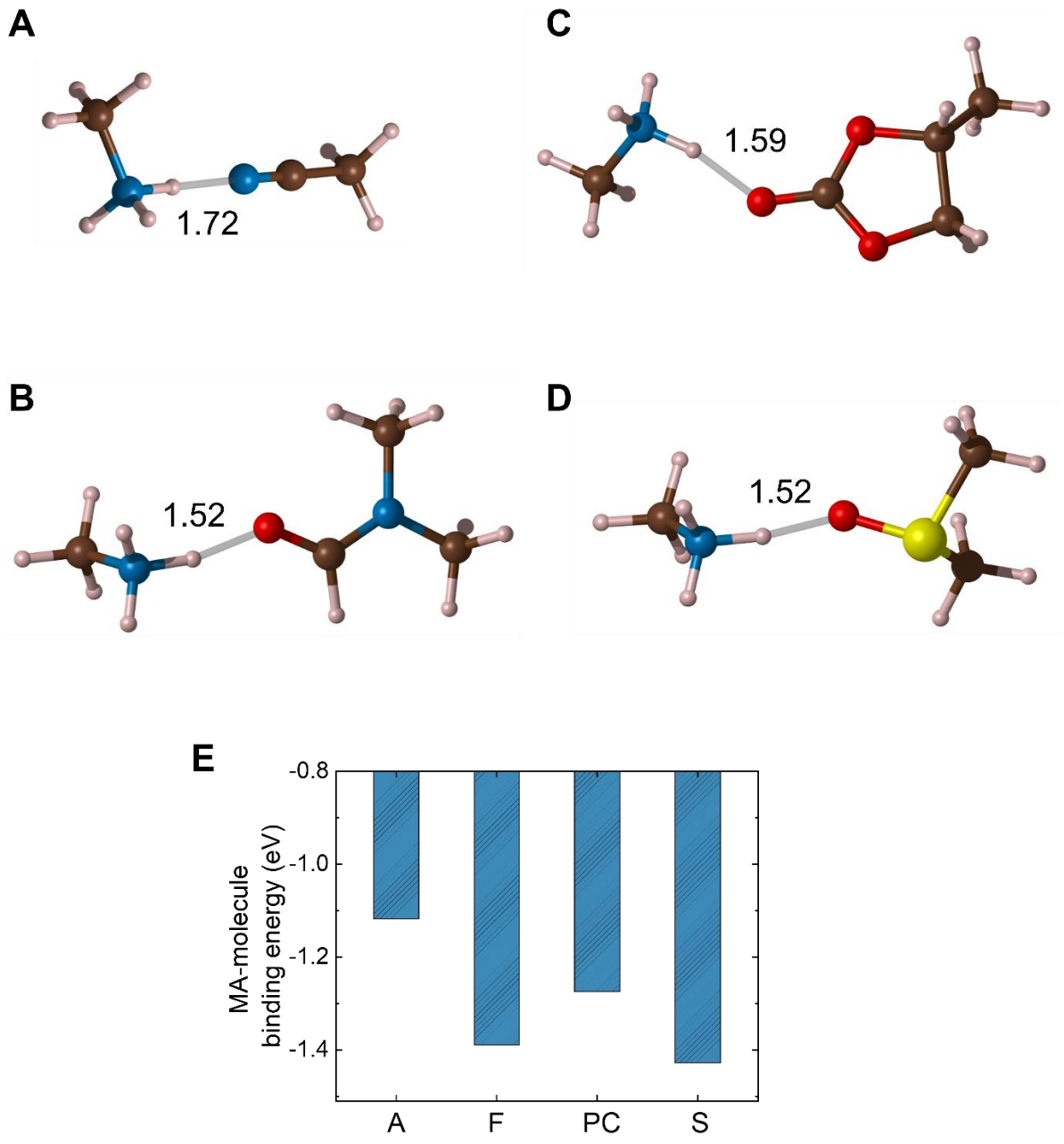

Fig. S17. Molecular configuration and binding with methylammonium of (**A**) acetonitrile (A), (**B**) dimethylformamide (F), (**C**) propylene carbonate (PC), and (**D**) dimethylsulfoxide (S). (**E**) Binding energy per solvent molecule with methylammonium.

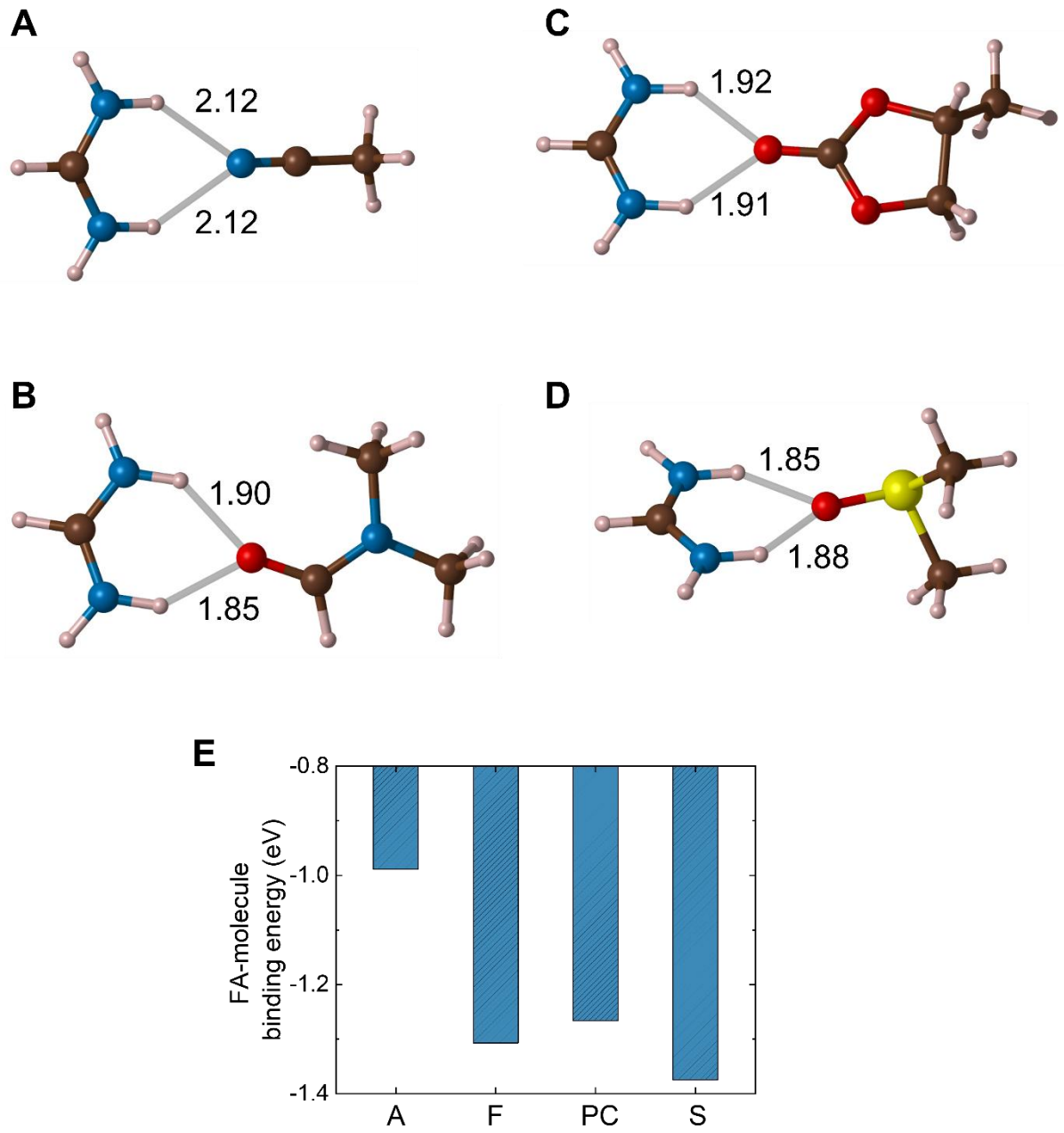

Fig. S18. Molecular configuration and binding with formamidinium of (**A**) acetonitrile (A), (**B**) dimethylformamide (F), (**C**) propylene carbonate (PC), and (**D**) dimethylsulfoxide (S). (**E**) Binding energy per solvent molecule with formamidinium.

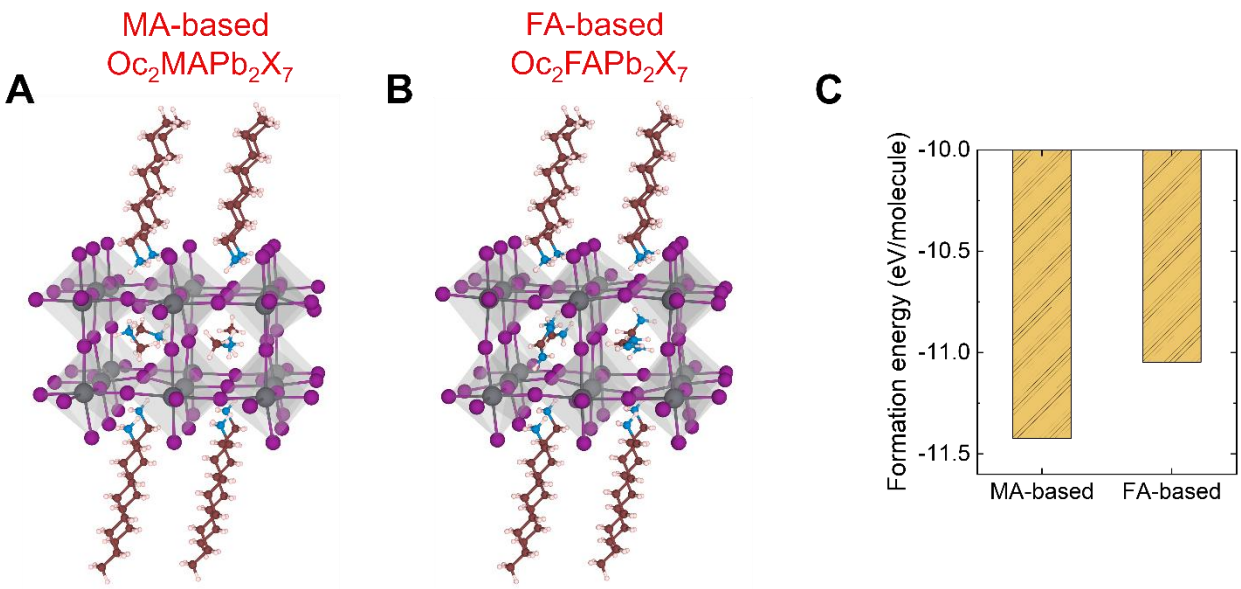

Fig. S19. Slab models of the 2D(n=2) perovskites with different A-site cation compositions of (**A**) MA, and (**B**) FA. (**C**) Formation energy per molecule of the 2D(n=2) perovskites.

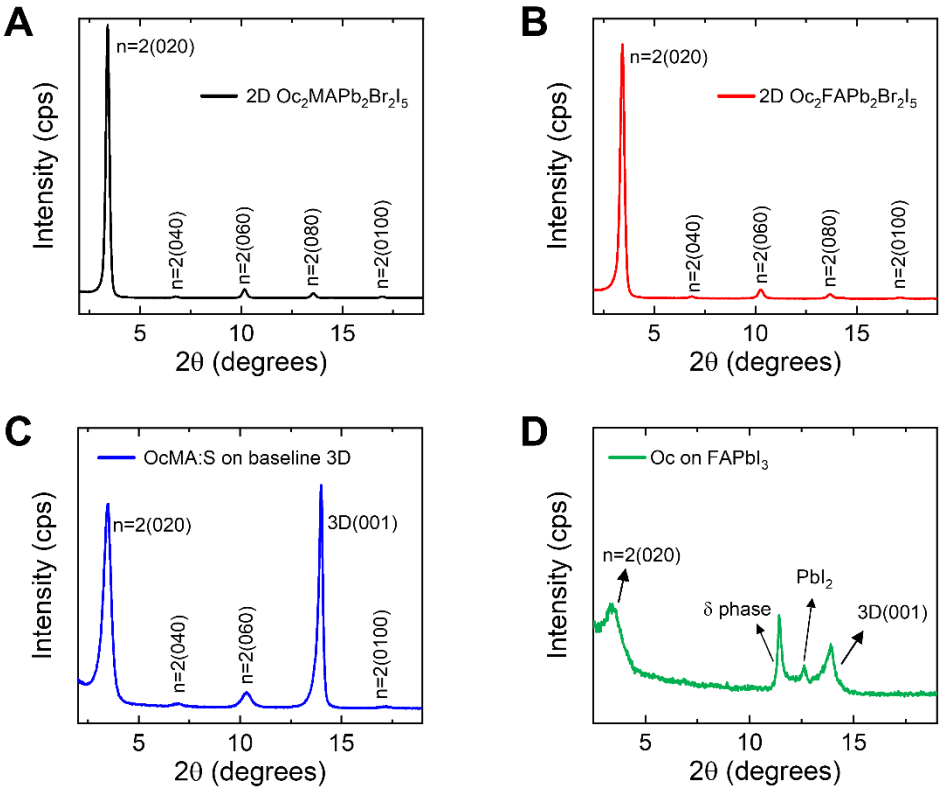

Fig. S20. XRD spectra of the 2D perovskites of (**A**) $OA_2MAPb_2Br_2I_5$ and (**B**) $OA_2FAPb_2Br_2I_5$. (**C**) XRD spectra of the OcMA:S 2D perovskite on our baseline 3D perovskite. This 3D perovskite contained excess PbI_2, MACl, and $MAPbBr_3$. (**D**) XRD spectra of the Oc 2D perovskite on 3D $FAPbI_3$. This 3D perovskite was a pure $FAPbI_3$ composition with only excess PbI_2.

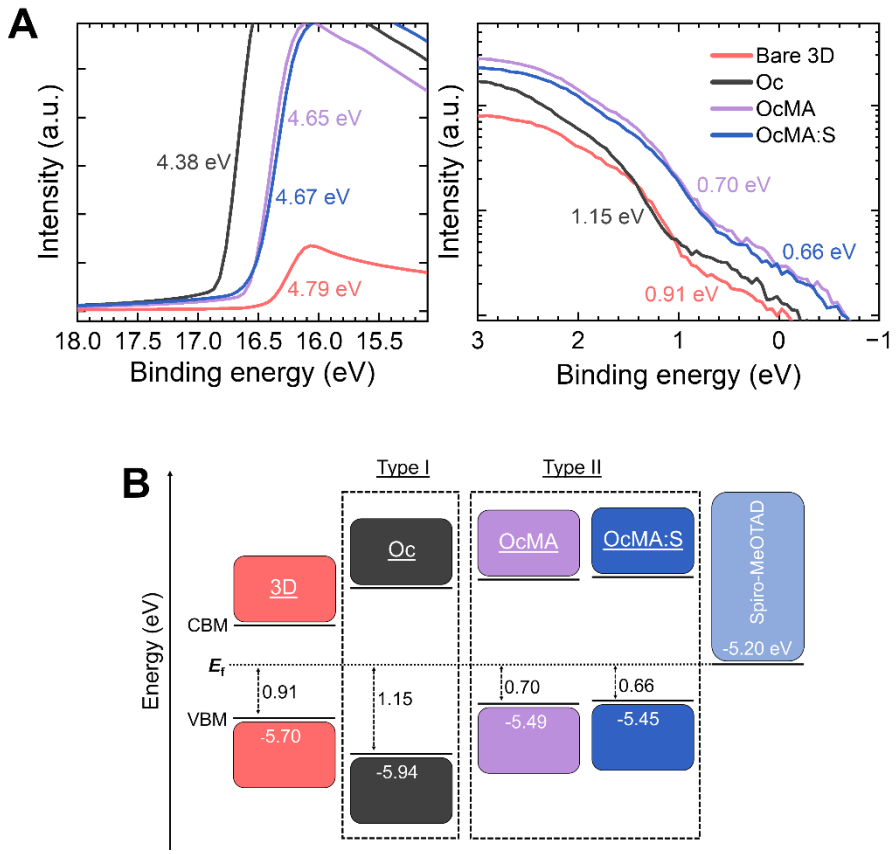

Fig. S21. (**A**) UPS secondary electron cut-offs (left) and valence band spectra (right) of the 2D/3D perovskites. (**B**) Band alignments constructed from the UPS results. The highest occupied molecular orbital (HOMO) level of the spiro-MeOTAD hole-transporting layer is also included.

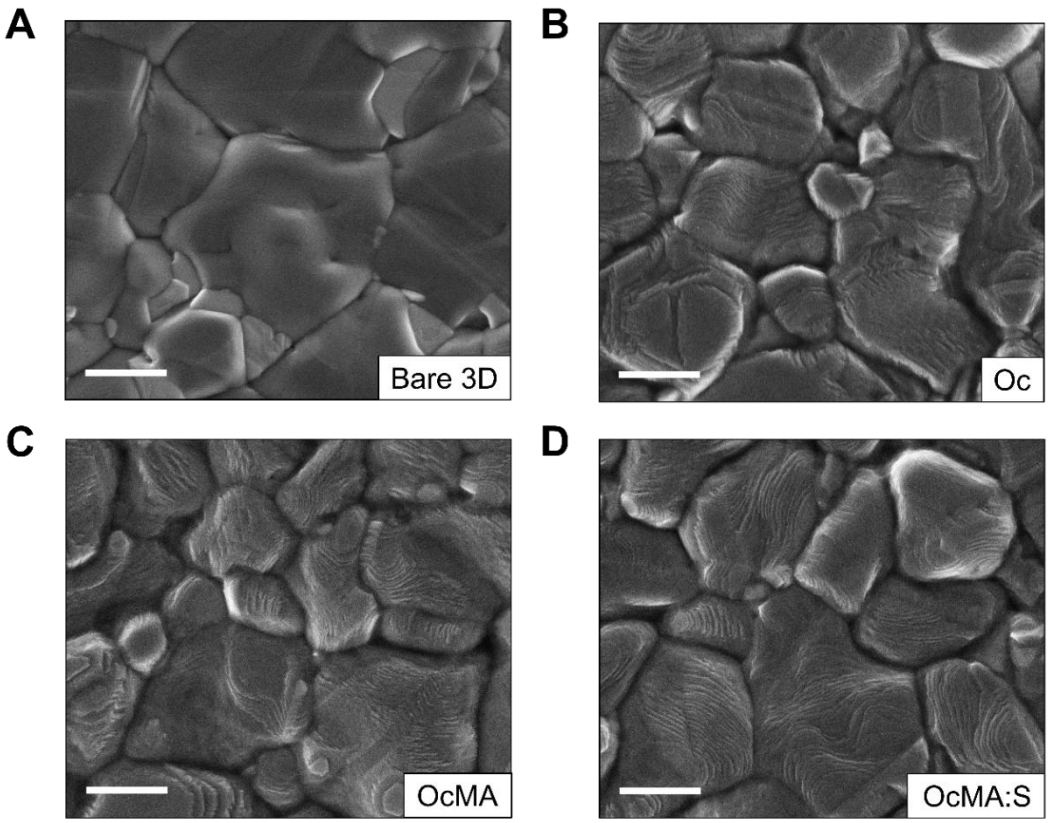

Fig. S22. Surface FE-SEM images of the (**A**) bare 3D, (**B**) Oc, (**C**) OcMA, and (**D**) OcMA:S 2D/3D perovskites. All scale bars are 600 nm.

1160

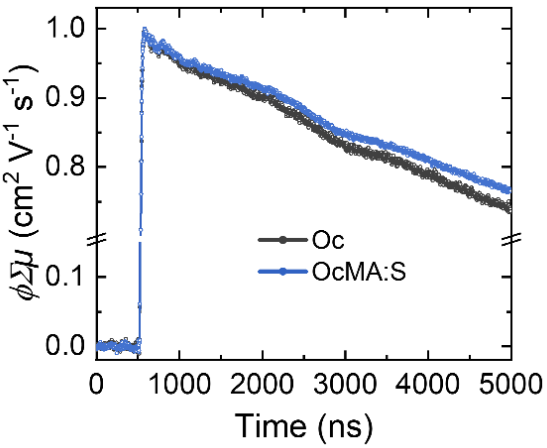

Fig. S23. Magnified time-resolved microwave conductivity (TRMC) transients of the control Oc and target OcMA:S 2D/3D perovskites on quartz.

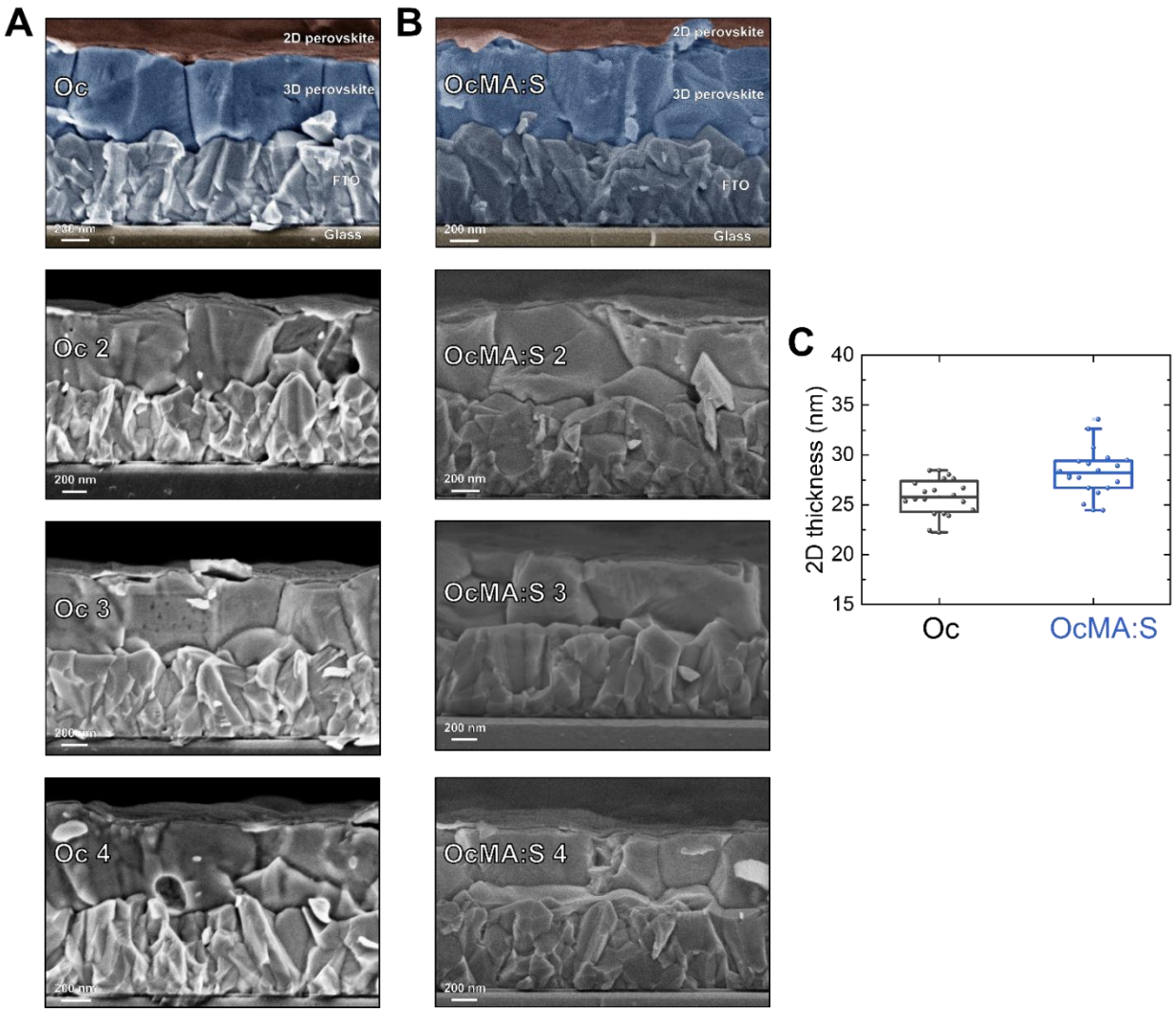

Fig. S24. Cross-sectional FE-SEM images of the (**A**) Oc and (**B**) OcMA:S 2D/3D perovskites. All scale bars are 200 nm. (**C**) Box plot showing the distribution of the 2D perovskite thickness measured from five different regions per image.

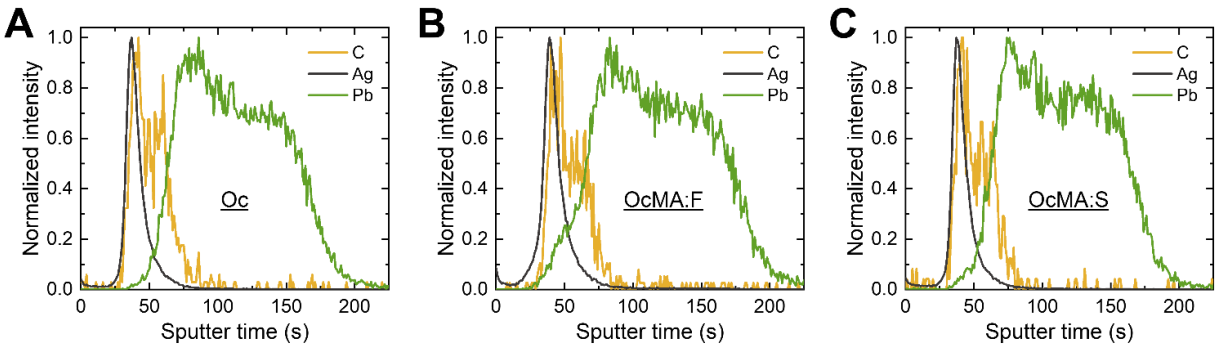

Fig. S25. Elemental depth profile of the (**A**) Oc, (**B**) OcMA:F, and (**C**) OcMA:S 2D/3D perovskites measured by time-of-flight secondary ion mass spectrometry (ToF-SIMS). We used an all-inorganic $CsPbI_2Br$ perovskite composition for this ToF-SIMS profiling. This allowed us to isolate the signal from carbon, which must originate only from the 2D perovskite.

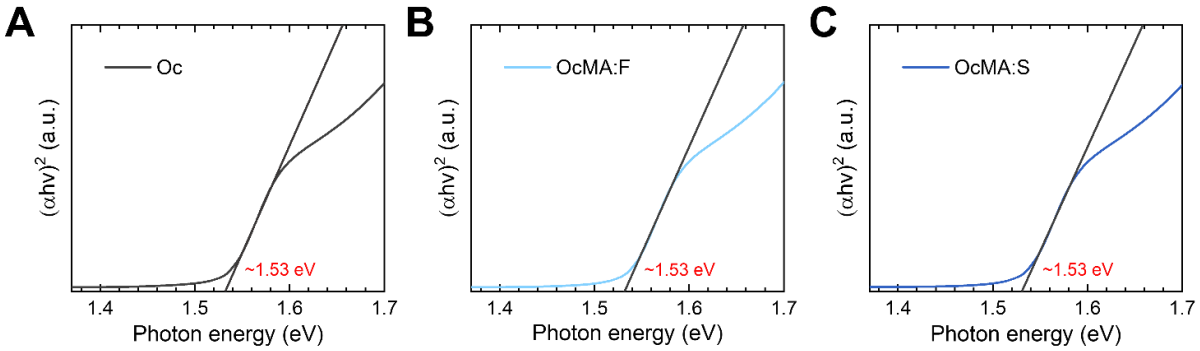

Fig. S26. Tauc plot of the (**A**) Oc, (**B**) OcMA:F, and (**C**) OcMA:S 2D/3D perovskites. Calculated bandgap values are given in red.

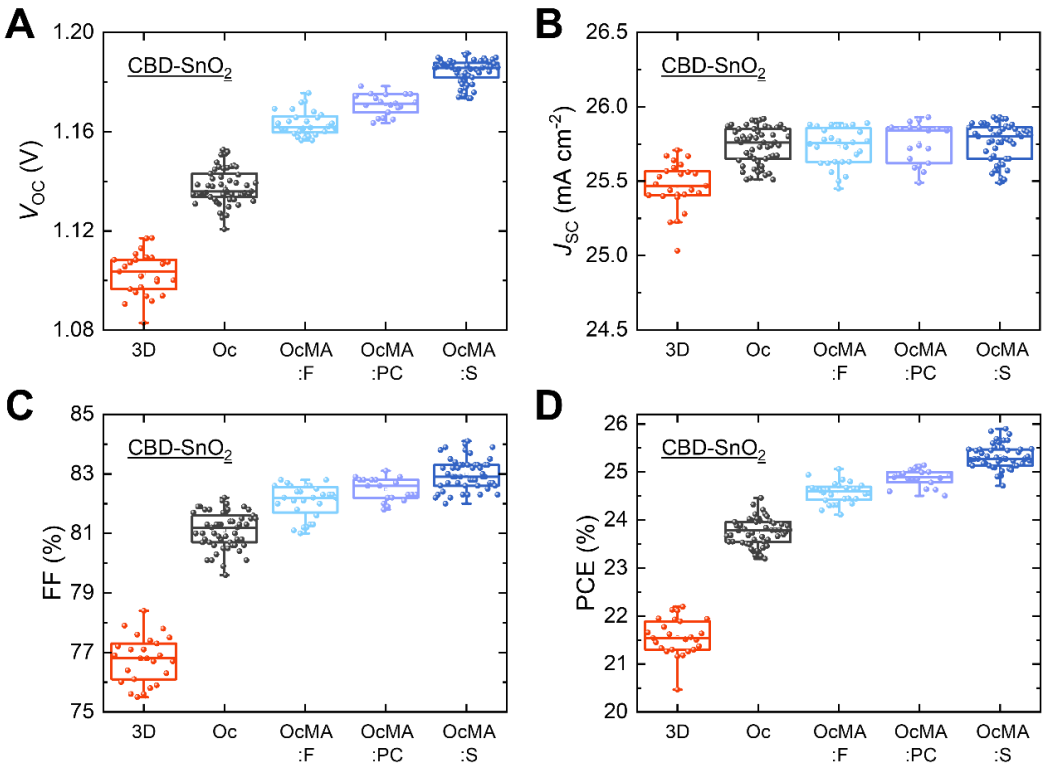

Fig. S27. Box plots showing the distribution of the photovoltaic parameters of (**A**) V_{OC}, (**B**) J_{SC}, (**C**) *FF*, and (**D**) PCE of the devices. The devices use CBD-SnO_2 as the electron-transporting layer.

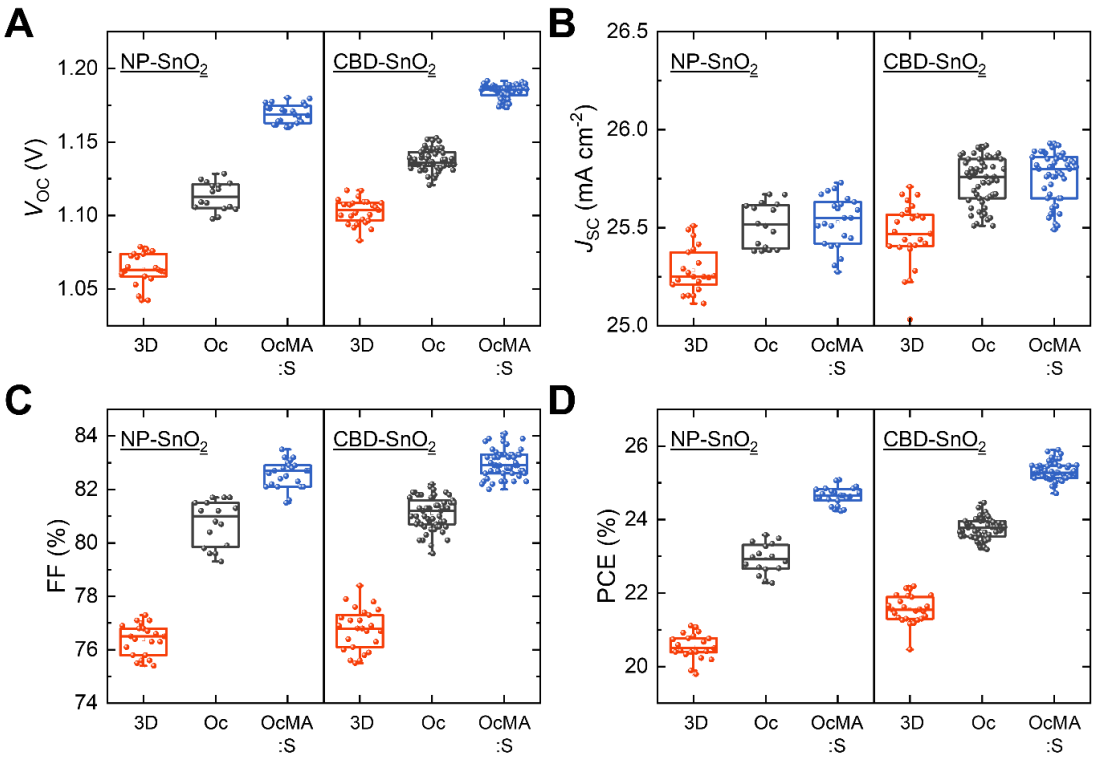

Fig. S28. Box plots comparing the distribution of the photovoltaic parameters of (**A**) V_{OC}, (**B**) J_{SC}, (**C**) *FF*, and (**D**) PCE of the devices with NP-SnO_2 or CBD-SnO_2.

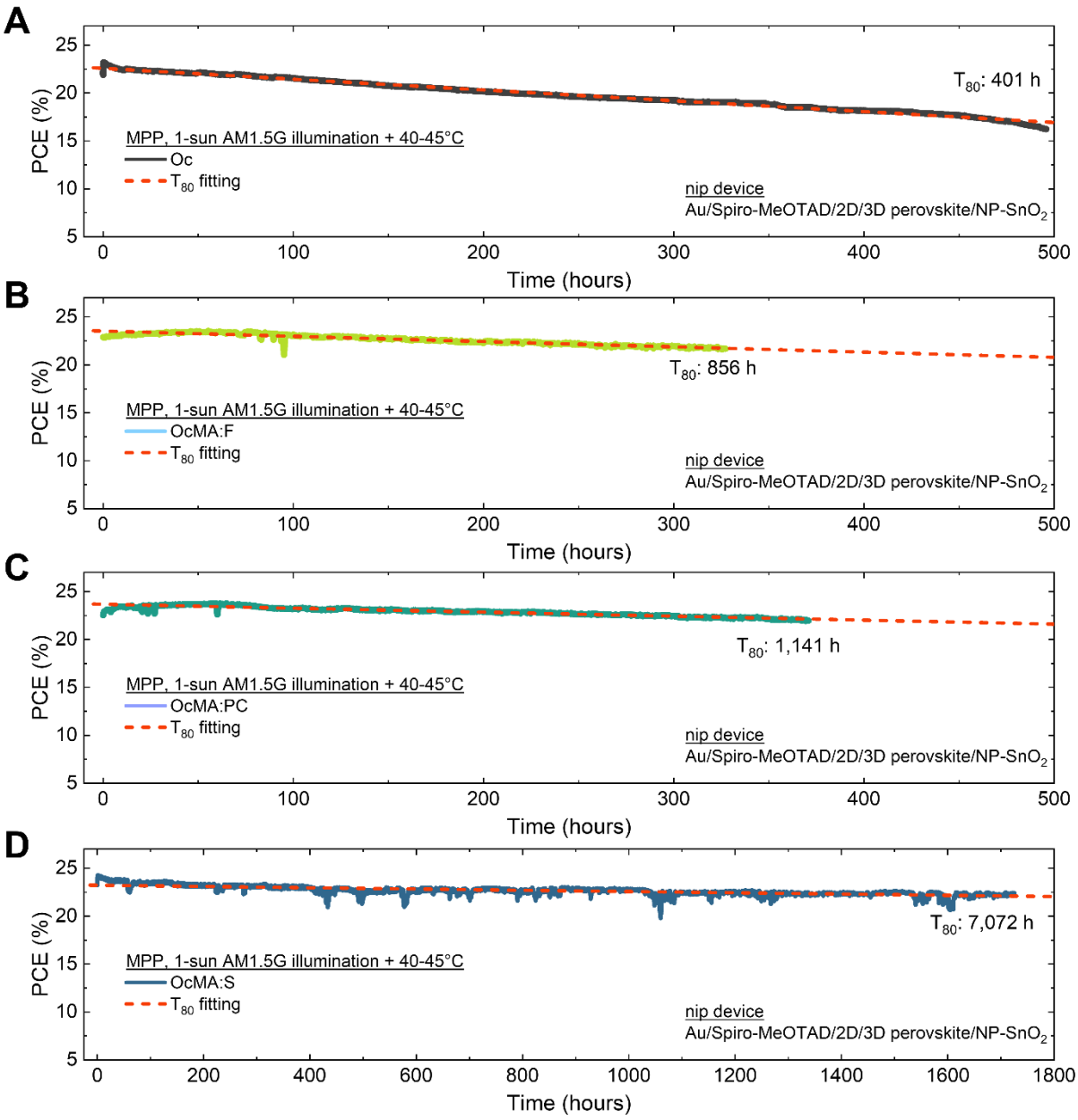

Fig. S29. MPP tracking under 1-sun AM1.5G illumination (UV included) of the devices at 40-45°C in a nitrogen atmosphere of the (**A**) Oc, (**B**) OcMA:F, (**C**) OcMA:PC, and (**D**) OcMA:S devices. The T_{80} lifetime is define as the linearly extrapolated time to reach 80% of the initial device PCE. The devices use NP-SnO_2 as the electron-transporting layer.

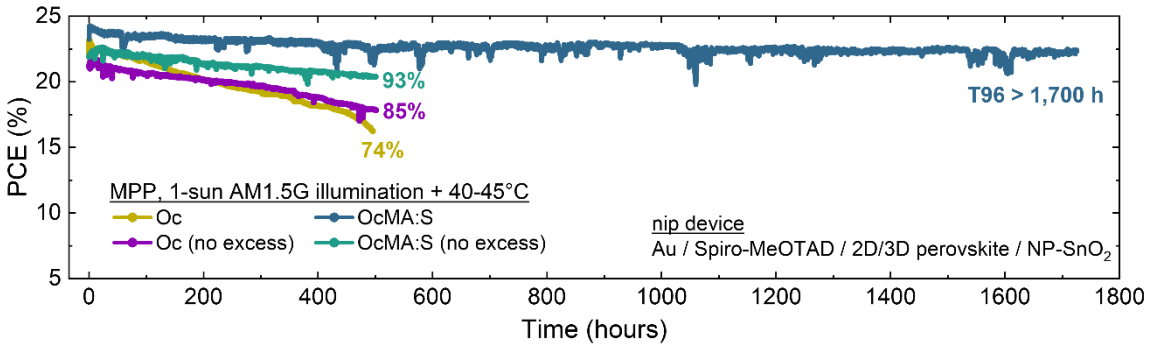

Fig. S30. MPP tracking under 1-sun AM1.5G illumination (UV included) of the devices with or without excess PbI_2 at 40-45°C in a nitrogen atmosphere.

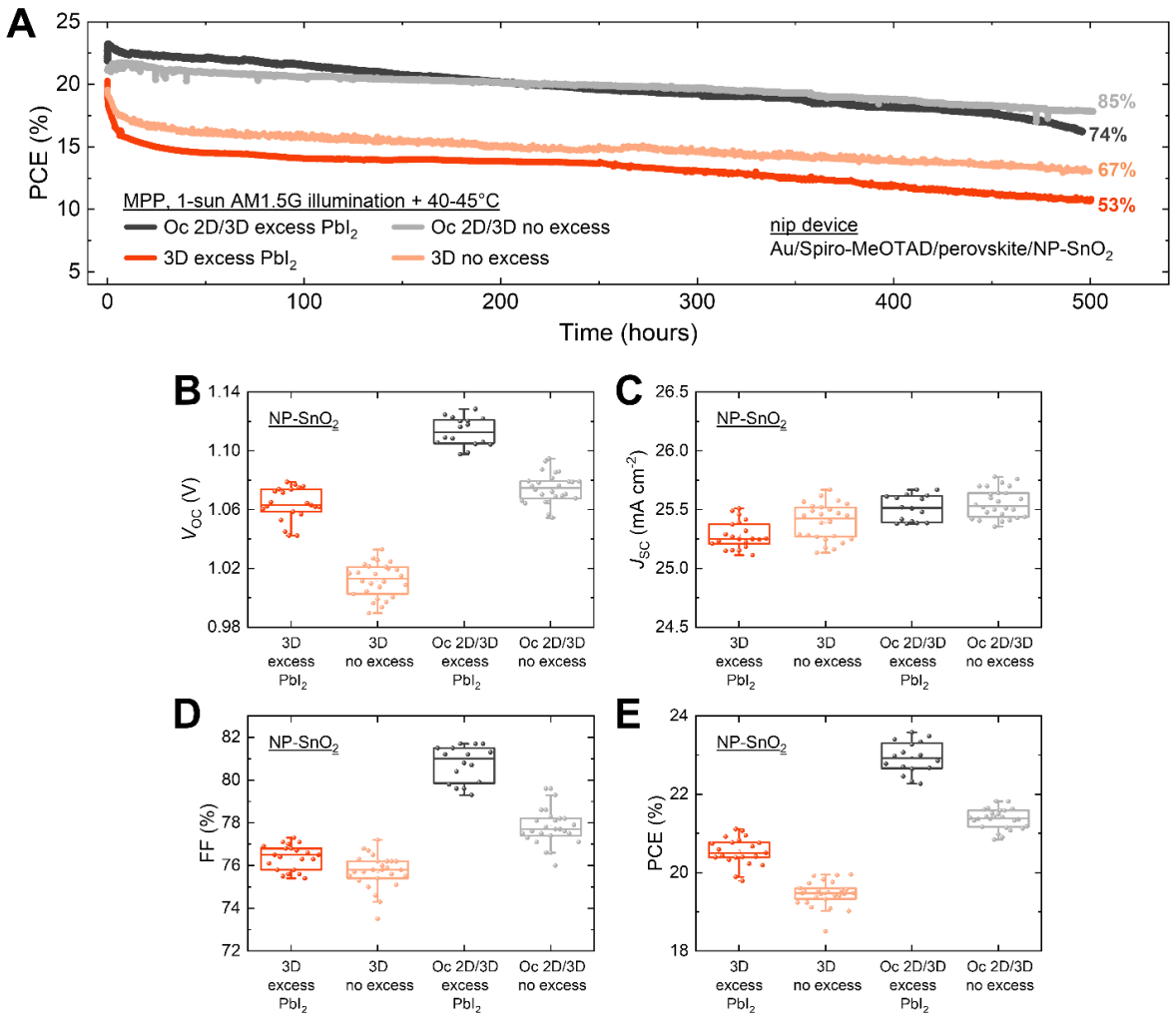

Fig. S31. (**A**) MPP tracking under 1-sun AM1.5G illumination (UV included) of the devices at 40-45°C in a nitrogen atmosphere. Box plots showing the distribution of the photovoltaic parameters of (**B**) V_{OC}, (**C**) J_{SC}, (**D**) *FF*, and (**E**) PCE of the devices. The devices use NP-SnO_2 as the electron-transporting layer.

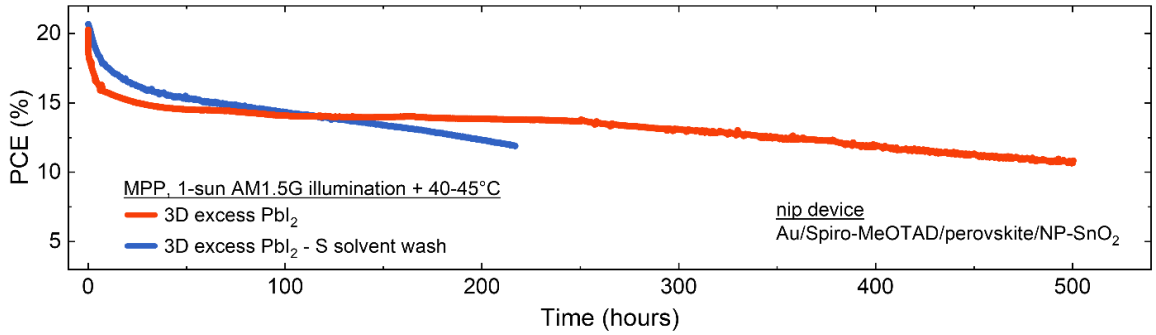

Fig. S32. MPP tracking under 1-sun AM1.5G illumination (UV included) of the devices at 40-45°C in a nitrogen atmosphere. For the "3D excess PbI_2 – S solvent wash" device, we spincoated the solvent S (i.e. dimethylsulfoxide and IPA mixed solvent) by itself without 2D perovskite on to the bare 3D perovskite.

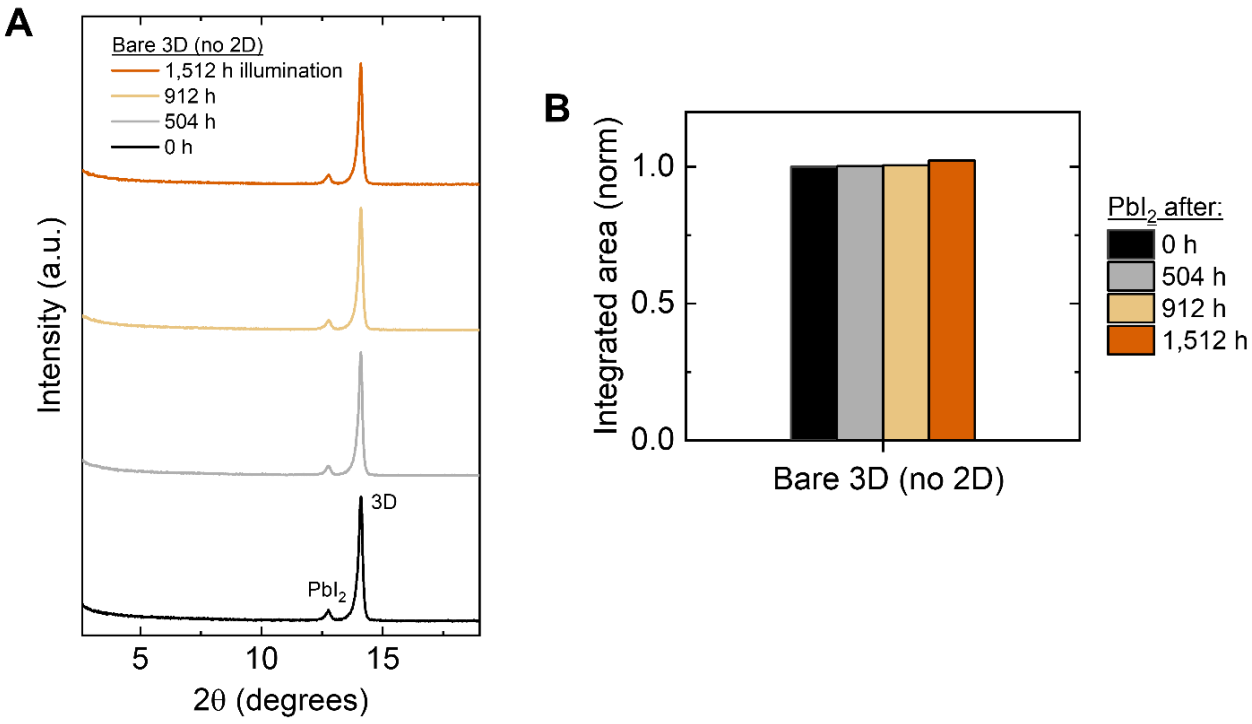

Fig. S33. (**A**) XRD patterns of the bare 3D (no 2D) perovskite aged under 1-sun AM 1.5G illumination in a N_2 glovebox. The XRD was performed on devices of structure spiro-MeOTAD/2D perovskite/3D perovskite/SnO_2/FTO. (**B**) Evolution of the PbI_2 integrated peak area. The time elapsed refers only to the time under illumination.

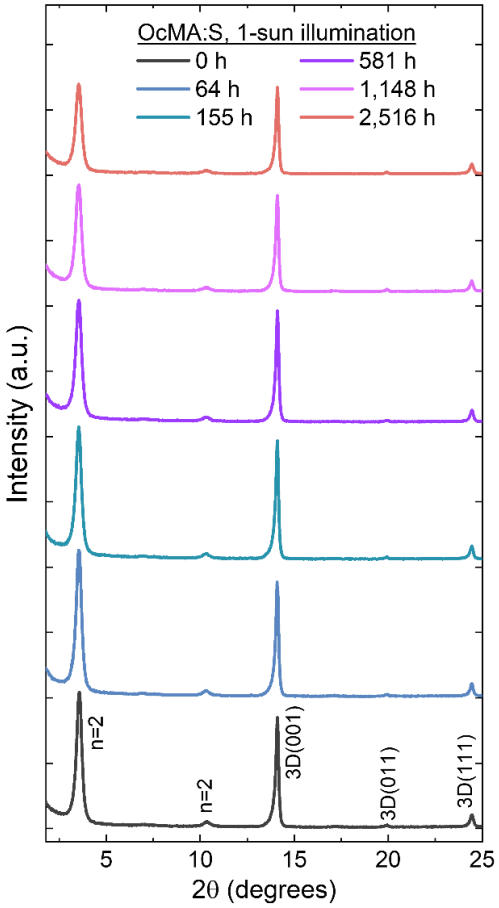

Fig. S34. XRD patterns of the OcMA:S 2D/3D perovskite aged under 1-sun AM 1.5G illumination in a N_2 glovebox. The XRD was performed on devices of structure spiro-MeOTAD/2D perovskite/3D perovskite/SnO_2/FTO. The time elapsed refers only to the time under illumination.

1230

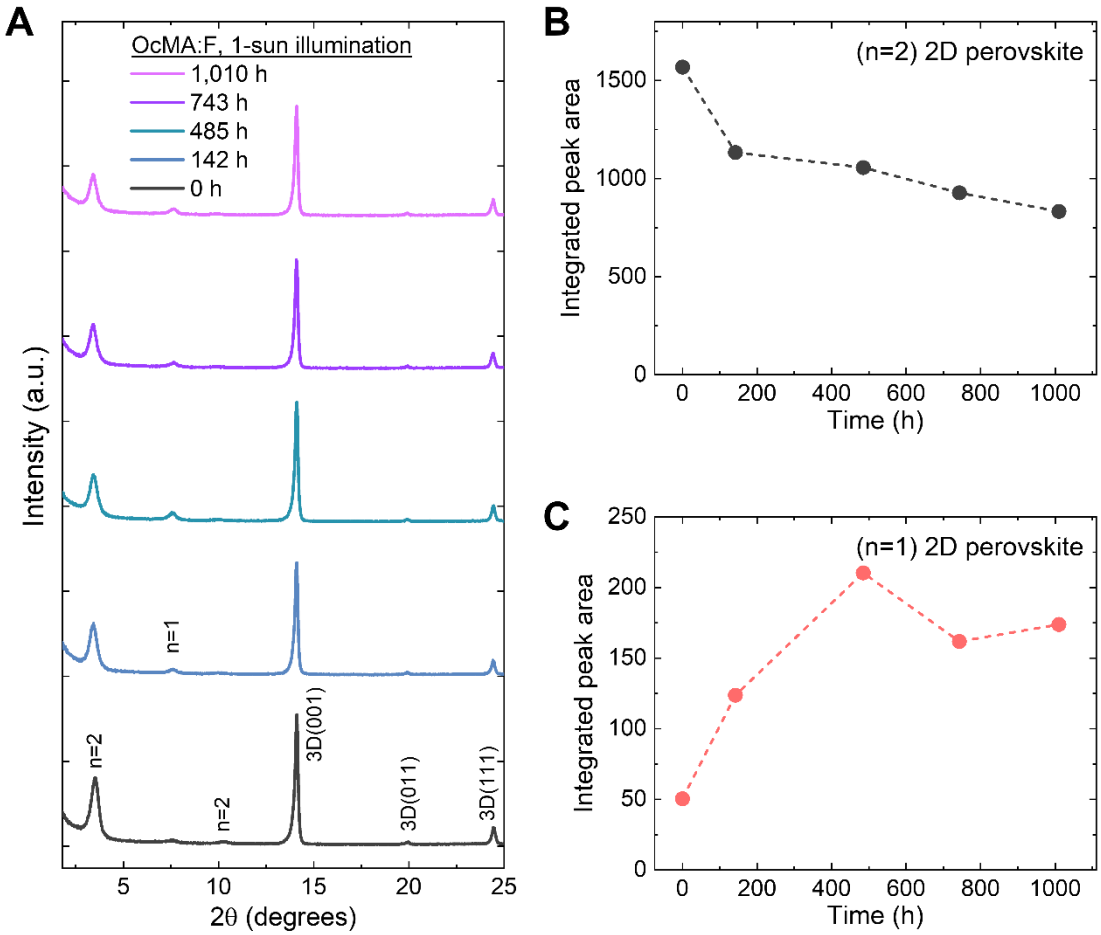

Fig. S35. (**A**) XRD patterns of the OcMA:F 2D/3D perovskite aged under 1-sun AM 1.5G illumination in a N_2 glovebox. The XRD was performed on devices of structure spiro-MeOTAD/2D perovskite/3D perovskite/SnO_2/FTO. Evolution of the (**B**) 2D(n=2) perovskite, and (**C**) 2D(n=1) perovskite integrated peak areas. The time elapsed refers only to the time under illumination.

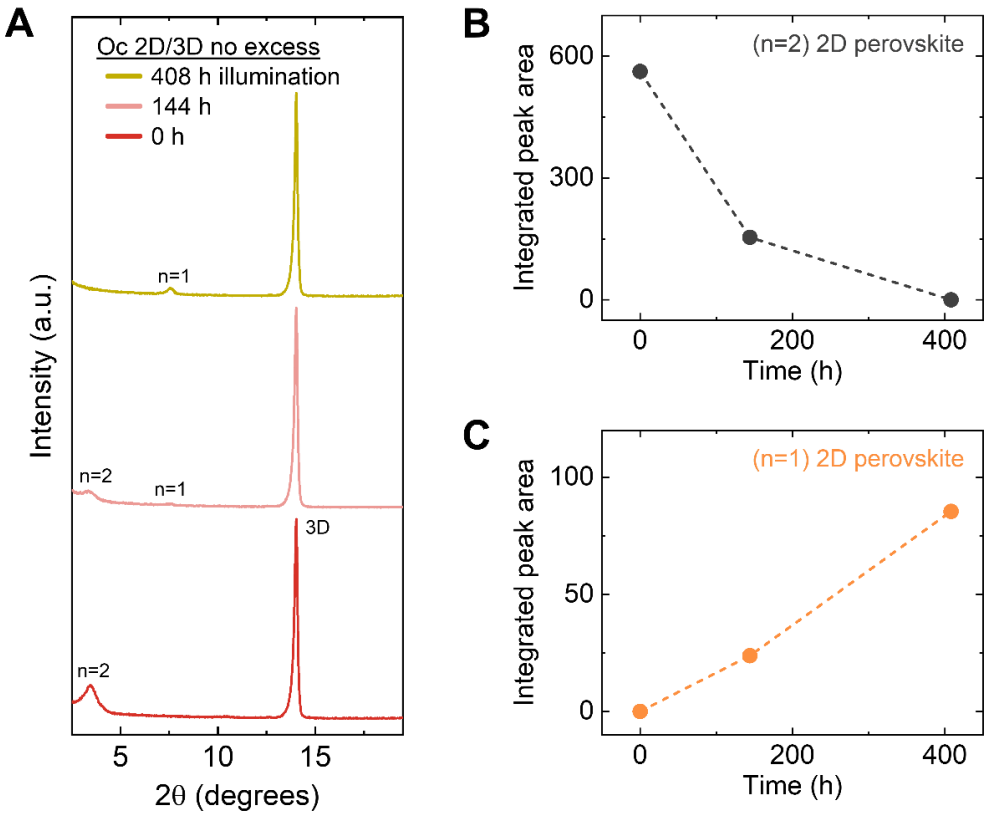

Fig. S36. (**A**) XRD patterns of the "Oc 2D/3D no excess" 2D/3D perovskite aged under 1-sun AM 1.5G illumination in a N_2 glovebox. This uses the control Oc 2D perovskite, but applied to our 3D perovskite composition but with no excess/residual PbI_2 at all. The XRD was performed on devices of structure spiro-MeOTAD/2D perovskite/3D perovskite/SnO_2/FTO. Evolution of the (**B**) 2D(n=2) perovskite, and (**C**) 2D(n=1) perovskite integrated peak areas. The time elapsed refers only to the time under illumination.

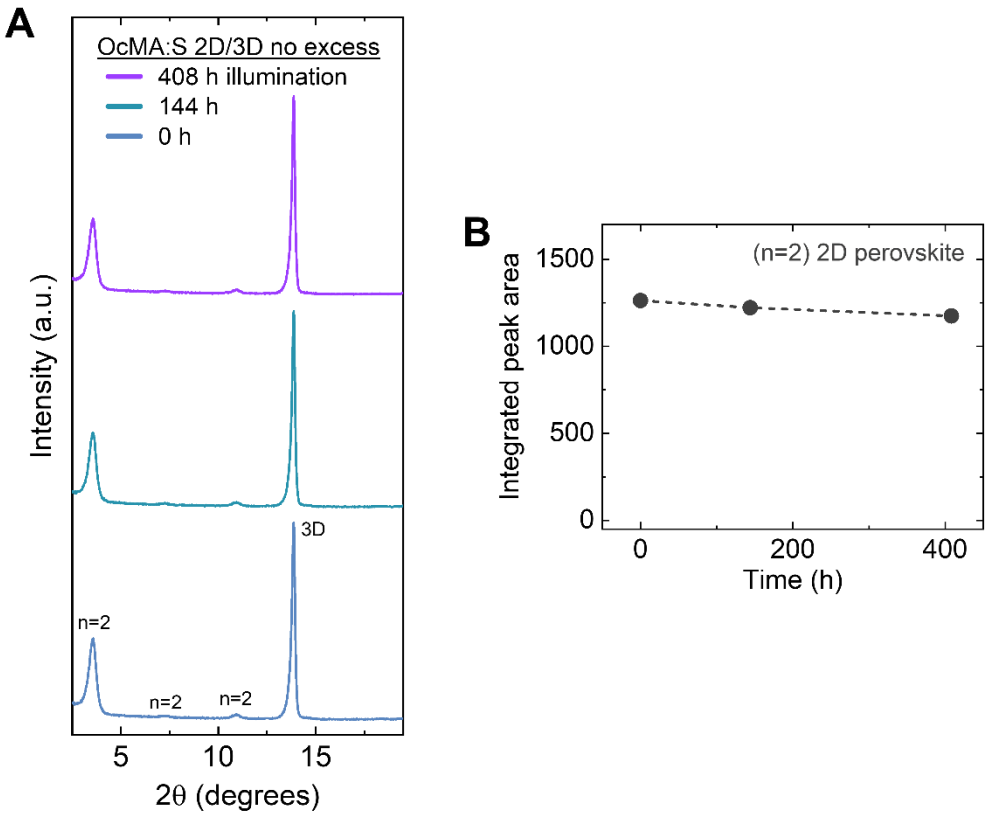

Fig. S37. (**A**) XRD patterns of the "OcMA:S 2D/3D no excess" 2D/3D perovskite aged under 1-sun AM 1.5G illumination in a N_2 glovebox. This uses the target OcMA:S 2D perovskite, but applied to our 3D perovskite composition but with no excess/residual PbI_2 at all. The XRD was performed on devices of structure spiro-MeOTAD/2D perovskite/3D perovskite/SnO_2/FTO. (**B**) Evolution of the 2D(n=2) perovskite integrated peak area. The time elapsed refers only to the time under illumination.

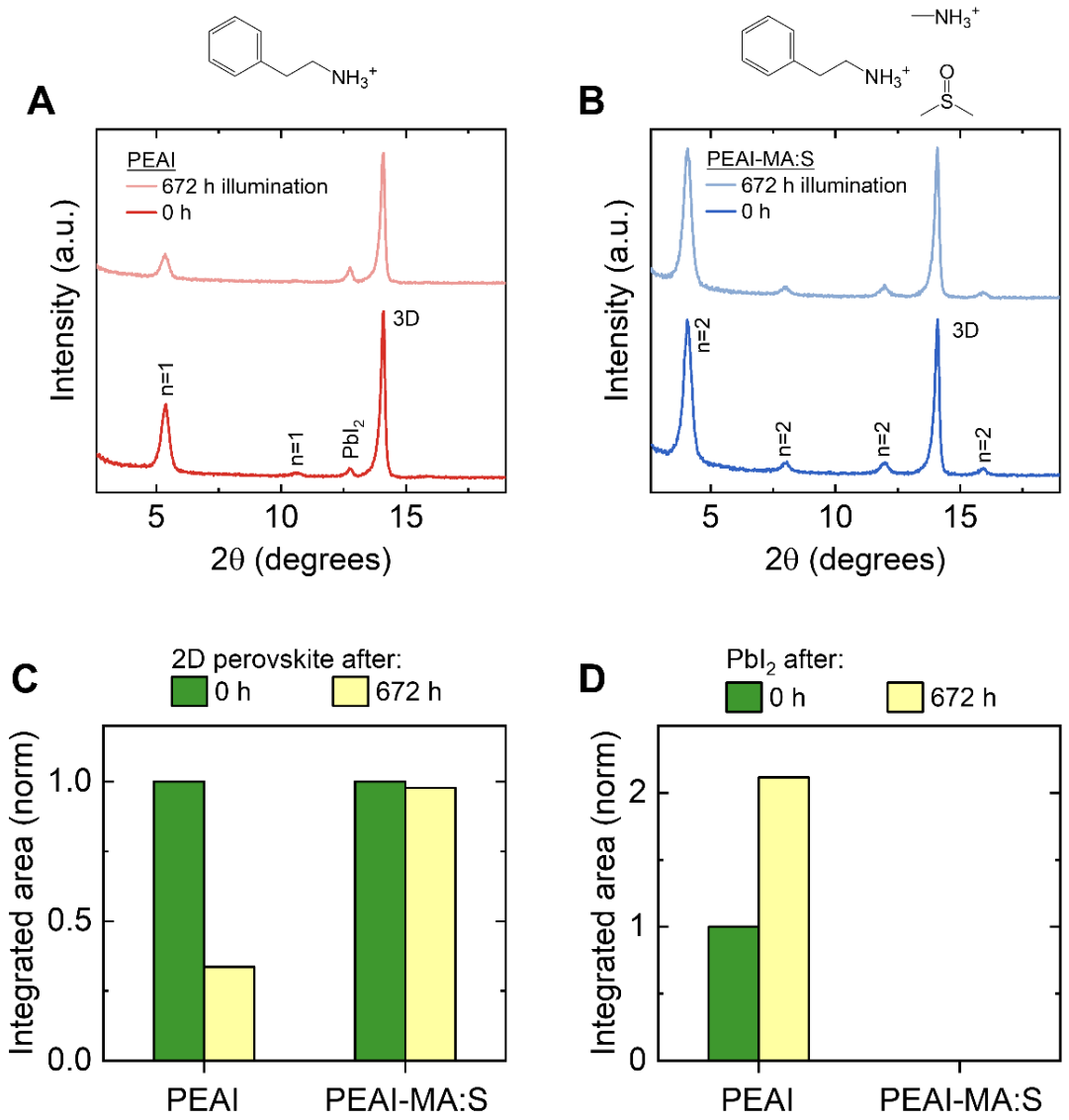

Fig. S38. XRD patterns of the 2D/3D perovskite with (**A**) PEAI, and (**B**) PEAI-MA:S aged under 1-sun AM 1.5G illumination in a N_2 glovebox. Evolution of the (**C**) 2D perovskite, and (**D**) PbI_2 integrated peak areas. For the PEAI-MA:S system, the PEAI:MAI:S ratio was 1:0.6:2.5. The time elapsed refers only to the time under illumination.

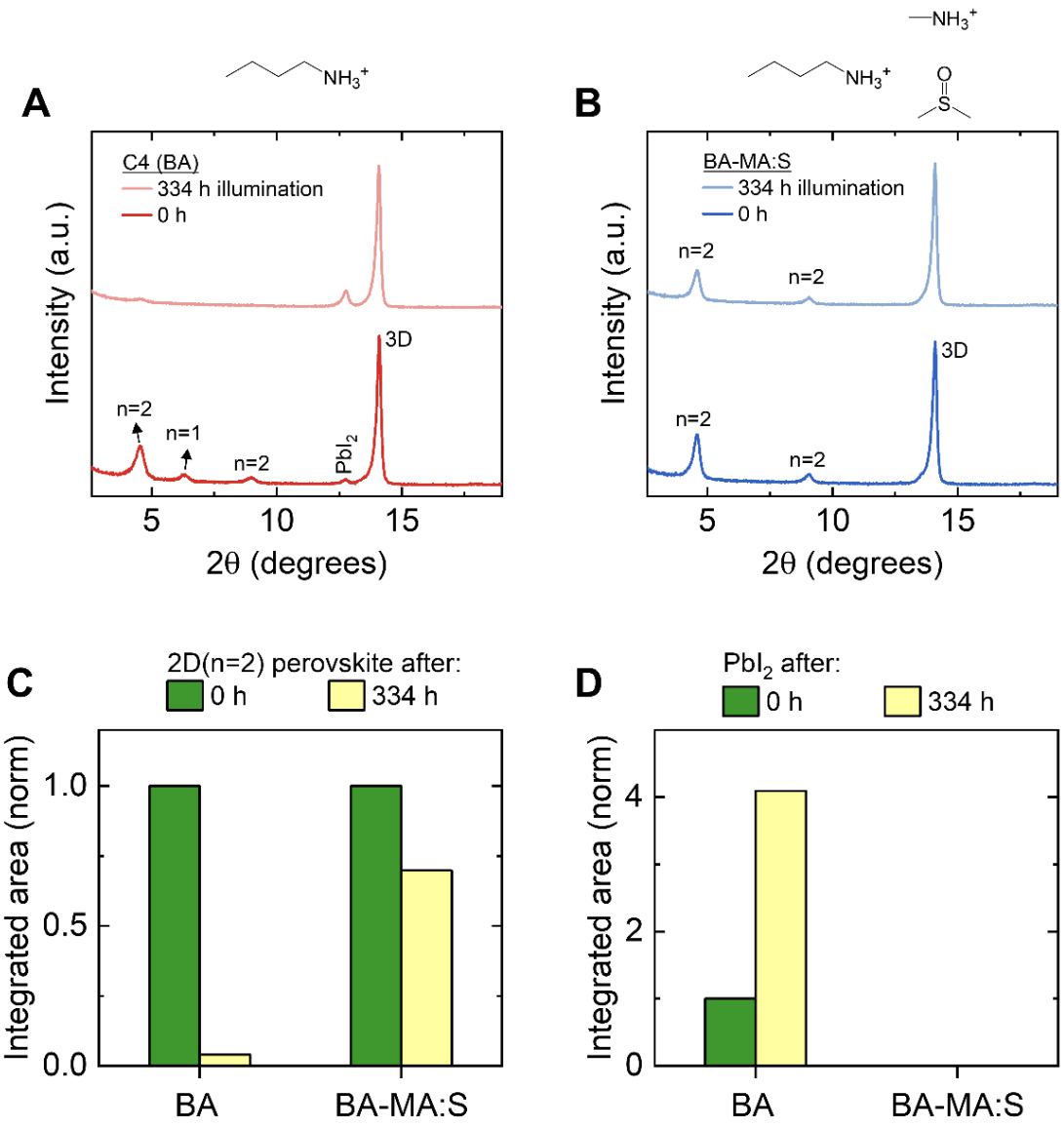

Fig. S39. XRD patterns of the 2D/3D perovskite with (**A**) BA, and (**B**) BA-MA:S aged under 1-sun AM 1.5G illumination in a N_2 glovebox. Evolution of the (**C**) 2D(n=2) perovskite, and (**D**) PbI_2 integrated peak areas. The time elapsed refers only to the time under illumination.

1270 **Table S1.** List of naming abbreviations.

Label	Ligand	A cation	Solvent
Oc	10 mM n-octylammonium bromide	-	isopropanol
Oc:S	10 mM n-octylammonium bromide	-	25 mM dimethylsulfoxide in isopropanol
OcMA	10 mM n-octylammonium bromide	3 mM methylammonium iodide	isopropanol
OcMA-Br	10 mM n-octylammonium bromide	3 mM methylammonium bromide	isopropanol
OcMA-Cl	10 mM n-octylammonium bromide	3 mM methylammonium chloride	isopropanol
OcMA:PC	10 mM n-octylammonium bromide	3 mM methylammonium iodide	25 mM propylene carbonate in isopropanol
OcMA:A	10 mM n-octylammonium bromide	3 mM methylammonium iodide	25 mM acetonitrile in isopropanol
OcMA:MG	10 mM n-octylammonium bromide	3 mM methylammonium iodide	25 mM methyl glycol in isopropanol
OcMA:F	10 mM n-octylammonium bromide	3 mM methylammonium iodide	25 mM dimethylformamide in isopropanol
OcMA:N	10 mM n-octylammonium bromide	3 mM methylammonium iodide	25 mM 1-methyl-2-pyrrolidone in isopropanol
OcMA:S	10 mM n-octylammonium bromide	3 mM methylammonium iodide	25 mM dimethylsulfoxide in isopropanol
PEAI	10 mM Phenethylammonium iodide	-	isopropanol
PEAI-MA:S	10 mM Phenethylammonium iodide	6 mM methylammonium iodide	25 mM dimethylsulfoxide in isopropanol
BA	10 mM		isopropanol

	n-butylammonium bromide		
BA-MA:S	10 mM n-butylammonium bromide	3 mM methylammonium iodide	25 mM dimethylsulfoxide in isopropanol

Table S2. Crystal data of the DFT slab models of the 3D perovskite and acetonitrile (A).

```
#======================================================================
# CRYSTAL DATA
#----------------------------------------------------------------------
data_VESTA_phase_1

_chemical_name_common                  'POSCAR pvsk A                '
_cell_length_a                         12.722600
_cell_length_b                         12.722600
_cell_length_c                         38.167801
_cell_angle_alpha                      90.000000
_cell_angle_beta                       90.000000
_cell_angle_gamma                      90.000000
_cell_volume                           6178.013930
_space_group_name_H-M_alt              'P 1'
_space_group_IT_number                 1

loop_
_space_group_symop_operation_xyz
   'x, y, z'

loop_
   _atom_site_label
   _atom_site_occupancy
   _atom_site_fract_x
   _atom_site_fract_y
   _atom_site_fract_z
   _atom_site_adp_type
   _atom_site_U_iso_or_equiv
   _atom_site_type_symbol
   C1        1.0     0.240031    0.274001    0.083436    Uiso  ? C
   C2        1.0     0.257256    0.285560    0.417546    Uiso  ? C
   C3        1.0     0.251068    0.786639    0.082635    Uiso  ? C
   C4        1.0     0.263751    0.775624    0.416863    Uiso  ? C
   C5        1.0     0.753495    0.277803    0.088240    Uiso  ? C
   C6        1.0     0.753268    0.286391    0.419315    Uiso  ? C
   C7        1.0     0.753155    0.779507    0.089313    Uiso  ? C
   C8        1.0     0.748879    0.754356    0.404412    Uiso  ? C
   C9        1.0     0.243879    0.290487    0.250640    Uiso  ? C
   C10       1.0     0.246796    0.770035    0.256412    Uiso  ? C
   C11       1.0     0.755475    0.243169    0.264018    Uiso  ? C
   C12       1.0     0.742805    0.778643    0.254074    Uiso  ? C
   C13       1.0     0.230495    0.763092    0.570325    Uiso  ? C
   C14       1.0     0.332678    0.786230    0.584939    Uiso  ? C

   N1        1.0     0.323404    0.233735    0.098283    Uiso  ? N
   N2        1.0     0.343267    0.232331    0.423557    Uiso  ? N
   N3        1.0     0.341713    0.739006    0.079641    Uiso  ? N
```

N4	1.0	0.284168	0.718383	0.444351	Uiso	? N
N5	1.0	0.803984	0.261024	0.059028	Uiso	? N
N6	1.0	0.747001	0.239330	0.388888	Uiso	? N
N7	1.0	0.810240	0.777188	0.060919	Uiso	? N
N8	1.0	0.839305	0.761832	0.420473	Uiso	? N
N9	1.0	0.196799	0.236282	0.055132	Uiso	? N
N10	1.0	0.163869	0.243795	0.414483	Uiso	? N
N11	1.0	0.160115	0.740368	0.078908	Uiso	? N
N12	1.0	0.188890	0.755398	0.394308	Uiso	? N
N13	1.0	0.676220	0.219194	0.099633	Uiso	? N
N14	1.0	0.755575	0.239008	0.449602	Uiso	? N
N15	1.0	0.678917	0.711786	0.096388	Uiso	? N
N16	1.0	0.663592	0.715805	0.418359	Uiso	? N
N17	1.0	0.153950	0.261406	0.237259	Uiso	? N
N18	1.0	0.326382	0.705156	0.255782	Uiso	? N
N19	1.0	0.843222	0.248519	0.246294	Uiso	? N
N20	1.0	0.787414	0.760548	0.223883	Uiso	? N
N21	1.0	0.315689	0.225483	0.261943	Uiso	? N
N22	1.0	0.168234	0.766611	0.234417	Uiso	? N
N23	1.0	0.663189	0.223988	0.250577	Uiso	? N
N24	1.0	0.690524	0.708310	0.271960	Uiso	? N
N25	1.0	0.415388	0.805568	0.596158	Uiso	? N
H1	1.0	0.204357	0.342781	0.095400	Uiso	? H
H2	1.0	0.263910	0.370203	0.414634	Uiso	? H
H3	1.0	0.251393	0.869794	0.089049	Uiso	? H
H4	1.0	0.311782	0.845013	0.412235	Uiso	? H
H5	1.0	0.777569	0.344121	0.104302	Uiso	? H
H6	1.0	0.756395	0.371830	0.419415	Uiso	? H
H7	1.0	0.768399	0.841504	0.108248	Uiso	? H
H8	1.0	0.744766	0.782440	0.377542	Uiso	? H
H9	1.0	0.353651	0.265361	0.120543	Uiso	? H
H10	1.0	0.412049	0.271910	0.426459	Uiso	? H
H11	1.0	0.408639	0.782406	0.080476	Uiso	? H
H12	1.0	0.343155	0.739833	0.461229	Uiso	? H
H13	1.0	0.862273	0.310660	0.051659	Uiso	? H
H14	1.0	0.745345	0.284545	0.366927	Uiso	? H
H15	1.0	0.865003	0.834018	0.056951	Uiso	? H
H16	1.0	0.900379	0.796730	0.407981	Uiso	? H
H17	1.0	0.361929	0.170785	0.087953	Uiso	? H
H18	1.0	0.342193	0.153798	0.428804	Uiso	? H
H19	1.0	0.347096	0.663043	0.071445	Uiso	? H
H20	1.0	0.240511	0.654604	0.451155	Uiso	? H
H21	1.0	0.785544	0.200397	0.042458	Uiso	? H
H22	1.0	0.742100	0.159950	0.386271	Uiso	? H
H23	1.0	0.799108	0.722498	0.041701	Uiso	? H
H24	1.0	0.850699	0.740607	0.445944	Uiso	? H
H25	1.0	0.227053	0.172702	0.042120	Uiso	? H
H26	1.0	0.149895	0.165491	0.417303	Uiso	? H
H27	1.0	0.153461	0.663262	0.072201	Uiso	? H
H28	1.0	0.141142	0.691431	0.396902	Uiso	? H
H29	1.0	0.648564	0.156537	0.085877	Uiso	? H
H30	1.0	0.752595	0.159406	0.452528	Uiso	? H
H31	1.0	0.659607	0.652643	0.079652	Uiso	? H
H32	1.0	0.660595	0.688711	0.443460	Uiso	? H
H33	1.0	0.133962	0.272623	0.043912	Uiso	? H
H34	1.0	0.101205	0.292062	0.410808	Uiso	? H
H35	1.0	0.093403	0.783122	0.081855	Uiso	? H
H36	1.0	0.179334	0.802892	0.373157	Uiso	? H
H37	1.0	0.639079	0.237145	0.122486	Uiso	? H

H38	1.0	0.761349	0.283410	0.471662	Uiso ? H	
H39	1.0	0.636571	0.718562	0.118963	Uiso ? H	
H40	1.0	0.596751	0.713320	0.403839	Uiso ? H	
H41	1.0	0.260126	0.374112	0.252249	Uiso ? H	
H42	1.0	0.245633	0.830480	0.276545	Uiso ? H	
H43	1.0	0.760231	0.255552	0.292149	Uiso ? H	
H44	1.0	0.750049	0.856907	0.265242	Uiso ? H	
H45	1.0	0.102982	0.317323	0.228797	Uiso ? H	
H46	1.0	0.384515	0.711657	0.273876	Uiso ? H	
H47	1.0	0.910553	0.261674	0.259992	Uiso ? H	
H48	1.0	0.822840	0.820219	0.210788	Uiso ? H	
H49	1.0	0.131593	0.184588	0.235368	Uiso ? H	
H50	1.0	0.331539	0.645915	0.237952	Uiso ? H	
H51	1.0	0.848010	0.237337	0.219908	Uiso ? H	
H52	1.0	0.782015	0.689853	0.211418	Uiso ? H	
H53	1.0	0.307585	0.145953	0.261106	Uiso ? H	
H54	1.0	0.164870	0.713057	0.214628	Uiso ? H	
H55	1.0	0.650736	0.212592	0.224489	Uiso ? H	
H56	1.0	0.677451	0.634207	0.262863	Uiso ? H	
H57	1.0	0.381638	0.253814	0.273681	Uiso ? H	
H58	1.0	0.110047	0.821352	0.236224	Uiso ? H	
H59	1.0	0.599881	0.223354	0.266848	Uiso ? H	
H60	1.0	0.655917	0.728069	0.295064	Uiso ? H	
H61	1.0	0.208279	0.823970	0.551549	Uiso ? H	
H62	1.0	0.170710	0.759043	0.590734	Uiso ? H	
H63	1.0	0.232354	0.688032	0.556329	Uiso ? H	
Pb1	1.0	0.998489	0.506409	0.001961	Uiso ? Pb	
Pb2	1.0	0.987922	0.506813	0.330398	Uiso ? Pb	
Pb3	1.0	0.513284	0.982534	0.007423	Uiso ? Pb	
Pb4	1.0	0.492682	0.997597	0.337417	Uiso ? Pb	
Pb5	1.0	0.003360	0.009530	0.163652	Uiso ? Pb	
Pb6	1.0	0.998109	0.003821	0.492608	Uiso ? Pb	
Pb7	1.0	0.495686	0.500418	0.172688	Uiso ? Pb	
Pb8	1.0	0.496740	0.486299	0.500698	Uiso ? Pb	
Pb9	1.0	0.011263	0.001191	0.999569	Uiso ? Pb	
Pb10	1.0	0.992842	0.007745	0.330553	Uiso ? Pb	
Pb11	1.0	0.496747	0.481185	0.010278	Uiso ? Pb	
Pb12	1.0	0.483834	0.492266	0.337612	Uiso ? Pb	
Pb13	1.0	0.992523	0.508756	0.166248	Uiso ? Pb	
Pb14	1.0	0.999587	0.499394	0.494279	Uiso ? Pb	
Pb15	1.0	0.497865	0.992508	0.173879	Uiso ? Pb	
Pb16	1.0	0.500915	0.995122	0.496915	Uiso ? Pb	
I1	1.0	0.258330	0.518945	0.016844	Uiso ? I	
I2	1.0	0.244505	0.488790	0.329768	Uiso ? I	
I3	1.0	0.758639	0.519270	0.009561	Uiso ? I	
I4	1.0	0.745068	0.494181	0.340503	Uiso ? I	
I5	1.0	0.000965	0.265514	0.988280	Uiso ? I	
I6	1.0	0.994529	0.255338	0.327019	Uiso ? I	
I7	1.0	0.001894	0.762539	0.991476	Uiso ? I	
I8	1.0	0.979834	0.756248	0.328898	Uiso ? I	
I9	1.0	0.490603	0.244115	0.012733	Uiso ? I	
I10	1.0	0.507522	0.242946	0.332168	Uiso ? I	
I11	1.0	0.533789	0.746372	0.007076	Uiso ? I	
I12	1.0	0.486437	0.743223	0.341183	Uiso ? I	
I13	1.0	0.998387	0.483797	0.081518	Uiso ? I	
I14	1.0	0.032840	0.501139	0.415138	Uiso ? I	
I15	1.0	0.998164	0.996897	0.079338	Uiso ? I	
I16	1.0	0.972050	0.024102	0.413588	Uiso ? I	

I17	1.0	0.510408	0.485082	0.089787	Uiso	? I
I18	1.0	0.489727	0.479260	0.421204	Uiso	? I
I19	1.0	0.502183	0.984153	0.087727	Uiso	? I
I20	1.0	0.546493	0.009515	0.418527	Uiso	? I
I21	1.0	0.247294	0.524053	0.174046	Uiso	? I
I22	1.0	0.256556	0.483141	0.503770	Uiso	? I
I23	1.0	0.747065	0.488918	0.174696	Uiso	? I
I24	1.0	0.758885	0.514927	0.485846	Uiso	? I
I25	1.0	0.992612	0.254828	0.159475	Uiso	? I
I26	1.0	0.998671	0.249399	0.502372	Uiso	? I
I27	1.0	0.981793	0.754237	0.157479	Uiso	? I
I28	1.0	0.026022	0.748750	0.492418	Uiso	? I
I29	1.0	0.488126	0.247056	0.175110	Uiso	? I
I30	1.0	0.522397	0.243647	0.507438	Uiso	? I
I31	1.0	0.520050	0.745978	0.175836	Uiso	? I
I32	1.0	0.507007	0.745258	0.499807	Uiso	? I
I33	1.0	0.996652	0.512599	0.248204	Uiso	? I
I34	1.0	0.009280	0.001858	0.247195	Uiso	? I
I35	1.0	0.506531	0.483880	0.255503	Uiso	? I
I36	1.0	0.474230	0.979580	0.254925	Uiso	? I
I37	1.0	0.254789	0.990675	0.006907	Uiso	? I
I38	1.0	0.754132	0.025509	0.004917	Uiso	? I
I39	1.0	0.243943	0.999484	0.342093	Uiso	? I
I40	1.0	0.744034	0.999326	0.327284	Uiso	? I
I41	1.0	0.246829	0.999352	0.166232	Uiso	? I
I42	1.0	0.745978	0.019475	0.175043	Uiso	? I
I43	1.0	0.261635	0.006127	0.479418	Uiso	? I
I44	1.0	0.760857	0.976790	0.499199	Uiso	? I

Table S3. Crystal data of the DFT slab models of the 3D perovskite and dimethylformamide (F).

```
#======================================================================
# CRYSTAL DATA
#----------------------------------------------------------------------
data_VESTA_phase_1

_chemical_name_common                  'POSCAR pvsk F                '
_cell_length_a                         12.722600
_cell_length_b                         12.722600
_cell_length_c                         38.167801
_cell_angle_alpha                      90.000000
_cell_angle_beta                       90.000000
_cell_angle_gamma                      90.000000
_cell_volume                           6178.013930
_space_group_name_H-M_alt              'P 1'
_space_group_IT_number                 1

loop_
_space_group_symop_operation_xyz
   'x, y, z'

loop_
   _atom_site_label
   _atom_site_occupancy
   _atom_site_fract_x
   _atom_site_fract_y
   _atom_site_fract_z
```

_atom_site_adp_type _atom_site_U_iso_or_equiv _atom_site_type_symbol						
C1	1.0	0.242143	0.273739	0.084097	Uiso	? C
C2	1.0	0.256359	0.290817	0.417106	Uiso	? C
C3	1.0	0.250136	0.787372	0.083796	Uiso	? C
C4	1.0	0.257448	0.772747	0.417115	Uiso	? C
C5	1.0	0.753833	0.278632	0.088943	Uiso	? C
C6	1.0	0.754067	0.292194	0.418459	Uiso	? C
C7	1.0	0.751955	0.778374	0.089126	Uiso	? C
C8	1.0	0.755600	0.759279	0.403612	Uiso	? C
C9	1.0	0.241159	0.293828	0.253491	Uiso	? C
C10	1.0	0.243484	0.769173	0.256717	Uiso	? C
C11	1.0	0.755485	0.244149	0.264051	Uiso	? C
C12	1.0	0.739140	0.776959	0.253426	Uiso	? C
C13	1.0	0.710304	0.621327	0.565524	Uiso	? C
N1	1.0	0.321167	0.227028	0.099467	Uiso	? N
N2	1.0	0.344974	0.241250	0.422178	Uiso	? N
N3	1.0	0.340844	0.739964	0.080900	Uiso	? N
N4	1.0	0.274778	0.713011	0.444241	Uiso	? N
N5	1.0	0.802558	0.259457	0.059574	Uiso	? N
N6	1.0	0.752959	0.244620	0.388084	Uiso	? N
N7	1.0	0.802773	0.777338	0.059422	Uiso	? N
N8	1.0	0.845236	0.758670	0.420346	Uiso	? N
N9	1.0	0.201446	0.243002	0.054478	Uiso	? N
N10	1.0	0.164853	0.244767	0.414140	Uiso	? N
N11	1.0	0.159305	0.742053	0.078484	Uiso	? N
N12	1.0	0.191533	0.750099	0.391855	Uiso	? N
N13	1.0	0.677547	0.220913	0.101525	Uiso	? N
N14	1.0	0.756321	0.245113	0.448847	Uiso	? N
N15	1.0	0.684551	0.706276	0.098675	Uiso	? N
N16	1.0	0.667535	0.722937	0.416276	Uiso	? N
N17	1.0	0.160545	0.266134	0.234431	Uiso	? N
N18	1.0	0.321482	0.703101	0.260045	Uiso	? N
N19	1.0	0.843353	0.250376	0.246487	Uiso	? N
N20	1.0	0.780931	0.753389	0.223226	Uiso	? N
N21	1.0	0.310937	0.228441	0.265884	Uiso	? N
N22	1.0	0.172206	0.763740	0.232201	Uiso	? N
N23	1.0	0.663129	0.226994	0.250335	Uiso	? N
N24	1.0	0.689680	0.709796	0.273409	Uiso	? N
N25	1.0	0.728387	0.716897	0.553473	Uiso	? N
H1	1.0	0.207980	0.342116	0.096764	Uiso	? H
H2	1.0	0.259048	0.376034	0.414880	Uiso	? H
H3	1.0	0.249983	0.869370	0.091655	Uiso	? H
H4	1.0	0.299426	0.846887	0.415411	Uiso	? H
H5	1.0	0.778315	0.346748	0.104077	Uiso	? H
H6	1.0	0.753154	0.377826	0.418453	Uiso	? H
H7	1.0	0.766833	0.843058	0.107058	Uiso	? H
H8	1.0	0.754456	0.792871	0.377420	Uiso	? H
H9	1.0	0.349779	0.253860	0.122629	Uiso	? H
H10	1.0	0.411637	0.284250	0.425282	Uiso	? H
H11	1.0	0.407828	0.782373	0.083795	Uiso	? H
H12	1.0	0.327453	0.736297	0.462849	Uiso	? H
H13	1.0	0.860056	0.308874	0.051326	Uiso	? H
H14	1.0	0.750896	0.289788	0.366119	Uiso	? H
H15	1.0	0.852913	0.836984	0.053688	Uiso	? H
H16	1.0	0.909101	0.791075	0.408764	Uiso	? H

H17	1.0	0.357975	0.163895	0.088672	Uiso	? H
H18	1.0	0.347741	0.162358	0.426313	Uiso	? H
H19	1.0	0.347262	0.664667	0.072231	Uiso	? H
H20	1.0	0.239278	0.642174	0.447959	Uiso	? H
H21	1.0	0.783115	0.197963	0.043527	Uiso	? H
H22	1.0	0.751826	0.165184	0.385468	Uiso	? H
H23	1.0	0.790927	0.720578	0.040926	Uiso	? H
H24	1.0	0.853710	0.731519	0.445274	Uiso	? H
H25	1.0	0.229729	0.179331	0.041067	Uiso	? H
H26	1.0	0.155841	0.165687	0.416576	Uiso	? H
H27	1.0	0.153192	0.666160	0.070311	Uiso	? H
H28	1.0	0.149612	0.681854	0.391665	Uiso	? H
H29	1.0	0.648543	0.157242	0.088587	Uiso	? H
H30	1.0	0.758039	0.165553	0.451630	Uiso	? H
H31	1.0	0.665405	0.644542	0.082978	Uiso	? H
H32	1.0	0.662976	0.688874	0.440355	Uiso	? H
H33	1.0	0.140811	0.283080	0.043361	Uiso	? H
H34	1.0	0.099722	0.289607	0.410597	Uiso	? H
H35	1.0	0.092511	0.784804	0.081125	Uiso	? H
H36	1.0	0.183596	0.800568	0.371375	Uiso	? H
H37	1.0	0.641562	0.241305	0.124317	Uiso	? H
H38	1.0	0.757509	0.289366	0.470988	Uiso	? H
H39	1.0	0.645493	0.713149	0.121841	Uiso	? H
H40	1.0	0.601222	0.725977	0.401398	Uiso	? H
H41	1.0	0.250696	0.376785	0.259441	Uiso	? H
H42	1.0	0.237499	0.832844	0.275602	Uiso	? H
H43	1.0	0.759935	0.254240	0.292238	Uiso	? H
H44	1.0	0.746413	0.857345	0.262728	Uiso	? H
H45	1.0	0.110116	0.322090	0.225678	Uiso	? H
H46	1.0	0.374146	0.712085	0.279829	Uiso	? H
H47	1.0	0.910716	0.263475	0.260193	Uiso	? H
H48	1.0	0.813929	0.810950	0.208472	Uiso	? H
H49	1.0	0.143907	0.189699	0.228720	Uiso	? H
H50	1.0	0.331993	0.641181	0.243577	Uiso	? H
H51	1.0	0.848061	0.242529	0.219986	Uiso	? H
H52	1.0	0.775614	0.680356	0.212365	Uiso	? H
H53	1.0	0.309491	0.149783	0.260993	Uiso	? H
H54	1.0	0.173584	0.707159	0.213356	Uiso	? H
H55	1.0	0.651046	0.217852	0.224159	Uiso	? H
H56	1.0	0.675874	0.634106	0.266052	Uiso	? H
H57	1.0	0.370166	0.255245	0.281472	Uiso	? H
H58	1.0	0.114478	0.819012	0.231486	Uiso	? H
H59	1.0	0.599459	0.225706	0.266415	Uiso	? H
H60	1.0	0.657212	0.733841	0.296387	Uiso	? H
H61	1.0	0.774237	0.587105	0.580871	Uiso	? H
H62	1.0	0.675174	0.752586	0.537407	Uiso	? H
H63	1.0	0.800612	0.749578	0.555385	Uiso	? H

Pb1	1.0	0.997785	0.508761	0.002038	Uiso	? Pb
Pb2	1.0	0.996824	0.509618	0.330187	Uiso	? Pb
Pb3	1.0	0.512579	0.986027	0.009403	Uiso	? Pb
Pb4	1.0	0.495622	0.003148	0.338112	Uiso	? Pb
Pb5	1.0	0.000655	0.009052	0.165112	Uiso	? Pb
Pb6	1.0	0.020582	0.010479	0.491110	Uiso	? Pb
Pb7	1.0	0.494156	0.498668	0.174971	Uiso	? Pb
Pb8	1.0	0.537579	0.517474	0.507134	Uiso	? Pb
Pb9	1.0	0.011002	0.004093	0.001338	Uiso	? Pb
Pb10	1.0	0.997259	0.010604	0.331219	Uiso	? Pb
Pb11	1.0	0.496696	0.485633	0.011581	Uiso	? Pb
Pb12	1.0	0.494088	0.497692	0.341795	Uiso	? Pb

Pb13	1.0	0.992219	0.510084	0.165701	Uiso	? Pb
Pb14	1.0	0.029171	0.500952	0.495898	Uiso	? Pb
Pb15	1.0	0.495785	0.991444	0.175700	Uiso	? Pb
Pb16	1.0	0.523952	0.022752	0.497775	Uiso	? Pb
I1	1.0	0.255760	0.523998	0.014663	Uiso	? I
I2	1.0	0.248207	0.494252	0.331851	Uiso	? I
I3	1.0	0.756301	0.518261	0.010124	Uiso	? I
I4	1.0	0.748943	0.498761	0.340884	Uiso	? I
I5	1.0	0.000792	0.268211	0.988256	Uiso	? I
I6	1.0	0.997370	0.258614	0.327075	Uiso	? I
I7	1.0	0.001849	0.765484	0.991675	Uiso	? I
I8	1.0	0.982450	0.759595	0.328747	Uiso	? I
I9	1.0	0.492523	0.245471	0.014225	Uiso	? I
I10	1.0	0.511786	0.248164	0.333164	Uiso	? I
I11	1.0	0.532847	0.747558	0.008239	Uiso	? I
I12	1.0	0.484905	0.750168	0.343014	Uiso	? I
I13	1.0	0.001012	0.481041	0.081572	Uiso	? I
I14	1.0	0.033555	0.505302	0.415965	Uiso	? I
I15	1.0	0.989817	0.997386	0.080865	Uiso	? I
I16	1.0	0.953736	0.030196	0.414620	Uiso	? I
I17	1.0	0.505188	0.486830	0.090839	Uiso	? I
I18	1.0	0.485565	0.487967	0.422031	Uiso	? I
I19	1.0	0.511719	0.982282	0.089841	Uiso	? I
I20	1.0	0.560161	0.026177	0.419161	Uiso	? I
I21	1.0	0.245482	0.520745	0.173598	Uiso	? I
I22	1.0	0.262929	0.486774	0.502899	Uiso	? I
I23	1.0	0.745817	0.486195	0.173835	Uiso	? I
I24	1.0	0.763703	0.521628	0.479300	Uiso	? I
I25	1.0	0.990602	0.253370	0.159937	Uiso	? I
I26	1.0	0.998566	0.255973	0.503626	Uiso	? I
I27	1.0	0.979271	0.753866	0.157340	Uiso	? I
I28	1.0	0.011192	0.757205	0.499793	Uiso	? I
I29	1.0	0.484301	0.245399	0.176436	Uiso	? I
I30	1.0	0.526551	0.261288	0.509914	Uiso	? I
I31	1.0	0.513042	0.745126	0.176642	Uiso	? I
I32	1.0	0.502485	0.762365	0.495840	Uiso	? I
I33	1.0	0.997815	0.513902	0.248394	Uiso	? I
I34	1.0	0.026529	0.005031	0.248216	Uiso	? I
I35	1.0	0.506069	0.486662	0.256189	Uiso	? I
I36	1.0	0.460125	0.981252	0.256759	Uiso	? I
I37	1.0	0.256266	0.990313	0.011139	Uiso	? I
I38	1.0	0.755202	0.026096	0.003529	Uiso	? I
I39	1.0	0.246150	0.007820	0.348610	Uiso	? I
I40	1.0	0.746444	0.001402	0.324977	Uiso	? I
I41	1.0	0.245915	0.995616	0.163339	Uiso	? I
I42	1.0	0.745477	0.015931	0.179595	Uiso	? I
I43	1.0	0.258633	0.011475	0.474643	Uiso	? I
I44	1.0	0.760309	0.992321	0.509452	Uiso	? I
O1	1.0	0.627735	0.570699	0.560887	Uiso	? O

1275

Table S4. Crystal data of the DFT slab models of the 3D perovskite and propylene carbonate (PC).

```
#======================================================================
# CRYSTAL DATA
#----------------------------------------------------------------------
```

```
data_VESTA_phase_1
_chemical_name_common                  'POSCAR pvsk PC                        '
_cell_length_a                         12.722600
_cell_length_b                         12.722600
_cell_length_c                         38.167801
_cell_angle_alpha                      90.000000
_cell_angle_beta                       90.000000
_cell_angle_gamma                      90.000000
_cell_volume                           6178.013930
_space_group_name_H-M_alt              'P 1'
_space_group_IT_number                 1

loop_
_space_group_symop_operation_xyz
   'x, y, z'

loop_
   _atom_site_label
   _atom_site_occupancy
   _atom_site_fract_x
   _atom_site_fract_y
   _atom_site_fract_z
   _atom_site_adp_type
   _atom_site_U_iso_or_equiv
   _atom_site_type_symbol
   C1     1.0   0.244592   0.273214   0.082917   Uiso  ? C
   C2     1.0   0.260727   0.289717   0.416359   Uiso  ? C
   C3     1.0   0.249282   0.790039   0.084068   Uiso  ? C
   C4     1.0   0.265593   0.767186   0.417566   Uiso  ? C
   C5     1.0   0.754930   0.279587   0.089751   Uiso  ? C
   C6     1.0   0.758842   0.298587   0.420246   Uiso  ? C
   C7     1.0   0.751556   0.778634   0.088896   Uiso  ? C
   C8     1.0   0.749879   0.750262   0.405945   Uiso  ? C
   C9     1.0   0.236511   0.289406   0.254740   Uiso  ? C
   C10    1.0   0.239306   0.768334   0.255456   Uiso  ? C
   C11    1.0   0.755743   0.239463   0.264197   Uiso  ? C
   C12    1.0   0.732445   0.773278   0.252370   Uiso  ? C
   C13    1.0   0.219341   0.380590   0.595711   Uiso  ? C
   C14    1.0   0.294169   0.287764   0.599649   Uiso  ? C
   C15    1.0   0.382306   0.433132   0.580219   Uiso  ? C
   C16    1.0   0.263226   0.190001   0.580196   Uiso  ? C

   N1     1.0   0.314440   0.215020   0.098930   Uiso  ? N
   N2     1.0   0.347036   0.238961   0.423782   Uiso  ? N
   N3     1.0   0.339292   0.742122   0.080127   Uiso  ? N
   N4     1.0   0.292596   0.704691   0.443065   Uiso  ? N
   N5     1.0   0.804314   0.261619   0.060425   Uiso  ? N
   N6     1.0   0.756191   0.247738   0.390443   Uiso  ? N
   N7     1.0   0.797148   0.778153   0.058279   Uiso  ? N
   N8     1.0   0.843307   0.758284   0.419876   Uiso  ? N
   N9     1.0   0.208555   0.253331   0.051651   Uiso  ? N
   N10    1.0   0.167223   0.246999   0.415798   Uiso  ? N
   N11    1.0   0.157999   0.747520   0.077106   Uiso  ? N
   N12    1.0   0.190719   0.747364   0.395009   Uiso  ? N
   N13    1.0   0.680261   0.219879   0.102358   Uiso  ? N
   N14    1.0   0.761651   0.255680   0.451266   Uiso  ? N
   N15    1.0   0.689868   0.703719   0.100237   Uiso  ? N
   N16    1.0   0.663966   0.729225   0.423260   Uiso  ? N
   N17    1.0   0.169265   0.270372   0.229666   Uiso  ? N
```

N18	1.0	0.316704	0.704802	0.263197	Uiso	?	N
N19	1.0	0.842825	0.249634	0.246334	Uiso	?	N
N20	1.0	0.770320	0.750076	0.221533	Uiso	?	N
N21	1.0	0.303065	0.220644	0.267055	Uiso	?	N
N22	1.0	0.175294	0.754961	0.229109	Uiso	?	N
N23	1.0	0.662198	0.227703	0.250692	Uiso	?	N
N24	1.0	0.690573	0.704880	0.273773	Uiso	?	N
H1	1.0	0.214654	0.342135	0.096488	Uiso	?	H
H2	1.0	0.266907	0.372305	0.409641	Uiso	?	H
H3	1.0	0.250011	0.869555	0.094365	Uiso	?	H
H4	1.0	0.307310	0.841169	0.414762	Uiso	?	H
H5	1.0	0.777186	0.348508	0.104836	Uiso	?	H
H6	1.0	0.758908	0.383855	0.419073	Uiso	?	H
H7	1.0	0.766084	0.845113	0.106061	Uiso	?	H
H8	1.0	0.743249	0.762121	0.377832	Uiso	?	H
H9	1.0	0.340287	0.234227	0.123289	Uiso	?	H
H10	1.0	0.415686	0.279639	0.425049	Uiso	?	H
H11	1.0	0.407008	0.782022	0.084709	Uiso	?	H
H12	1.0	0.349316	0.727032	0.460537	Uiso	?	H
H13	1.0	0.860522	0.312473	0.052196	Uiso	?	H
H14	1.0	0.753593	0.290396	0.367949	Uiso	?	H
H15	1.0	0.842019	0.840332	0.050978	Uiso	?	H
H16	1.0	0.905208	0.774988	0.404055	Uiso	?	H
H17	1.0	0.346711	0.150287	0.087541	Uiso	?	H
H18	1.0	0.345185	0.163387	0.432679	Uiso	?	H
H19	1.0	0.344495	0.669391	0.069179	Uiso	?	H
H20	1.0	0.255421	0.635440	0.448136	Uiso	?	H
H21	1.0	0.786485	0.199689	0.044356	Uiso	?	H
H22	1.0	0.755299	0.168041	0.388856	Uiso	?	H
H23	1.0	0.784712	0.719880	0.040350	Uiso	?	H
H24	1.0	0.857982	0.749262	0.445966	Uiso	?	H
H25	1.0	0.233525	0.189812	0.037457	Uiso	?	H
H26	1.0	0.154736	0.170199	0.421771	Uiso	?	H
H27	1.0	0.151747	0.674364	0.066594	Uiso	?	H
H28	1.0	0.147948	0.679811	0.395780	Uiso	?	H
H29	1.0	0.653433	0.154858	0.089624	Uiso	?	H
H30	1.0	0.760526	0.176725	0.455517	Uiso	?	H
H31	1.0	0.670931	0.640143	0.085337	Uiso	?	H
H32	1.0	0.662067	0.717136	0.449647	Uiso	?	H
H33	1.0	0.154683	0.301401	0.040283	Uiso	?	H
H34	1.0	0.103875	0.292833	0.410567	Uiso	?	H
H35	1.0	0.091738	0.790772	0.080296	Uiso	?	H
H36	1.0	0.176587	0.799175	0.375307	Uiso	?	H
H37	1.0	0.643596	0.239411	0.125087	Uiso	?	H
H38	1.0	0.761914	0.303682	0.472571	Uiso	?	H
H39	1.0	0.653344	0.710810	0.123855	Uiso	?	H
H40	1.0	0.594957	0.725010	0.409958	Uiso	?	H
H41	1.0	0.236901	0.367550	0.266233	Uiso	?	H
H42	1.0	0.227254	0.836696	0.272026	Uiso	?	H
H43	1.0	0.762067	0.240823	0.292547	Uiso	?	H
H44	1.0	0.736819	0.854618	0.261016	Uiso	?	H
H45	1.0	0.119735	0.328163	0.221683	Uiso	?	H
H46	1.0	0.364291	0.720862	0.283894	Uiso	?	H
H47	1.0	0.911288	0.257463	0.259918	Uiso	?	H
H48	1.0	0.797335	0.808820	0.205894	Uiso	?	H
H49	1.0	0.162453	0.198804	0.218063	Uiso	?	H
H50	1.0	0.333606	0.639115	0.249080	Uiso	?	H
H51	1.0	0.845757	0.248949	0.219689	Uiso	?	H
H52	1.0	0.767608	0.676052	0.211280	Uiso	?	H

H53	1.0	0.308278	0.145766	0.257847	Uiso ? H	
H54	1.0	0.182193	0.693487	0.212129	Uiso ? H	
H55	1.0	0.648349	0.226103	0.224440	Uiso ? H	
H56	1.0	0.680574	0.627933	0.267313	Uiso ? H	
H57	1.0	0.353653	0.241174	0.286625	Uiso ? H	
H58	1.0	0.116856	0.808114	0.225167	Uiso ? H	
H59	1.0	0.599437	0.222661	0.267140	Uiso ? H	
H60	1.0	0.660739	0.728771	0.297160	Uiso ? H	
H61	1.0	0.172775	0.396603	0.618981	Uiso ? H	
H62	1.0	0.169126	0.372825	0.572587	Uiso ? H	
H63	1.0	0.312232	0.271776	0.627128	Uiso ? H	
H64	1.0	0.322820	0.128967	0.583467	Uiso ? H	
H65	1.0	0.189140	0.160546	0.590772	Uiso ? H	
H66	1.0	0.252739	0.206796	0.552301	Uiso ? H	
Pb1	1.0	0.996200	0.510767	0.000865	Uiso ? Pb	
Pb2	1.0	0.994148	0.506092	0.328175	Uiso ? Pb	
Pb3	1.0	0.511779	0.987066	0.010204	Uiso ? Pb	
Pb4	1.0	0.491643	0.999059	0.339256	Uiso ? Pb	
Pb5	1.0	0.992712	0.008272	0.166111	Uiso ? Pb	
Pb6	1.0	0.001446	0.009536	0.491731	Uiso ? Pb	
Pb7	1.0	0.487332	0.494138	0.173676	Uiso ? Pb	
Pb8	1.0	0.500185	0.492849	0.504922	Uiso ? Pb	
Pb9	1.0	0.009769	0.006804	0.002413	Uiso ? Pb	
Pb10	1.0	0.994084	0.007869	0.330271	Uiso ? Pb	
Pb11	1.0	0.496398	0.486854	0.010777	Uiso ? Pb	
Pb12	1.0	0.492190	0.493775	0.339902	Uiso ? Pb	
Pb13	1.0	0.987341	0.509857	0.163946	Uiso ? Pb	
Pb14	1.0	0.002524	0.506628	0.493004	Uiso ? Pb	
Pb15	1.0	0.488997	0.987188	0.176349	Uiso ? Pb	
Pb16	1.0	0.508430	0.002824	0.494241	Uiso ? Pb	
I1	1.0	0.255958	0.531722	0.012456	Uiso ? I	
I2	1.0	0.247733	0.496247	0.334166	Uiso ? I	
I3	1.0	0.756106	0.517754	0.010103	Uiso ? I	
I4	1.0	0.748054	0.489541	0.336480	Uiso ? I	
I5	1.0	0.002163	0.270956	0.987615	Uiso ? I	
I6	1.0	0.004473	0.256176	0.325072	Uiso ? I	
I7	1.0	0.999459	0.769022	0.990725	Uiso ? I	
I8	1.0	0.980569	0.756653	0.331300	Uiso ? I	
I9	1.0	0.492298	0.246670	0.012945	Uiso ? I	
I10	1.0	0.508063	0.244775	0.332927	Uiso ? I	
I11	1.0	0.533056	0.748838	0.007676	Uiso ? I	
I12	1.0	0.492021	0.746105	0.345154	Uiso ? I	
I13	1.0	0.004606	0.482386	0.080127	Uiso ? I	
I14	1.0	0.016991	0.495105	0.413653	Uiso ? I	
I15	1.0	0.985061	0.999357	0.081398	Uiso ? I	
I16	1.0	0.959624	0.036098	0.414261	Uiso ? I	
I17	1.0	0.505725	0.486893	0.089593	Uiso ? I	
I18	1.0	0.507664	0.475978	0.420269	Uiso ? I	
I19	1.0	0.517211	0.981035	0.090350	Uiso ? I	
I20	1.0	0.570038	0.021304	0.418271	Uiso ? I	
I21	1.0	0.239446	0.517316	0.168888	Uiso ? I	
I22	1.0	0.259816	0.464426	0.495081	Uiso ? I	
I23	1.0	0.740962	0.480855	0.174673	Uiso ? I	
I24	1.0	0.762038	0.522618	0.491285	Uiso ? I	
I25	1.0	0.987920	0.253226	0.158841	Uiso ? I	
I26	1.0	0.003752	0.249294	0.508134	Uiso ? I	
I27	1.0	0.974424	0.753293	0.156288	Uiso ? I	
I28	1.0	0.033895	0.749158	0.491288	Uiso ? I	

I29	1.0	0.479432	0.240624	0.176697	Uiso ? I	
I30	1.0	0.525026	0.245243	0.506966	Uiso ? I	
I31	1.0	0.504221	0.740871	0.174875	Uiso ? I	
I32	1.0	0.504998	0.748494	0.503294	Uiso ? I	
I33	1.0	0.000859	0.513595	0.246687	Uiso ? I	
I34	1.0	0.035117	0.001453	0.248163	Uiso ? I	
I35	1.0	0.496486	0.485565	0.254941	Uiso ? I	
I36	1.0	0.458204	0.976804	0.256953	Uiso ? I	
I37	1.0	0.256687	0.991837	0.013689	Uiso ? I	
I38	1.0	0.755800	0.030041	0.003464	Uiso ? I	
I39	1.0	0.247033	0.001415	0.349685	Uiso ? I	
I40	1.0	0.747166	0.999805	0.323489	Uiso ? I	
I41	1.0	0.244426	0.994169	0.163361	Uiso ? I	
I42	1.0	0.744856	0.012852	0.180233	Uiso ? I	
I43	1.0	0.267674	0.009899	0.475945	Uiso ? I	
I44	1.0	0.766195	0.985440	0.505938	Uiso ? I	
O1	1.0	0.452254	0.488837	0.568748	Uiso ? O	
O2	1.0	0.391176	0.330149	0.584650	Uiso ? O	
O3	1.0	0.288432	0.469191	0.590022	Uiso ? O	

Table S5. Crystal data of the DFT slab models of the 3D perovskite and dimethylsulfoxide (S).

```
#======================================================================
# CRYSTAL DATA
#----------------------------------------------------------------------
data_VESTA_phase_1

_chemical_name_common                  'POSCAR pvsk S                '
_cell_length_a                         12.722600
_cell_length_b                         12.722600
_cell_length_c                         38.167801
_cell_angle_alpha                      90.000000
_cell_angle_beta                       90.000000
_cell_angle_gamma                      90.000000
_cell_volume                           6178.013930
_space_group_name_H-M_alt              'P 1'
_space_group_IT_number                 1

loop_
_space_group_symop_operation_xyz
   'x, y, z'

loop_
   _atom_site_label
   _atom_site_occupancy
   _atom_site_fract_x
   _atom_site_fract_y
   _atom_site_fract_z
   _atom_site_adp_type
   _atom_site_U_iso_or_equiv
   _atom_site_type_symbol
```

C1	1.0	0.240118	0.274525	0.083401	Uiso ? C	
C2	1.0	0.258803	0.291018	0.415265	Uiso ? C	
C3	1.0	0.252621	0.786835	0.083791	Uiso ? C	
C4	1.0	0.265783	0.771170	0.417150	Uiso ? C	

C5	1.0	0.754325	0.279441	0.088699	Uiso	? C
C6	1.0	0.754425	0.287515	0.419498	Uiso	? C
C7	1.0	0.755172	0.778913	0.088548	Uiso	? C
C8	1.0	0.753276	0.759038	0.405252	Uiso	? C
C9	1.0	0.242180	0.294272	0.252325	Uiso	? C
C10	1.0	0.242138	0.767218	0.256456	Uiso	? C
C11	1.0	0.755315	0.239321	0.262174	Uiso	? C
C12	1.0	0.738530	0.775622	0.253221	Uiso	? C
C13	1.0	0.309331	0.563552	0.606469	Uiso	? C
C14	1.0	0.468924	0.704396	0.603208	Uiso	? C
N1	1.0	0.317841	0.226543	0.099096	Uiso	? N
N2	1.0	0.344583	0.238257	0.421899	Uiso	? N
N3	1.0	0.343039	0.739168	0.080521	Uiso	? N
N4	1.0	0.290724	0.711860	0.443719	Uiso	? N
N5	1.0	0.802522	0.262152	0.059087	Uiso	? N
N6	1.0	0.755617	0.240213	0.389059	Uiso	? N
N7	1.0	0.803686	0.773992	0.058471	Uiso	? N
N8	1.0	0.840237	0.770384	0.423124	Uiso	? N
N9	1.0	0.201497	0.245634	0.053269	Uiso	? N
N10	1.0	0.164726	0.249699	0.414130	Uiso	? N
N11	1.0	0.161572	0.742392	0.077987	Uiso	? N
N12	1.0	0.188120	0.752442	0.395562	Uiso	? N
N13	1.0	0.679303	0.220184	0.101305	Uiso	? N
N14	1.0	0.752800	0.240999	0.449991	Uiso	? N
N15	1.0	0.687306	0.709122	0.099501	Uiso	? N
N16	1.0	0.673432	0.702664	0.415570	Uiso	? N
N17	1.0	0.159735	0.268962	0.233747	Uiso	? N
N18	1.0	0.320026	0.700682	0.259072	Uiso	? N
N19	1.0	0.842036	0.253168	0.244439	Uiso	? N
N20	1.0	0.779814	0.751414	0.222984	Uiso	? N
N21	1.0	0.309416	0.226653	0.264947	Uiso	? N
N22	1.0	0.170955	0.764420	0.231868	Uiso	? N
N23	1.0	0.663048	0.221591	0.248414	Uiso	? N
N24	1.0	0.686794	0.709734	0.273077	Uiso	? N
H1	1.0	0.205446	0.342450	0.096266	Uiso	? H
H2	1.0	0.266056	0.374549	0.409889	Uiso	? H
H3	1.0	0.252751	0.868147	0.092426	Uiso	? H
H4	1.0	0.312205	0.841431	0.412500	Uiso	? H
H5	1.0	0.778214	0.347349	0.104036	Uiso	? H
H6	1.0	0.755007	0.372906	0.419470	Uiso	? H
H7	1.0	0.772622	0.845010	0.105610	Uiso	? H
H8	1.0	0.747558	0.799091	0.380167	Uiso	? H
H9	1.0	0.344696	0.251696	0.122731	Uiso	? H
H10	1.0	0.413741	0.278038	0.423017	Uiso	? H
H11	1.0	0.410190	0.780854	0.083831	Uiso	? H
H12	1.0	0.350730	0.733689	0.460059	Uiso	? H
H13	1.0	0.859582	0.312326	0.051010	Uiso	? H
H14	1.0	0.756569	0.285478	0.367131	Uiso	? H
H15	1.0	0.854263	0.832241	0.051659	Uiso	? H
H16	1.0	0.897443	0.818528	0.413860	Uiso	? H
H17	1.0	0.355220	0.163838	0.088224	Uiso	? H
H18	1.0	0.342295	0.161376	0.429375	Uiso	? H
H19	1.0	0.348710	0.664713	0.071046	Uiso	? H
H20	1.0	0.249522	0.646583	0.450662	Uiso	? H
H21	1.0	0.783961	0.200735	0.042909	Uiso	? H
H22	1.0	0.754623	0.160826	0.386419	Uiso	? H
H23	1.0	0.789430	0.715988	0.040605	Uiso	? H
H24	1.0	0.851710	0.738374	0.447287	Uiso	? H

H25	1.0	0.230618	0.182692	0.039693	Uiso	? H
H26	1.0	0.151104	0.172243	0.418944	Uiso	? H
H27	1.0	0.155376	0.667125	0.069109	Uiso	? H
H28	1.0	0.140751	0.688291	0.398085	Uiso	? H
H29	1.0	0.651147	0.156187	0.088344	Uiso	? H
H30	1.0	0.752101	0.161469	0.453136	Uiso	? H
H31	1.0	0.665269	0.646323	0.084662	Uiso	? H
H32	1.0	0.674203	0.662373	0.438657	Uiso	? H
H33	1.0	0.142102	0.286603	0.041859	Uiso	? H
H34	1.0	0.101938	0.297129	0.409512	Uiso	? H
H35	1.0	0.094752	0.785158	0.081027	Uiso	? H
H36	1.0	0.175653	0.801632	0.375067	Uiso	? H
H37	1.0	0.643547	0.239297	0.124238	Uiso	? H
H38	1.0	0.752000	0.286065	0.472009	Uiso	? H
H39	1.0	0.649997	0.719020	0.122865	Uiso	? H
H40	1.0	0.608484	0.697904	0.400175	Uiso	? H
H41	1.0	0.255796	0.377090	0.257561	Uiso	? H
H42	1.0	0.236184	0.828939	0.276080	Uiso	? H
H43	1.0	0.760678	0.242737	0.290532	Uiso	? H
H44	1.0	0.748195	0.855625	0.262775	Uiso	? H
H45	1.0	0.110996	0.326751	0.225179	Uiso	? H
H46	1.0	0.372987	0.708038	0.278857	Uiso	? H
H47	1.0	0.909528	0.265845	0.258111	Uiso	? H
H48	1.0	0.814179	0.808342	0.208267	Uiso	? H
H49	1.0	0.139086	0.192970	0.228963	Uiso	? H
H50	1.0	0.330971	0.641026	0.241733	Uiso	? H
H51	1.0	0.845563	0.251492	0.217780	Uiso	? H
H52	1.0	0.772354	0.678733	0.211973	Uiso	? H
H53	1.0	0.303375	0.147770	0.260948	Uiso	? H
H54	1.0	0.172024	0.709619	0.212424	Uiso	? H
H55	1.0	0.650304	0.218347	0.222113	Uiso	? H
H56	1.0	0.671569	0.634253	0.265755	Uiso	? H
H57	1.0	0.370435	0.251706	0.280049	Uiso	? H
H58	1.0	0.113506	0.820029	0.231674	Uiso	? H
H59	1.0	0.600018	0.214225	0.264608	Uiso	? H
H60	1.0	0.655609	0.734297	0.296197	Uiso	? H
H61	1.0	0.259375	0.624801	0.617439	Uiso	? H
H62	1.0	0.261943	0.506006	0.592444	Uiso	? H
H63	1.0	0.356713	0.525493	0.626550	Uiso	? H
H64	1.0	0.417030	0.764752	0.613842	Uiso	? H
H65	1.0	0.503612	0.656540	0.623921	Uiso	? H
H66	1.0	0.529331	0.740859	0.587003	Uiso	? H
Pb1	1.0	0.998127	0.509372	0.000355	Uiso	? Pb
Pb2	1.0	0.993590	0.507363	0.328149	Uiso	? Pb
Pb3	1.0	0.513179	0.985567	0.009189	Uiso	? Pb
Pb4	1.0	0.492841	0.997909	0.337667	Uiso	? Pb
Pb5	1.0	0.999218	0.009915	0.163887	Uiso	? Pb
Pb6	1.0	0.001678	0.011367	0.491706	Uiso	? Pb
Pb7	1.0	0.491925	0.497270	0.172651	Uiso	? Pb
Pb8	1.0	0.499306	0.491069	0.504331	Uiso	? Pb
Pb9	1.0	0.011970	0.004286	0.000750	Uiso	? Pb
Pb10	1.0	0.996354	0.007661	0.329648	Uiso	? Pb
Pb11	1.0	0.497095	0.485456	0.009808	Uiso	? Pb
Pb12	1.0	0.491034	0.490711	0.338414	Uiso	? Pb
Pb13	1.0	0.990486	0.510691	0.164102	Uiso	? Pb
Pb14	1.0	0.002339	0.505749	0.492490	Uiso	? Pb
Pb15	1.0	0.493880	0.990340	0.175250	Uiso	? Pb
Pb16	1.0	0.507709	0.004269	0.493833	Uiso	? Pb
I1	1.0	0.257854	0.526254	0.014853	Uiso	? I

I2	1.0	0.247939	0.490318	0.332465	Uiso	? I
I3	1.0	0.758027	0.518070	0.005963	Uiso	? I
I4	1.0	0.749199	0.489340	0.336537	Uiso	? I
I5	1.0	0.000799	0.267011	0.987503	Uiso	? I
I6	1.0	0.998456	0.256053	0.325128	Uiso	? I
I7	1.0	0.002195	0.765382	0.990312	Uiso	? I
I8	1.0	0.983816	0.757938	0.328721	Uiso	? I
I9	1.0	0.489828	0.245529	0.012570	Uiso	? I
I10	1.0	0.513524	0.242066	0.331446	Uiso	? I
I11	1.0	0.533788	0.747561	0.007869	Uiso	? I
I12	1.0	0.485551	0.743880	0.342548	Uiso	? I
I13	1.0	0.998669	0.486040	0.079714	Uiso	? I
I14	1.0	0.022773	0.502914	0.413431	Uiso	? I
I15	1.0	0.988524	0.996248	0.079874	Uiso	? I
I16	1.0	0.959718	0.034183	0.413391	Uiso	? I
I17	1.0	0.512103	0.486813	0.088572	Uiso	? I
I18	1.0	0.501487	0.472529	0.418436	Uiso	? I
I19	1.0	0.512121	0.984035	0.089345	Uiso	? I
I20	1.0	0.570313	0.016100	0.417744	Uiso	? I
I21	1.0	0.244250	0.523002	0.170401	Uiso	? I
I22	1.0	0.257665	0.478980	0.499555	Uiso	? I
I23	1.0	0.745303	0.483579	0.173673	Uiso	? I
I24	1.0	0.759990	0.518826	0.488248	Uiso	? I
I25	1.0	0.992616	0.254415	0.158057	Uiso	? I
I26	1.0	0.003031	0.252760	0.503273	Uiso	? I
I27	1.0	0.977489	0.754989	0.156455	Uiso	? I
I28	1.0	0.031208	0.752250	0.493324	Uiso	? I
I29	1.0	0.482362	0.243404	0.175593	Uiso	? I
I30	1.0	0.522193	0.249659	0.513652	Uiso	? I
I31	1.0	0.512555	0.743339	0.175902	Uiso	? I
I32	1.0	0.517485	0.755823	0.498595	Uiso	? I
I33	1.0	0.000818	0.514694	0.246374	Uiso	? I
I34	1.0	0.026708	0.006184	0.247065	Uiso	? I
I35	1.0	0.502884	0.483757	0.253539	Uiso	? I
I36	1.0	0.457923	0.977872	0.255921	Uiso	? I
I37	1.0	0.255825	0.990886	0.010861	Uiso	? I
I38	1.0	0.754793	0.026230	0.003519	Uiso	? I
I39	1.0	0.246368	0.004865	0.348136	Uiso	? I
I40	1.0	0.746579	0.998743	0.323654	Uiso	? I
I41	1.0	0.245840	0.992789	0.162111	Uiso	? I
I42	1.0	0.745975	0.015059	0.178221	Uiso	? I
I43	1.0	0.269661	0.008926	0.474804	Uiso	? I
I44	1.0	0.768499	0.992532	0.507813	Uiso	? I
S1	1.0	0.394039	0.622033	0.574609	Uiso	? S
O1	1.0	0.470244	0.534529	0.565008	Uiso	? O

1280

Table S6. Fitted XRD peak positions.

	2D		2D/3D	
	$OA_2MAPb_2Br_2I_5$	$OA_2FAPb_2Br_2I_5$	OcMA:S on baseline 3D w/ excess PbI_2, MACl, $MAPbBr_3$	Oc on $FAPbI_3$ w/ excess PbI_2 only
n=2(020)	3.39°	3.43°	3.44°	3.46°
n=2(040)	6.77°	6.85°	6.92°	-
n=2(060)	10.16°	10.28°	10.31°	-
n=2(080)	13.56°	13.70°	-	-
n=2(0100)	16.97°	17.15°	17.16°	-

1285

Table S7. Average device photovoltaic parameters.

	V_{OC} (V)	J_{SC} (mA cm^{-2})	FF (%)	PCE (%)
Bare 3D	1.103 ±0.009	25.47 ±0.16	76.8 ±0.8	21.56 ±0.38
Oc	1.138 ±0.007	25.74 ±0.12	81.1 ±0.6	23.75 ±0.28
OcMA:F	1.163 ±0.005	25.73 ±0.13	82.1 ±0.6	24.57 ±0.22
OcMA:PC	1.171 ±0.004	25.76 ±0.14	82.5 ±0.4	24.88 ±0.18
OcMA:S	1.184 ±0.005	25.76 ±0.13	83.0 ±0.5	25.32 ±0.25

Table S8. Photovoltaic parameters of the champion devices.

	V_{OC} (V)	J_{SC} (mA cm^{-2})	FF (%)	PCE (%)
Bare 3D	1.104	25.64	78.4	22.2
Oc	1.153	25.85	82.1	24.5
OcMA:F	1.172	25.89	82.6	25.1
OcMA:PC	1.175	25.85	82.8	25.1
OcMA:S	1.189	25.89	84.1	25.9

Table S9. Literature summary of state-of-the-art device stabilities from years 2022-2024, for both the regular nip and inverted pin device architectures. World-record devices (certified on the NREL efficiency chart) are highlighted in red.

Institution	PCE retention (%)	MPP duration (hours)	Light source	MPP temp (°C)	Device structure	Ref.
This work	96 %	1,724 h	1-sun AM1.5G illumination (UV included)	40-45°C	Regular nip	-
This work	95 %	807 h	1-sun AM1.5G illumination (UV included)	65°C	Regular nip	-
This work	91 %	1,074 h	1-sun AM1.5G illumination (UV included)	85°C	Regular nip	-
UNIST	88 %	600 h	1-sun AM1.5G illumination	25°C	Regular nip	(*19*) Nature 2023
École Polytechnique Fédérale de Lausanne (EPFL)	87.19 %	1,000 h	1-sun illumination	65°C	Regular nip	(*48*) Nature 2024
Peking University	95.8 %	500 h	1-sun illumination	50°C	Regular nip	(*49*) Science 2024
Northwestern University	85 %	1,250 h	1-sun illumination	85°C	Regular nip	(*5*) Nature 2024
Shanghai Jiao Tong University (SJTU)	92 %	1,500 h	1-sun illumination	25°C	Regular nip	(*50*) Nature 2024
NREL	90 %	1,000 h	1-sun illumination	40°C	Regular nip	(*1*) Science 2022
Beijing Institute of Technology (BIT)	91 %	500 h	1-sun illumination, LED source	65±5°C	Regular nip	(*51*) Science 2023
Beijing Institute of Technology (BIT)	89 %	500 h	1-sun illumination, LED source	85±5°C	Regular nip	(*51*) Science 2023
UNIST	85 %	450 h	LED lamp, 100 mW cm^{-2} 35°C	35°C	Regular nip	(*52*) Nature 2021
Southern University of Science and Technology (SUST)	94 %	1,000 h	1-sun AM1.5G illumination	50±5°C	Inverted pin	(*53*) Science 2024

Northwestern Uni / U of Toronto	95 %	1,075 h	1-sun illumination	65°C	Inverted pin	(*31*) Nature 2023
Chinese Academy of Sciences (CAS)	85.4 %	1,000 h	1-sun illumination	50°C	Inverted pin	(*54*) Science 2023
KAUST	90 %	1,000 h	1-sun illumination	40°C	Inverted pin	(*8*) Nature 2024
City University of Hong Kong (CUHK)	85 %	1,200 h	1-sun illumination	65°C	Inverted pin	(*55*) Science 2023
City University of Hong Kong (CUHK)	90 %	1,200 h	1-sun illumination	65°C	Inverted pin	(*55*) Science 2023
Wuhan National Laboratory for Optoelectronics	97 %	750 h	1-sun AM1.5G illumination	55±5°C	Inverted pin	(*56*) Science 2024
East China University of Science and Technology (ECUST)	90 %	2,000 h	1-sun illumination	45°C	Inverted pin	(*57*) Science 2023
Northwestern Uni / U of Toronto	84 %	1,586 h	1-sun illumination	85°C	Inverted pin	(*58*) Science 2023
Chinese Academy of Sciences (CAS)	92 %	2,500 h	1-sun illumination	25°C	Inverted pin	(*7*) Nature 2023
Rice University	97 %	1,000 h	1-sun illumination (no UV filter)	85°C	Inverted pin	(*47*) Science 2024
Northwestern Uni / U of Toronto	95 %	1,200 h	1-sun illumination	65°C	Inverted pin	(*59*) Science 2024
Oxford University	95 %	1,600 h	76 mW cm^{-2} full-spectrum illumination	85°C	Inverted pin	(*60*) Science 2024
KAUST	95 %	500 h	1-sun AM1.5G illumination	25°C	Inverted pin	(*3*) Science 2022
Helmholtz-Zentrum Berlin (HZB)	96 %	1,000 h	1-sun illumination	25°C	Inverted pin	(*61*) Science 2023
NREL	87 %	2,428 h	1-sun illumination	55±2°C	Inverted pin	(*25*) Nature 2022
City University of Hong Kong (CUHK)	95 %	2,000 h	1-sun AM1.5G illumination	65°C	Inverted pin	(*62*) Science 2024
National University of Singapore (NUS)	93 %	500 h	LED 1-sun illumination	30°C	Inverted pin	(*63*)

						Nat. Energy 2024
Peking University	90 %	1,142 h	LED 1-sun illumination	40±5°C	Inverted pin	(*64*) Nature 2024
Beijing Institute of Technology (BIT)	90 %	800 h	1-sun AM1.5G illumination	50°C	Inverted pin	(*65*) Science 2024

References and Notes

1. F. Zhang, S. Y. Park, C. Yao, H. Lu, S. P. Dunfield, C. Xiao, S. Uličná, X. Zhao, L. Du Hill, X. Chen, X. Wang, L. E. Mundt, K. H. Stone, L. T. Schelhas, G. Teeter, S. Parkin, E. L. Ratcliff, Y.-L. Loo, J. J. Berry, M. C. Beard, Y. Yan, B. W. Larson, K. Zhu, Metastable Dion-Jacobson 2D structure enables efficient and stable perovskite solar cells. *Science* **375**, 71–76 (2022).

2. J. Tong, Q. Jiang, A. J. Ferguson, A. F. Palmstrom, X. Wang, J. Hao, S. P. Dunfield, A. E. Louks, S. P. Harvey, C. Li, H. Lu, R. M. France, S. A. Johnson, F. Zhang, M. Yang, J. F. Geisz, M. D. McGehee, M. C. Beard, Y. Yan, D. Kuciauskas, J. J. Berry, K. Zhu, Carrier control in Sn–Pb perovskites via 2D cation engineering for all-perovskite tandem solar cells with improved efficiency and stability. *Nat. Energy* **7**, 642–651 (2022).

3. R. Azmi, E. Ugur, A. Seitkhan, F. Aljamaan, A. S. Subbiah, J. Liu, G. T. Harrison, M. I. Nugraha, M. K. Eswaran, M. Babics, Y. Chen, F. Xu, T. G. Allen, A. ur Rehman, C. Wang, T. D. Anthopoulos, U. Schwingenschlögl, M. De Bastiani, E. Aydin, S. De Wolf, Damp heat–stable perovskite solar cells with tailored-dimensionality 2D/3D heterojunctions. *Science* **376**, 73–77 (2022).

4. S. Sidhik, Y. Wang, M. De Siena, R. Asadpour, A. J. Torma, T. Terlier, K. Ho, W. Li, A. B. Puthirath, X. Shuai, A. Agrawal, B. Traore, M. Jones, R. Giridharagopal, P. M. Ajayan, J. Strzalka, D. S. Ginger, C. Katan, M. A. Alam, J. Even, M. G. Kanatzidis, A. D. Mohite, Deterministic fabrication of 3D/2D perovskite bilayer stacks for durable and efficient solar cells. *Science* **377**, 1425–1430 (2022).

5. C. Liu, Y. Yang, H. Chen, I. Spanopoulos, A. S. R. Bati, I. W. Gilley, J. Chen, A. Maxwell, B. Vishal, R. P. Reynolds, T. E. Wiggins, Z. Wang, C. Huang, J. Fletcher, Y. Liu, L. X. Chen, S. De Wolf, B. Chen, D. Zheng, T. J. Marks, A. Facchetti, E. H. Sargent, M. G. Kanatzidis, Two-dimensional perovskitoids enhance stability in perovskite solar cells. *Nature* **633**, 359–364 (2024).

6. R. Lin, J. Xu, M. Wei, Y. Wang, Z. Qin, Z. Liu, J. Wu, K. Xiao, B. Chen, S. M. Park, G. Chen, H. R. Atapattu, K. R. Graham, J. Xu, J. Zhu, L. Li, C. Zhang, E. H. Sargent, H. Tan, All-perovskite tandem solar cells with improved grain surface passivation. *Nature* **603**, 73–78 (2022).

7. Z. Liang, Y. Zhang, H. Xu, W. Chen, B. Liu, J. Zhang, H. Zhang, Z. Wang, D.-H. Kang, J. Zeng, X. Gao, Q. Wang, H. Hu, H. Zhou, X. Cai, X. Tian, P. Reiss, B. Xu, T. Kirchartz, Z. Xiao, S. Dai, N.-G. Park, J. Ye, X. Pan, Homogenizing out-of-plane cation composition in perovskite solar cells. *Nature* **624**, 557–563 (2023).

8. R. Azmi, D. S. Utomo, B. Vishal, S. Zhumagali, P. Dally, A. M. Risqi, A. Prasetio, E. Ugur, F. Cao, I. F. Imran, A. A. Said, A. R. Pininti, A. S. Subbiah, E. Aydin, C. Xiao, S. Il Seok, S. De

Wolf, Double-side 2D/3D heterojunctions for inverted perovskite solar cells. *Nature* **628**, 93–98 (2024).

9. H. Gu, J. Xia, C. Liang, Y. Chen, W. Huang, G. Xing, Phase-pure two-dimensional layered perovskite thin films. *Nat. Rev. Mater.* **8**, 533–551 (2023).

10. M. Kim, G.-H. Kim, T. K. Lee, I. W. Choi, H. W. Choi, Y. Jo, Y. J. Yoon, J. W. Kim, J. Lee, D. Huh, H. Lee, S. K. Kwak, J. Y. Kim, D. S. Kim, Methylammonium Chloride Induces Intermediate Phase Stabilization for Efficient Perovskite Solar Cells. *Joule* **3**, 2179–2192 (2019).

11. J.-W. Lee, S. Tan, S. Il Seok, Y. Yang, N.-G. Park, Rethinking the A cation in halide perovskites. *Science* **375**, eabj1186 (2022).

12. K. Domanski, B. Roose, T. Matsui, M. Saliba, S.-H. Turren-Cruz, J.-P. Correa-Baena, C. R. Carmona, G. Richardson, J. M. Foster, F. De Angelis, J. M. Ball, A. Petrozza, N. Mine, M. K. Nazeeruddin, W. Tress, M. Grätzel, U. Steiner, A. Hagfeldt, A. Abate, Migration of cations induces reversible performance losses over day/night cycling in perovskite solar cells. *Energy Environ. Sci.* **10**, 604–613 (2017).

13. J. M. Azpiroz, E. Mosconi, J. Bisquert, F. De Angelis, Defect migration in methylammonium lead iodide and its role in perovskite solar cell operation. *Energy Environ. Sci.* **8**, 2118–2127 (2015).

14. S. Tan, I. Yavuz, N. De Marco, T. Huang, S. Lee, C. S. Choi, M. Wang, S. Nuryyeva, R. Wang, Y. Zhao, H.-C. Wang, T.-H. Han, B. Dunn, Y. Huang, J.-W. Lee, Y. Yang, Steric Impediment of Ion Migration Contributes to Improved Operational Stability of Perovskite Solar Cells. *Adv. Mater.* **32**, 1906995 (2020).

15. Q. Chen, H. Zhou, T.-B. Song, S. Luo, Z. Hong, H.-S. Duan, L. Dou, Y. Liu, Y. Yang, Controllable Self-Induced Passivation of Hybrid Lead Iodide Perovskites toward High Performance Solar Cells. *Nano Lett.* **14**, 4158–4163 (2014).

16. A. H. Proppe, A. Johnston, S. Teale, A. Mahata, R. Quintero-Bermudez, E. H. Jung, L. Grater, T. Cui, T. Filleter, C.-Y. Kim, S. O. Kelley, F. De Angelis, E. H. Sargent, Multication perovskite 2D/3D interfaces form via progressive dimensional reduction. *Nat. Commun.* **12**, 3472 (2021).

17. S. Tan, T. Huang, I. Yavuz, R. Wang, M. H. Weber, Y. Zhao, M. Abdelsamie, M. E. Liao, H. Wang, K. Huynh, K. Wei, J. Xue, F. Babbe, M. S. Goorsky, J. Lee, C. M. Sutter-Fella, Y. Yang, Surface Reconstruction of Halide Perovskites During Post-treatment. *J. Am. Chem. Soc.* **143**, 6781–6786 (2021).

18. J. Xue, R. Wang, K.-L. Wang, Z.-K. Wang, I. Yavuz, Y. Wang, Y. Yang, X. Gao, T. Huang, S. Nuryyeva, J. Lee, Y. Duan, L. Liao, R. Kaner, Y. Yang, Crystalline Liquid-like Behavior: Surface-Induced Secondary Grain Growth of Photovoltaic Perovskite Thin Film. *J. Am. Chem. Soc.* **141**, 13948–13953 (2019).

19. J. Park, J. Kim, H.-S. Yun, M. J. Paik, E. Noh, H. J. Mun, M. G. Kim, T. J. Shin, S. Il Seok, Controlled growth of perovskite layers with volatile alkylammonium chlorides. *Nature* **616**, 724–730 (2023).

20. H. Lu, Y. Liu, P. Ahlawat, A. Mishra, W. R. Tress, F. T. Eickemeyer, Y. Yang, F. Fu, Z. Wang,

C. E. Avalos, B. I. Carlsen, A. Agarwalla, X. Zhang, X. Li, Y. Zhan, S. M. Zakeeruddin, L. Emsley, U. Rothlisberger, L. Zheng, A. Hagfeldt, M. Grätzel, Vapor-assisted deposition of highly efficient, stable black-phase FAPbI 3 perovskite solar cells. *Science* **370**, 1–8 (2020).

21. Y. Xu, M. Wang, Y. Lei, Z. Ci, Z. Jin, Crystallization Kinetics in 2D Perovskite Solar Cells. *Adv. Energy Mater.* **10**, 1–18 (2020).

22. J.-W. Lee, H.-S. Kim, N.-G. Park, Lewis Acid-Base Adduct Approach for High Efficiency Perovskite Solar Cells. *Acc. Chem. Res.* **49**, 311–319 (2016).

23. J. Euvrard, Y. Yan, D. B. Mitzi, Electrical doping in halide perovskites. *Nat. Rev. Mater.* **6**, 531–549 (2021).

24. J. Peng, F. Kremer, D. Walter, Y. Wu, Y. Ji, J. Xiang, W. Liu, T. Duong, H. Shen, T. Lu, F. Brink, D. Zhong, L. Li, O. Lee Cheong Lem, Y. Liu, K. J. Weber, T. P. White, K. R. Catchpole, Centimetre-scale perovskite solar cells with fill factors of more than 86 per cent. *Nature* **601**, 573–578 (2022).

25. Q. Jiang, J. Tong, Y. Xian, R. A. Kerner, S. P. Dunfield, C. Xiao, R. A. Scheidt, D. Kuciauskas, X. Wang, M. P. Hautzinger, R. Tirawat, M. C. Beard, D. P. Fenning, J. J. Berry, B. W. Larson, Y. Yan, K. Zhu, Surface reaction for efficient and stable inverted perovskite solar cells. *Nature* **611**, 278–283 (2022).

26. Y. Yang, M. Yang, D. T. Moore, Y. Yan, E. M. Miller, K. Zhu, M. C. Beard, Top and bottom surfaces limit carrier lifetime in lead iodide perovskite films. *Nat. Energy* **2**, 16207 (2017).

27. T. Malinauskas, D. Tomkute-Luksiene, R. Sens, M. Daskeviciene, R. Send, H. Wonneberger, V. Jankauskas, I. Bruder, V. Getautis, Enhancing Thermal Stability and Lifetime of Solid-State Dye-Sensitized Solar Cells via Molecular Engineering of the Hole-Transporting Material Spiro-OMeTAD. *ACS Appl. Mater. Interfaces* **7**, 11107–11116 (2015).

28. F. Lamberti, T. Gatti, E. Cescon, R. Sorrentino, A. Rizzo, E. Menna, G. Meneghesso, M. Meneghetti, A. Petrozza, L. Franco, Evidence of Spiro-OMeTAD De-doping by tert-Butylpyridine Additive in Hole-Transporting Layers for Perovskite Solar Cells. *Chem* **5**, 1806–1817 (2019).

29. F. M. Rombach, S. A. Haque, T. J. Macdonald, Lessons learned from spiro-OMeTAD and PTAA in perovskite solar cells. *Energy Environ. Sci.* **14**, 5161–5190 (2021).

30. T. Moot, J. B. Patel, G. McAndrews, E. J. Wolf, D. Morales, I. E. Gould, B. A. Rosales, C. C. Boyd, L. M. Wheeler, P. A. Parilla, S. W. Johnston, L. T. Schelhas, M. D. McGehee, J. M. Luther, Temperature Coefficients of Perovskite Photovoltaics for Energy Yield Calculations. *ACS Energy Lett.* **6**, 2038–2047 (2021).

31. S. M. Park, M. Wei, N. Lempesis, W. Yu, T. Hossain, L. Agosta, V. Carnevali, H. R. Atapattu, P. Serles, F. T. Eickemeyer, H. Shin, M. Vafaie, D. Choi, K. Darabi, E. D. Jung, Y. Yang, D. Bin Kim, S. M. Zakeeruddin, B. Chen, A. Amassian, T. Filleter, M. G. Kanatzidis, K. R. Graham, L. Xiao, U. Rothlisberger, M. Grätzel, E. H. Sargent, Low-loss contacts on textured substrates for inverted perovskite solar cells. *Nature* **624**, 289–294 (2023).

32. M. V. Khenkin, E. A. Katz, A. Abate, G. Bardizza, J. J. Berry, C. Brabec, F. Brunetti, V. Bulović, Q. Burlingame, A. Di Carlo, R. Cheacharoen, Y.-B. Cheng, A. Colsmann, S. Cros, K. Domanski, M. Dusza, C. J. Fell, S. R. Forrest, Y. Galagan, D. Di Girolamo, M. Grätzel, A.

Hagfeldt, E. von Hauff, H. Hoppe, J. Kettle, H. Köbler, M. S. Leite, S. Liu, Y.-L. Loo, J. M. Luther, C.-Q. Ma, M. Madsen, M. Manceau, M. Matheron, M. McGehee, R. Meitzner, M. K. Nazeeruddin, A. F. Nogueira, Ç. Odabaşı, A. Osherov, N.-G. Park, M. O. Reese, F. De Rossi, M. Saliba, U. S. Schubert, H. J. Snaith, S. D. Stranks, W. Tress, P. A. Troshin, V. Turkovic, S. Veenstra, I. Visoly-Fisher, A. Walsh, T. Watson, H. Xie, R. Yıldırım, S. M. Zakeeruddin, K. Zhu, M. Lira-Cantu, Consensus statement for stability assessment and reporting for perovskite photovoltaics based on ISOS procedures. *Nat. Energy* **5**, 35–49 (2020).

33. T. Zhang, F. Wang, H.-B. Kim, I.-W. Choi, C. Wang, E. Cho, R. Konefal, Y. Puttisong, K. Terado, L. Kobera, M. Chen, M. Yang, S. Bai, B. Yang, J. Suo, S.-C. Yang, X. Liu, F. Fu, H. Yoshida, W. M. Chen, J. Brus, V. Coropceanu, A. Hagfeldt, J.-L. Brédas, M. Fahlman, D. S. Kim, Z. Hu, F. Gao, Ion-modulated radical doping of spiro-OMeTAD for more efficient and stable perovskite solar cells. *Science* **377**, 495–501 (2022).

34. T.-H. Han, S. Tan, J. Xue, L. Meng, J.-W. Lee, Y. Yang, Interface and Defect Engineering for Metal Halide Perovskite Optoelectronic Devices. *Adv. Mater.* **31**, 1803515 (2019).

35. J. Carrillo, A. Guerrero, S. Rahimnejad, O. Almora, I. Zarazua, E. Mas-Marza, J. Bisquert, G. Garcia-Belmonte, Ionic Reactivity at Contacts and Aging of Methylammonium Lead Triiodide Perovskite Solar Cells. *Adv. Energy Mater.* **6**, 1502246 (2016).

36. C. Besleaga, L. E. Abramiuc, V. Stancu, A. G. Tomulescu, M. Sima, L. Trinca, N. Plugaru, L. Pintilie, G. A. Nemnes, M. Iliescu, H. Gud, A. Manolescu, I. Pintilie, Iodine Migration and Degradation of Perovskite Solar Cells Enhanced by Metallic Electrodes. *J. Phys. Chem. Lett.* **7**, 5168–5175 (2016).

37. K. Domanski, J.-P. Correa-Baena, N. Mine, M. K. Nazeeruddin, A. Abate, M. Saliba, W. Tress, A. Hagfeldt, M. Grätzel, Not All That Glitters Is Gold: Metal-Migration- Induced Degradation in Perovskite Solar Cells. *ACS Nano* **10**, 6306–6314 (2016).

38. G. Tumen-Ulzii, C. Qin, D. Klotz, M. R. Leyden, P. Wang, M. Auffray, T. Fujihara, T. Matsushima, J. Lee, S. Lee, Y. Yang, C. Adachi, Detrimental Effect of Unreacted PbI 2 on the Long-Term Stability of Perovskite Solar Cells. *Adv. Mater.* **32**, 1905035 (2020).

39. S. Wang, Y. Jiang, E. J. Juarez-perez, L. K. Ono, Y. Qi, Accelerated degradation of methylammonium lead iodide perovskites induced by exposure to iodine vapour ShenghaoWang†,. *Nat. Energy* **16195**, 1–8 (2016).

40. S. Tan, I. Yavuz, M. H. Weber, T. Huang, C.-H. Chen, R. Wang, H.-C. Wang, J. H. Ko, S. Nuryyeva, J. Xue, Y. Zhao, K.-H. Wei, J.-W. Lee, Y. Yang, Shallow Iodine Defects Accelerate the Degradation of α-Phase Formamidinium Perovskite. *Joule* **4**, 2426–2442 (2020).

41. Y. Zhou, I. Poli, D. Meggiolaro, F. De Angelis, A. Petrozza, Defect activity in metal halide perovskites with wide and narrow bandgap. *Nat. Rev. Mater.* **0123456789** (2021).

42. B. Chen, P. N. Rudd, S. Yang, Y. Yuan, J. Huang, Imperfections and their passivation in halide perovskite solar cells. *Chem. Soc. Rev.* **48**, 3842–3867 (2019).

43. G. Kresse, J. Hafner, Ab initio molecular dynamics for liquid metals. *Phys. Rev. B* **47**, 558–561 (1993).

44. G. Kresse, J. Furthmuller, Efficiency of ab-initio total energy calculations for metals and semiconductors using a plane-wave basis set. *Comput. Mater. Sci.* **6**, 15–50 (1996).

45. J. Klimeš, D. R. Bowler, A. Michaelides, Van der Waals density functionals applied to solids. *Phys. Rev. B* **83**, 195131 (2011).

46. H. Peng, Z.-H. Yang, J. P. Perdew, J. Sun, Versatile van der Waals Density Functional Based on a Meta-Generalized Gradient Approximation. *Phys. Rev. X* **6**, 041005 (2016).

47. S. Sidhik, I. Metcalf, W. Li, T. Kodalle, C. J. Dolan, M. Khalili, J. Hou, F. Mandani, A. Torma, H. Zhang, R. Garai, J. Persaud, A. Marciel, I. A. Muro Puente, G. N. M. Reddy, A. Balvanz, M. A. Alam, C. Katan, E. Tsai, D. Ginger, D. P. Fenning, M. G. Kanatzidis, C. M. Sutter-Fella, J. Even, A. D. Mohite, Two-dimensional perovskite templates for durable, efficient formamidinium perovskite solar cells. *Science* **384**, 1227–1235 (2024).

48. B. Ding, Y. Ding, J. Peng, J. Romano-deGea, L. E. K. Frederiksen, H. Kanda, O. A. Syzgantseva, M. A. Syzgantseva, J.-N. Audinot, J. Bour, S. Zhang, T. Wirtz, Z. Fei, P. Dörflinger, N. Shibayama, Y. Niu, S. Hu, S. Zhang, F. F. Tirani, Y. Liu, G.-J. Yang, K. Brooks, L. Hu, S. Kinge, V. Dyakonov, X. Zhang, S. Dai, P. J. Dyson, M. K. Nazeeruddin, Dopant-additive synergism enhances perovskite solar modules. *Nature* **628**, 299–305 (2024).

49. Y. Zou, W. Yu, H. Guo, Q. Li, X. Li, L. Li, Y. Liu, H. Wang, Z. Tang, S. Yang, Y. Chen, B. Qu, Y. Gao, Z. Chen, S. Wang, D. Zhang, Y. Chen, Q. Chen, S. M. Zakeeruddin, Y. Peng, H. Zhou, Q. Gong, M. Wei, M. Grätzel, L. Xiao, A crystal capping layer for formation of black-phase FAPbI 3 perovskite in humid air. *Science* **385**, 161–167 (2024).

50. H. Wang, S. Su, Y. Chen, M. Ren, S. Wang, Y. Wang, C. Zhu, Y. Miao, C. Ouyang, Y. Zhao, Impurity-healing interface engineering for efficient perovskite submodules. *Nature*, doi: 10.1038/s41586-024-08073-w (2024).

51. Y. Bai, Z. Huang, X. Zhang, J. Lu, X. Niu, Z. He, C. Zhu, M. Xiao, Q. Song, X. Wei, C. Wang, Z. Cui, J. Dou, Y. Chen, F. Pei, H. Zai, W. Wang, T. Song, P. An, J. Zhang, J. Dong, Y. Li, J. Shi, H. Jin, P. Chen, Y. Sun, Y. Li, H. Chen, Z. Wei, H. Zhou, Q. Chen, Initializing film homogeneity to retard phase segregation for stable perovskite solar cells. *Science* **378**, 747–754 (2022).

52. J. Jeong, M. Kim, J. Seo, H. Lu, P. Ahlawat, A. Mishra, Y. Yang, M. A. Hope, F. T. Eickemeyer, M. Kim, Y. J. Yoon, I. W. Choi, B. P. Darwich, S. J. Choi, Y. Jo, J. H. Lee, B. Walker, S. M. Zakeeruddin, L. Emsley, U. Rothlisberger, A. Hagfeldt, D. S. Kim, M. Grätzel, J. Y. Kim, Pseudo-halide anion engineering for α-FAPbI3 perovskite solar cells. *Nature* **592**, 381–385 (2021).

53. P. Zhu, D. Wang, Y. Zhang, Z. Liang, J. Li, J. Zeng, J. Zhang, Y. Xu, S. Wu, Z. Liu, X. Zhou, B. Hu, F. He, L. Zhang, X. Pan, X. Wang, N.-G. Park, B. Xu, Aqueous synthesis of perovskite precursors for highly efficient perovskite solar cells. *Science* **383**, 524–531 (2024).

54. S. Yu, Z. Xiong, H. Zhou, Q. Zhang, Z. Wang, F. Ma, Z. Qu, Y. Zhao, X. Chu, X. Zhang, J. You, Homogenized NiO x nanoparticles for improved hole transport in inverted perovskite solar cells. *Science* **382**, 1399–1404 (2023).

55. Z. Li, X. Sun, X. Zheng, B. Li, D. Gao, S. Zhang, X. Wu, S. Li, J. Gong, J. M. Luther, Z. Li, Z. Zhu, Stabilized hole-selective layer for high-performance inverted p-i-n perovskite solar cells. *Science* **382**, 284–289 (2023).

56. J. Liu, X. Chen, K. Chen, W. Tian, Y. Sheng, B. She, Y. Jiang, D. Zhang, Y. Liu, J. Qi, K. Chen, Y. Ma, Z. Qiu, C. Wang, Y. Yin, S. Zhao, J. Leng, S. Jin, W. Zhao, Y. Qin, Y. Su, X. Li,

X. Li, Y. Zhou, Y. Zhou, F. Ling, A. Mei, H. Han, Electron injection and defect passivation for high-efficiency mesoporous perovskite solar cells. *Science* **383**, 1198–1204 (2024).

57. S. Zhang, F. Ye, X. Wang, R. Chen, H. Zhang, L. Zhan, X. Jiang, Y. Li, X. Ji, S. Liu, M. Yu, F. Yu, Y. Zhang, R. Wu, Z. Liu, Z. Ning, D. Neher, L. Han, Y. Lin, H. Tian, W. Chen, M. Stolterfoht, L. Zhang, W.-H. Zhu, Y. Wu, Minimizing buried interfacial defects for efficient inverted perovskite solar cells. *Science* **380**, 404–409 (2023).

58. S. M. Park, M. Wei, J. Xu, H. R. Atapattu, F. T. Eickemeyer, K. Darabi, L. Grater, Y. Yang, C. Liu, S. Teale, B. Chen, H. Chen, T. Wang, L. Zeng, A. Maxwell, Z. Wang, K. R. Rao, Z. Cai, S. M. Zakeeruddin, J. T. Pham, C. M. Risko, A. Amassian, M. G. Kanatzidis, K. R. Graham, M. Grätzel, E. H. Sargent, Engineering ligand reactivity enables high-temperature operation of stable perovskite solar cells. *Science* **381**, 209–215 (2023).

59. H. Chen, C. Liu, J. Xu, A. Maxwell, W. Zhou, Y. Yang, Q. Zhou, A. S. R. Bati, H. Wan, Z. Wang, L. Zeng, J. Wang, P. Serles, Y. Liu, S. Teale, Y. Liu, M. I. Saidaminov, M. Li, N. Rolston, S. Hoogland, T. Filleter, M. G. Kanatzidis, B. Chen, Z. Ning, E. H. Sargent, Improved charge extraction in inverted perovskite solar cells with dual-site-binding ligands. *Science* **384**, 189–193 (2024).

60. Y.-H. Lin, Vikram, F. Yang, X.-L. Cao, A. Dasgupta, R. D. J. Oliver, A. M. Ulatowski, M. M. McCarthy, X. Shen, Q. Yuan, M. G. Christoforo, F. S. Y. Yeung, M. B. Johnston, N. K. Noel, L. M. Herz, M. S. Islam, H. J. Snaith, Bandgap-universal passivation enables stable perovskite solar cells with low photovoltage loss. *Science* **384**, 767–775 (2024).

61. G. Li, Z. Su, L. Canil, D. Hughes, M. H. Aldamasy, J. Dagar, S. Trofimov, L. Wang, W. Zuo, J. J. Jerónimo-Rendon, M. M. Byranvand, C. Wang, R. Zhu, Z. Zhang, F. Yang, G. Nasti, B. Naydenov, W. C. Tsoi, Z. Li, X. Gao, Z. Wang, Y. Jia, E. Unger, M. Saliba, M. Li, A. Abate, Highly efficient p-i-n perovskite solar cells that endure temperature variations. *Science* **379**, 399–403 (2023).

62. D. Gao, B. Li, Q. Liu, C. Zhang, Z. Yu, S. Li, J. Gong, L. Qian, F. Vanin, K. Schutt, M. A. Davis, A. F. Palmstrom, S. P. Harvey, N. J. Long, J. M. Luther, X. C. Zeng, Z. Zhu, Long-term stability in perovskite solar cells through atomic layer deposition of tin oxide. *Science* **386**, 187–192 (2024).

63. J. Li, H. Liang, C. Xiao, X. Jia, R. Guo, J. Chen, X. Guo, R. Luo, X. Wang, M. Li, M. Rossier, A. Hauser, F. Linardi, E. Alvianto, S. Liu, J. Feng, Y. Hou, Enhancing the efficiency and longevity of inverted perovskite solar cells with antimony-doped tin oxides. *Nat. Energy* **9**, 308–315 (2024).

64. S. Li, Y. Xiao, R. Su, W. Xu, D. Luo, P. Huang, L. Dai, P. Chen, P. Caprioglio, K. A. Elmestekawy, M. Dubajic, C. Chosy, J. Hu, I. Habib, A. Dasgupta, D. Guo, Y. Boeije, S. J. Zelewski, Z. Lu, T. Huang, Q. Li, J. Wang, H. Yan, H. Chen, C. Li, B. A. I. Lewis, D. Wang, J. Wu, L. Zhao, B. Han, J. Wang, L. M. Herz, J. R. Durrant, K. S. Novoselov, Z. Lu, Q. Gong, S. D. Stranks, H. J. Snaith, R. Zhu, Coherent growth of high-Miller-index facets enhances perovskite solar cells. *Nature*, 0–1 (2024).

65. Y. Chen, N. Yang, G. Zheng, F. Pei, W. Zhou, Y. Zhang, L. Li, Z. Huang, G. Liu, R. Yin, H. Zhou, C. Zhu, T. Song, C. Hu, D. Zheng, Y. Bai, Y. Duan, Y. Ye, Y. Wu, Q. Chen, Nuclei engineering for even halide distribution in stable perovskite/silicon tandem solar cells. *Science* **385**, 554–560 (2024).